A Study of Extrusion Printed Millimetre-Scale MEMS Transducers

by

Desmond Lagace

A Thesis submitted to the Faculty of Graduate Studies of

The University of Manitoba

in partial fulfilment of the requirements of the degree of

MASTER OF SCIENCE

Department of Electrical and Computer Engineering

University of Manitoba

Winnipeg

Acknowledgements

I would like to thank my supervisor **Dr. Cyrus Shafai** for his unwavering guidance and support throughout this project. His leadership, advice, and thoughtfulness has been paramount, and I would certainly not be where I am today without it.

I would like to thank **Tao Chen** for his help and guidance in learning the practical aspects of developing and testing sensors and actuators. For training on equipment and assisting with technical development, I would like to thank **Dwayne Chrusch**, **James Dietrich**, **Zoran Trajkoski**, **Cory Smit**, **Oleg Shevchenko**, **Mount-First Ng**, and **Sinisa Janjic**. This project would not have been possible without your technical expertise and help.

I would like to thank **Mohammad Rezaeimeybodi**, **Phiona Buhr**, and **Ramin Soltanzadeh** for your support, guidance, and most of all, your friendship.

I would like to thank my partner **Taylor Mutch** for being close to my side for the entirety of this degree - both ups and downs; your love and support has been unwavering and absolutely crucial to my success. I would like to thank my parents for their generous love and support, as well as my sister and brother-in-law for theirs.

Thank you to everyone.

Abstract

This thesis presents a comparison in performance of various microelectromechanical devices fabricated by both lithographic methods in a clean room facility and by means of extrusion printing of conductive ink. Traditional microelectromechanical systems (MEMS) fabrication practices involve costly, time-consuming and complex multi-step processes utilising high-end, high-maintenance cleanroom facilities. On the other hand, printed electronics (PE) offers quick turn-around time, low-cost, and simplicity.

The work completed in this thesis involves taking candidate MEMS transducer designs intended for clean room fabrication and scaling them up to the resolution of a direct-ink write extrusion printer. Firstly, unknown ink parameters are determined through experimentation and simulation. Then, past MEMS designs for a Lorentz actuator and DC electric field sensor are scaled up and in some cases changed slightly to accommodate PE. A Lorentz actuator-based electromagnetic relay is designed as well. The devices are then fabricated using a direct ink writing (DIW) printer in conjunction with a laser micro-machining tool, and are tested to both verify the simulations and offer comparison to their respective MEMS counterparts and/or other similar devices from the literature.

A key finding was comparable performance metrics between the PE devices fabricated in this thesis, and their respective lithographic or commercially available counterparts. This signifies that PE is a viable alternative to lithography for manufacturing some MEMS devices, or at least offers itself as a means of rapid prototyping. In addition, the ink used in this thesis was characterized for use in simulation models.

Contents

List of Figures

List of Tables

List of Abbreviations

1

Introduction

1.1 | Motivation

As of now, all around the world, electronic devices and transducers manufactured by traditional means and processes dominate the technological landscape, contributing to a $646B global market [1]. These devices, manufactured primarily from semiconducting silicon and/or other inorganic materials and metals, have fundamentally changed the way we as a species live, grow, and interact with each other; however, this comes at a cost. Manufactured primarily in facilities such as clean rooms, these devices require complex and expensive equipment, both to operate and to maintain, lengthy and labour-intensive fabrication processes, and generate considerable chemical and heavy metal waste. Furthermore, start-up and long-term maintenance costs associated with cleanrooms are fixed and do not scale with production. As a consequence, there as been significant research and advancements in the field of additive manufacturing (AM) and printed electronics (PE) to act as an alternative to traditional methods for manufacture of small and complex electronic devices [1]. PE promises less setup time, less equipment, fewer production steps, less chemical

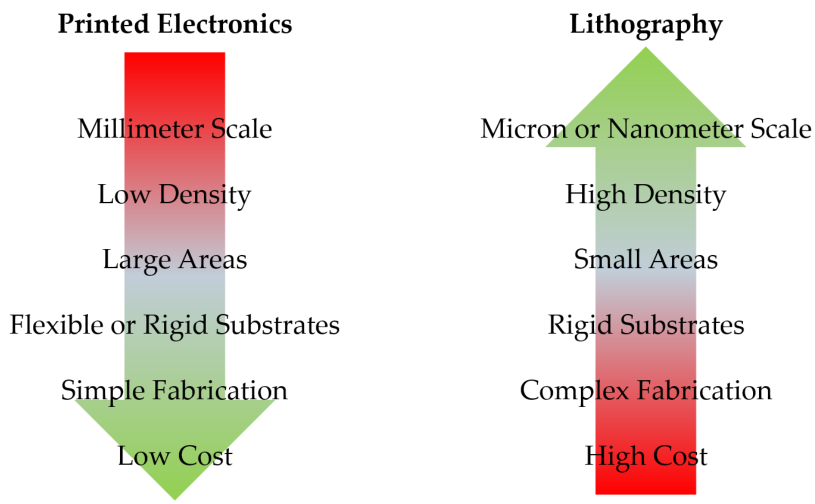

Figure 1.1: Printed electronics vs. lithography.

waste, and faster production time over traditional lithographic techniques [2], as shown in Fig. 1.1.

Though PE has been used extensively for applications in biomedical devices, wearables, displays, radio frequency identification (RFID) tags, strain gauges, and more [3], the idea of printing MEMS devices by direct ink writing (DIW) of conductive ink has not been fully explored in the current literature; in fact, less than 1% of AM-centric papers focus on MEMS [4]. It presents an interesting challenge, as at the ~100-150 μm resolution of PE [5], some 10-100 μm-scale MEMS devices are *nearly* printable, and the trade-off of size versus performance is magnified. It is the existence of this trade-off that yields the impetus for the research conducted for this thesis, which aims to show how size affects performance (and other application-specific parameters) for printed MEMS devices. This thesis also hopes to set the stage for future work to be done as PE printing resolution improves further.

1.2 | Aims and Objectives

The 3 core objectives of this thesis are to:

1. **Simulate** scaled-up MEMS devices with PE materials.

2. **Fabricate** the scaled-up devices using PE.

3. **Test** and compare the performance of printed vs. lithographic MEMS.

The completion of these objectives will yield the feasibility and highlight the trade-offs associated with printing MEMS devices vs. manufacturing them in a clean room environment, granted the current state-of-the-art in PE technology and resolution.

1.3 | Contributions

The work presented in this thesis makes the following contributions:

- Establishes the presence of novel printed electronics research at the University of Manitoba.

- Determines best practices for extrusion printing MEMS devices to aid in rapid prototyping and development.

1.4 | MEMS Devices

There are 3 devices (Fig. 1.2) selected for comparison in this thesis:

1. DC Electric Field Sensor

2. Lorentz Actuator

3. Lorentz-actuated Relay

These are chosen for their simplicity as well as they possess 2-dimensional planar designs, which best facilitates the use and feasibility of PE. Additionally, they are all similar in their simulation settings, fabrication processes, and testing procedures, thus maintaining consistency.

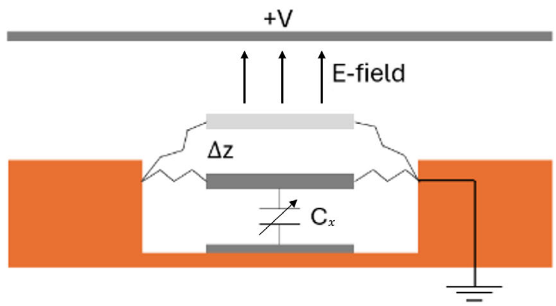

(a) DC Electric Field Sensor

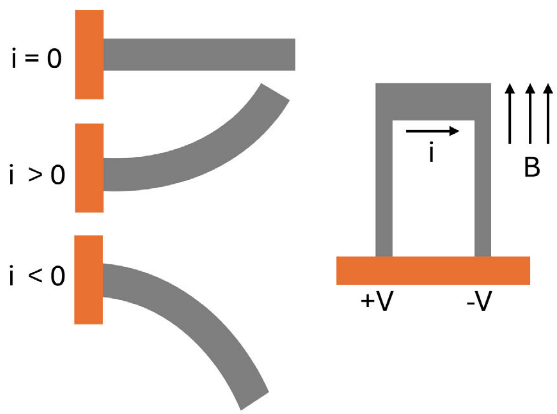

(b) Lorentz Actuator

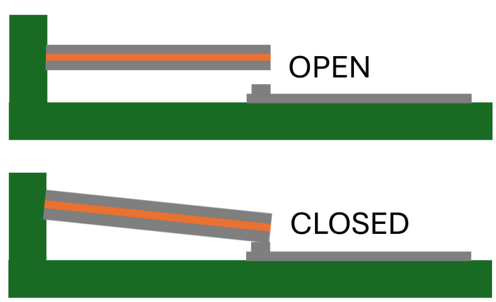

(c) Lorentz Actuator Relay

Figure 1.2: Devices studied in this thesis.

1.5 | Thesis Structure

This thesis is laid out as follows, as 7 chapters:

1. Chapter 1 Introduction: motivation and introduction to thesis topic.
2. Chapter 2 Printed Electronics Technology: background on PE technology used in this thesis, current state of AM/PE for MEMS devices, as well as determination of ink parameters for modeling and simulation.
3. Chapter 3 DC Electric Field Sensor: background, comparison of scaled up PE DC electric field sensor to MEMS.
4. Chapter 4 Lorentz Actuator: background, comparison of scaled up PE MEMS Lorentz actuator to MEMS.
5. Chapter 5 Lorentz Actuator Relay: background, fabrication trials, results.
6. Chapter 6 Discussion and Conclusion: conclusion of this thesis is presented based on experimental findings.
7. Future Work: recommendations on future work that could be done with PE for MEMS.
8. References

2

Background

Printed electronics (PE) involves depositing a layer of conductive or functional material on a surface of either a rigid, flexible, or functional substrate. Popular methods for PE include gravure, screen, inkjet, and extrusion printing [6]. Gravure printing, also known as roll-to-roll, involves two adjacent rollers; one to carry the ink in circumferentially impressed molds, and another to feed and press the ink pattern onto the substrate. Although it requires large output in order to see any economical benefit, sub-micron features are achievable. Screen printing is quite popular, utilising a rubber squeegee to push ink through a patterned mesh screen and onto a substrate. Micron-level features are attainable, but again this method is not cost-efficient unless large quantities of prints are required. Inkjet printing is a very common direct-ink writing DIW process, involving depositing low viscosity ink droplets, one drop at a time, at a controlled rate through an array of microscopic droplet dispensers. It results in high resolution (1-10 micrometre level), flexibility, ease of use, and fast speed. However, it can be very difficult to create suitable inks for this process, as droplet formation demands strict and narrow viscosity ranges. Extrusion printing involves loading (and liquefying, if required) a material, extruding the material out of the nozzle with pre-defined pressure, and moving the dispenser around, depositing liquid material in a program-defined route. Advantages include low cost, short production cycle, and high accuracy. However, resolution is highly dependent on printer type and ink composition and viscosity, as well as the accuracy of the stepper motors present in most extrusion printing apparatuses.

In this thesis, focus will be placed on extrusion printing over other methods which have largely been covered by other works [7]. Also, the availability of new extrusion printing technology breeds new and exciting opportunities for research in the area. This chapter will cover the current technology in extrusion printed electronics, including printers, inks and substrates. Next, the technology used in this thesis is highlighted along with some relevant works from the literature. Finally, a review of the state-of-the-art in printed MEMS technology is discussed.

2.1 | Extrusion Printing

A specific sub-domain of PE is extrusion printing, which involves pushing or extruding ink out of a nozzle at a controlled rate, dependent upon nozzle size, pressure, and ink viscosity [8]. Filament-based fused deposition modelling (FDM) 3D printers familiarly use this technology, heating and melting a rod or filament of material while simultaneously extruding it to print a 3D object, layer-by-layer. Extrusion printing for PE, on the other hand, has lagged behind other PE methods until somewhat recently, being enabled by the advent of a wide variety of conductive and functional ready-to-use inks, fitting the strict demands of extrusion printing for viscosity and particle size through careful selection of binders, surfactants, and stabilizers [3]. Furthermore, printers with smart dispensers and sophisticated control systems facilitate finer control over various process parameters [9].

2.1.1 | Printers

Extrusion printing is a form of additive manufacturing. It is well known in the 3D printing domain, utilising materials such as low-melting point metals, ceramic slurries, suspensions containing nanoparticles, silicones, and concrete, among others [10]. The main advantage of this technique is its ability to deposit a wide range of materials in a straightforward and economical manner, which makes it robust and easily scalable.

There exist three types of extrusion printing: plunger-based, filament-based, and screw-based [11] (Fig. 2.1).

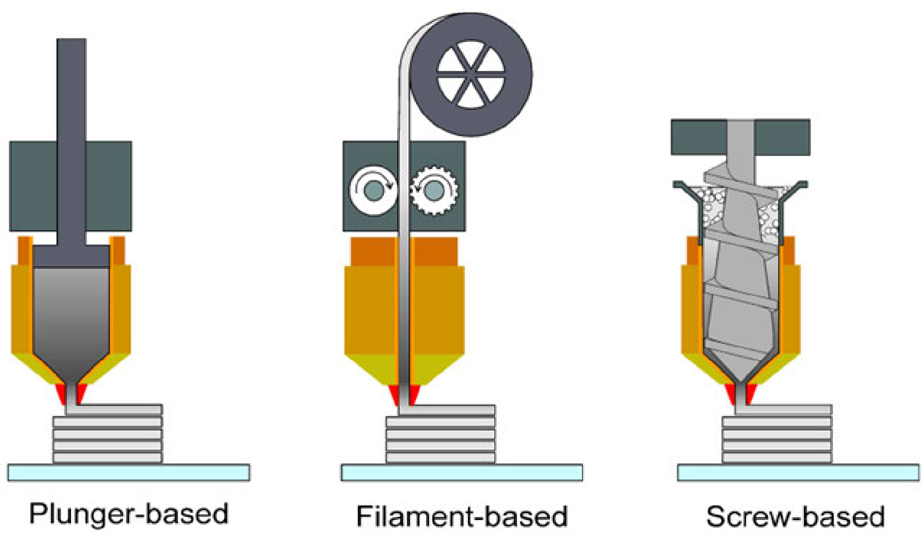

Figure 2.1: Three methods of extrusion printing. Reproduced from [11] under the terms of the Creative Commons (CC BY) License.

Plunger-based works by pushing a soft or liquid material with low viscosity through a nozzle by means of pressure induced by a plunger, or, in some cases, pressurized air. The materials for this process, generally referred to as inks, are designed to contain a solvent to suspend the desired deposited material. Thus, a post-deposition step is required, such as sintering and curing to remove the solvent and harden the suspended material into one contiguous shape. Examples of plunger-based printers used for printable electronics available in the market today are the Voltera V-One and Voltera NOVA [5] (Fig. 2.2). The Voltera NOVA, in particular, is capable of printing conductive ink on flexible substrates through utilisation of a vacuumed printing stage to hold the substrates secure.

Figure 2.2: Voltera V-One (top) and NOVA (bottom) plunger-based extrusion printers.

Filament printers are used as a safe and simple alternative to plunger-based methods but are much less common in the context of printable electronics. They involve feeding a thermoplastic or low-melting point metal filament through a liquefier, which the extrudes out of a nozzle. This technique is much more prevalent in 3D printing, where layer-by-layer of deposition of plastics is achieved. However, some printers combine this method with a conductive ink dispenser to implement electrical conductivity in a plastic 3D structure, such as the Voxel8 [12] (Fig. 2.3).

Figure 2.3: Voxel-8 filament electronics printer.

Screw-based methods are a popular alternative if a filament or ink cannot be manufactured due to constraints on material properties or technical know-how. This method involves using a hopper of solid pellets of the desired material fed into a heating zone to be melted. A rotating screw auger helps to push the pellets through the heating zone and the molten plastic out of the nozzle. In the context of printable electronics, the Nano3DPrint A2200 3D multi-material electronics printer uses a screw mechanism to extrude either thermoplastics or conductive material for the manufacturing of printed circuits and devices [13] (Fig. 2.4).

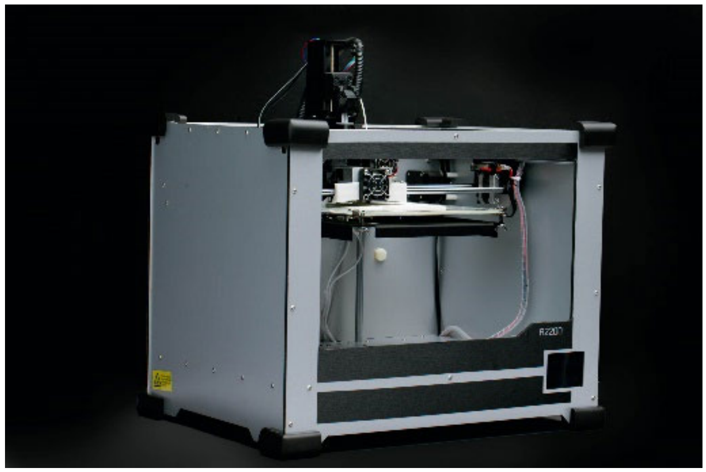

Figure 2.4: NanoPrint3D A2200 screw-based printer.

2.1.2 | Inks

There is a myriad of inks that are available, with a number of them being more compatible on some substrates than on others, and also exhibiting different electrical and functional properties. In addition, for a given printer, the concept of printability is paramount for achieving a high-quality print, affected by factors such as viscosity and curing method [14]. Each printer type discussed in the previous section has its own requirements on the ranges of viscosity's and different types of inks they can accommodate. Conductive inks are usually composed of conductive metal nanoparticles (NPs), typically silver, homogeneously suspended in a blend of stabilizers, organic solvents, and sintering agents [15]. Before the process of sintering the ink may not be conducting at all. Upon sintering, the organic solvents evaporate and the stabilizers are removed, allowing the NPs to coalesce into one whole conducting solid structure. Fig. 2.5 shows a schematic of the ink curing process.

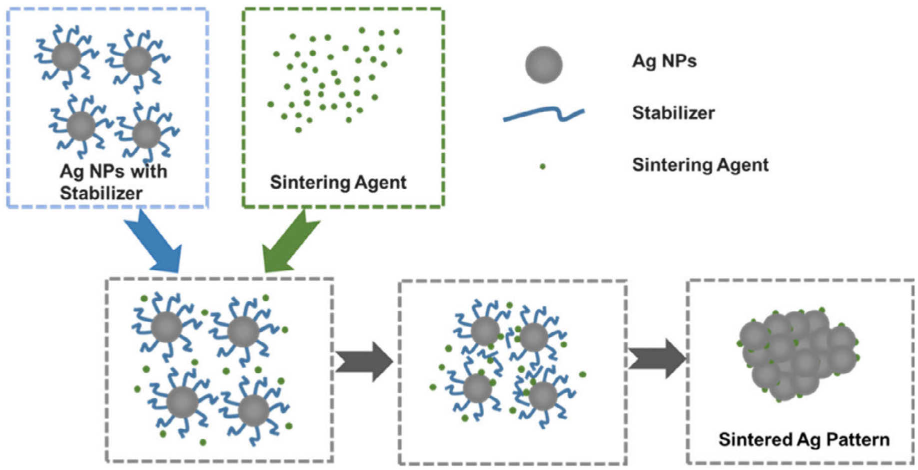

Figure 2.5: Conductive ink curing process. Reproduced from [15] under the terms of the Creative Commons Attribution (CC BY) License.

2.1.3 | Substrates

There exist a number of substrates suitable for extrusion printing in printable electronics. Each has its own functionality, from acting as simply a surface for a given circuit to be printed on, to being a functional and interconnected member of a circuit or device [16]. In the most general sense, there are really two distinct types of substrates: rigid and flexible. Rigid substrates are typically metal or glass – Si or SiO_2 are good examples – or more commonly a polymer composite such as flame retardant 4 (FR4) or plexiglass. Flexible substrates are commonly a polymer such as polyimide (PI), polyethylene terephthalate (PET), polydimethylsiloxane (PDMS), etc., or organic composites like paper. Each has its own advantages and disadvantages, and selecting one of either rigid or flexible substrates is dependent upon application, ink compatibility, and thermal, mechanical, chemical, electrical, and optical properties and requirements [16]. Also, surface roughness, adhesion properties, and surface energy – roughly, how a material's surface interacts with different materials

[17] – is an important consideration, and pre-treating of the substrates may be required to promote adhesion of inks to its surface [16].

The most common rigid substrate used in extrusion printing of electronic circuits is FR4. This material is generally regarded as a workhorse in printed circuit board (PCB) manufacturing due to its excellent dielectric properties, low cost, and mechanical strength [18]. For extrusion printing, FR4 on its own has moderate surface energy, offering sufficient adhesion for most conductive inks, and is generally compatible with most inks on the market without any pre-treatment requirements. Also, it has good resistance to most solvents used in electronic manufacturing, such as those found in conductive inks. However, FR4's glass transition temperature – the temperature at which it loses it mechanical structure and becomes soft – is around 130°C [19], which can limit the number of inks that can be used with it due to curing requirements.

On the other hand, there are a myriad of flexible substrates used in printable electronics, with no clear front-runner as is with the case of rigid substrates. Flexible substrates are commonly non-reinforced polymers, which lends more freedom of design than rigid substrates and contributes to clever and innovative applications in printable electronics [16]. As such, there is distinctly more research work being done in printable electronics for flexible substrates over rigid substrates.

2.2 | Printed MEMS

Microelectromechanical systems (MEMS) are utilised everywhere across various industries, such as automotive, consumer electronics, and medical, to name a few [20]. Examples include pressure sensors, gas sensors, accelerometers, and inkjet printer heads [4]. Sensing principles include capacitive, piezoresistive, and piezoelectric, whereas actuation principles include electrostatic, piezoelectric, and thermal [7]. The fabrication of these devices, composed principally of silicon, uses high-end, high maintenance cleanroom facilities, which are economically beneficial at large manufacturing scales, but infeasible for low-scale prototyping applications. Material deposition involves metal evaporation or vapor deposition equipment along with lithographic masking and etching processes. Fig. 2.6 shows the contrast in fabrication process between lithography and PE.

PE enables low cost, rapid prototyping of low-volume devices. However, there is a trade-off between with the benefits of PE and its disadvantages, such as decreased resolution and repeatability. Overcoming the challenge of matching the micron or sub-micron level of cleanroom fabrication facilities with PE is critical in establishing PE as a feasible alternative for prototyping MEMS devices. For some larger MEMS, on the scale of 10-100 μm, the resolution granted by most 2D and 3D printing techniques allows for almost 1:1 replication of the lithographic counterpart. For example, the authors in [20] realized a fully-functional MEMS accelerometer by means of multi-photon polymerization 3D printing, achieving a resolution of 6 μm. However, they had to rely on thermal evaporation to deposit the conductive material atop the 3D printed structure.

The majority of published research involving printed MEMS feature common 3D printing techniques [4], such as selective laser sintering, stereolithography, multi-photon polymerization, and more, whereas extrusion printing is not as highlighted. Inkjet printing of MEMS, however, is well documented. Devices such as microlenses, solder bumps, temperature sensors, strain sensors, thermal actuators, electrostatic actuators, gas/humidity sensors, and photodetectors have all been explored using inkjet printing [7]. Fig. 2.7 shows a flexible capacitive humidity sensor fabricated via inkjet printing [21]. These printed devices achieve printed thicknesses of around 1-10 μm, and a resolution of around 50-100 μm.

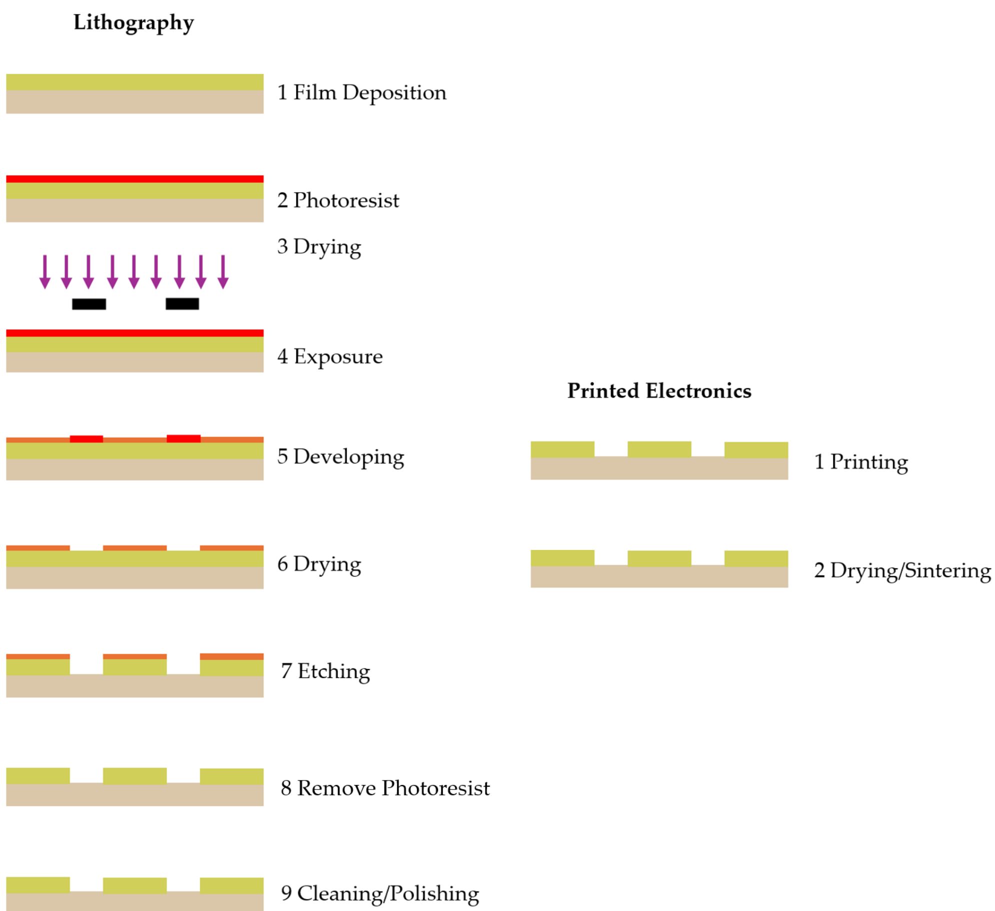

Figure 2.6: Lithography vs. printed electronics processes.

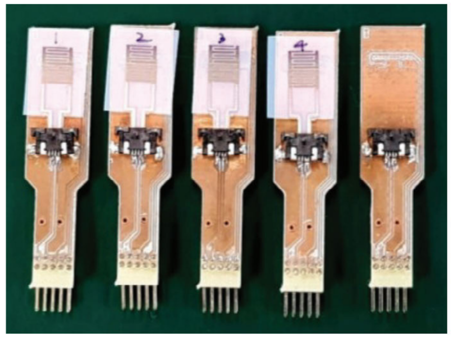

Figure 2.7: Inkjet printed capacitive humidity sensor (©2020 IEEE). S. Sulaiman, N. A. Rashid, A. S. A. Aziz, L. Q. Jun, and S. M. H. S. M. Jaafar, “Inkjet-printed graphene-based flexible humidity sensor for environmental applications,” in 2020 IEEE International Conference on Semiconductor Electronics (ICSE), pp. 148–151, 2020.

As mentioned, extrusion printing of MEMS devices is quite uncommon in the literature, with an average of 10 publications/year from 2017-2024 [22]. This could be attributed to its lower resolution (150-200 μm) than inkjet, as well as higher fluctuations in surface morphology due to extrusion printing's more viscous inks; the ink does not spread out as evenly as it does with inkjet printing. However, the low costs and wide portfolio of inks and substrates associated with extrusion printing can make it a viable alternative, especially as printing technology improves. Of the publications that highlight extrusion printing of sensors, the majority are strain gauges - whose resistance varies with applied stress - and most researchers opt for silver NPs inks [22]. Fig. 2.8 shows an example strain sensor from [23], made by embedding a printed silver ink structure within a 3D printed thermoplastic polymer substrate. Other examples from the literature include humidity sensors, pressure sensors, antennas, and electrochemical sensors. Most works are printed using 100-400 μm nozzles, and these devices are all on the millimetre scale.

Designing MEMS devices may require knowledge of electrical, thermal, optical, mechanical, chemical, and magnetic systems, and how they interact [24]. The devices in this

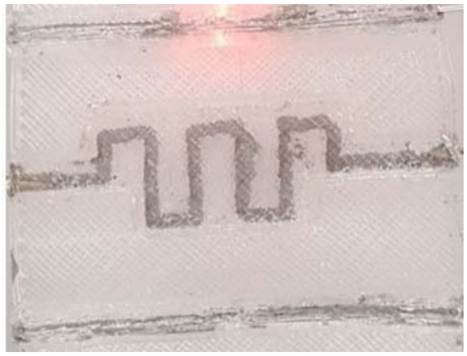

Figure 2.8: Extrusion printed strain sensor (©2018 IEEE). H. Nassar, M. Ntagios, W. T. Navaraj, and R. Dahiva, “Multi-material 3d printed bendable smart sensing structures,” in 2018 IEEE SENSORS, pp. 1–4, 2018.

thesis are consist of electrical, thermal, and mechanical interactions, and in order to design these devices, some important parameters related to the ink and substrate are required before moving forward.

For electrical systems in MEMS, there are typically two elements: the conductor and the dielectric; in context of this thesis, the ink is the conductor and the substrate is the dielectric. In the case of the conductor, the resistivity ρ is required, as this dictates electrical resistance R and thus current flow i, given an applied or induced voltage V:

$$R = \frac{\rho l}{A} \qquad i = \frac{V}{R}$$

where l is the length and A is the cross-sectional area of the conductor. For dielectrics, the dielectric constant ϵ is required, as this describes the strength of electric field E in the dielectric, and consequently the capacitance C - the ability of the dielectric to store electric charge. When an electric field is incident in a dielectric, the material polarizes to an extent based on the dielectric constant. This induces an electric field to counteract the incident field, which results in a net reduction of the field present inside the material:

$$E \rightarrow \frac{E}{\epsilon}$$

A higher dielectric constant increases capacitance because the dielectric material polarizes more strongly in response to an electric field. This polarization reduces the effective field between the capacitor plates, lowering the voltage for a given charge. The reduced voltage means more charge can be stored, resulting in higher capacitance:

$$C \rightarrow \epsilon C \qquad C = QV$$

In the case of thermal systems, the most relevant parameter to consider is the coefficient of thermal expansion, α. This dictates how much a material deforms - expands or contracts - from its original size V_0 based on a temperature change ΔT:

$$\Delta V = \alpha V_0 \Delta T$$

The temperature change can be a consequence of a myriad of different phenomena. In MEMS devices, it is induced most commonly through the process of Joule heating. This occurs when current i flows through a resistive material, causing it to dissipate energy as heat to the resistance R:

$$\Delta T = \frac{i^2 R t}{mc}$$

where t is the time interval, m is the mass of the material, and c is the specific heat capacity.

Lastly, for mechanical systems, one is generally concerned with how much a material moves or deforms due to an applied stress or force. This relationship is known as Hooke's law:

$$\sigma = Y\varepsilon$$

where σ is the applied stress, ε is the strain or deformation, and Y is the Young's modulus. The Young's modulus, then, is the parameter that satisfies this relationship, and is thus the most relevant parameter for designing mechanical MEMS devices. From Young's modulus, one can derive the spring constant k of some topology based on its Young's modulus and physical dimensions. Then, given an applied force F, the structure deflects or deforms by a displacement Δx, yielding a recast version of Hooke's law:

$$F = k\Delta x$$

To summarize, in order to design MEMS devices that involve electrical, thermal, and mechanical interactions, knowledge of the resistivity of the conductor, dielectric constant of the dielectric, coefficient of thermal expansion, and Young's modulus are all required at a bare minimum.

2.3 | Ink, Printer, and Substrate for This Thesis

The conductive ink used in this thesis is Voltera Conductor 3 silver conductive ink [25]. It exhibits good adhesion, flexibility, conductivity, and is robust to hand-soldering and rework. Also, it is readily available and makes little to no mess, requiring only a small amount of isopropyl alcohol (IPA) to clean up. Ink parameters are detailed in Table 2.1. Fig. 2.9 shows a ready-to-use cartridge of silver ink in a 2 mL package [26]. It is heated at 90 °C for 5 minutes to evaporate the solvents, then at 120 °C for 15 minutes to sinter and cure.

Figure 2.9: 2 mL cartridge of Voltera Conductor 3 silver ink.

Table 2.1: Voltera Conductor 3 silver ink parameters.

Resistivity $[\Omega \cdot m]$	1.27×10^{-7}
Typical Cured Thickness $[\mu m]$	15
Min. Line Width $[\mu m]$	150
Viscosity $[Pa \cdot s]$	15

The substrate used in this thesis is 50 μm thick polyimide (PI). This is due to its good adhesion to silver ink, high temperature and solvent resistance, durability, and flexibility. Also, the material is well documented, so important mechanical parameters required for simulation are readily available. Fig. 2.10 shows a sample of polyimide film [27]. Some useful parameters of PI are summarised in Table 2.2 [28].

The printer used in this thesis is a Voltera NOVA DIW electronics printer (Fig. 2.11) [29]. It utilises a smart dispenser system with an integrated pressure sensor and heater to monitor and manage ink flow rate, as well as a probe to accurately map the z-profile of the substrate to compensate for surface roughness and undulations before printing. It

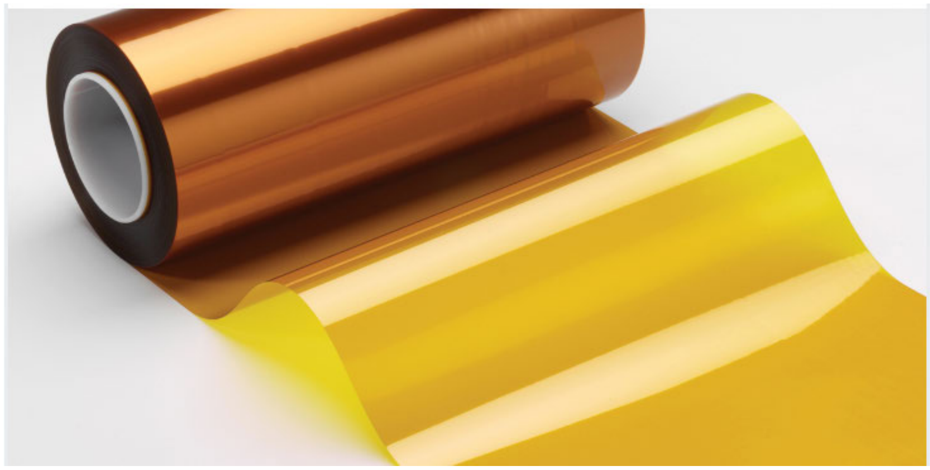

Figure 2.10: Polyimide film.

Table 2.2: Polyimide parameters.

Young's Modulus [GPa]	3.1
Density [kg/m^3]	1415
Coefficient of Thermal Expansion [$10^{-6}/K$]	45
Thermal Conductivity [$W/m \cdot K$]	0.535
Maximum Temperature [$^\circ C$]	250

also features a vacuumed printing stage for holding thin and flexible substrate still during the printing process, as well as user-friendly software allowing full control over all print parameters. Some examples of research with the NOVA include biomedical tattoos [30], a printed woven carbon heater for de-icing drone wings [31], and a smart CO_2 monitoring facemask [32]. Fig. (2.12) shows some examples. Most works are printed using 150-225 μm nozzles. The author of this thesis extrusion printed a piezoresistive strain sensor for respiration monitoring on a TPU substrate using carbon NP ink with a 150 μm nozzle and Voltera NOVA [33].

The most important print parameters for a printed ink trace are:

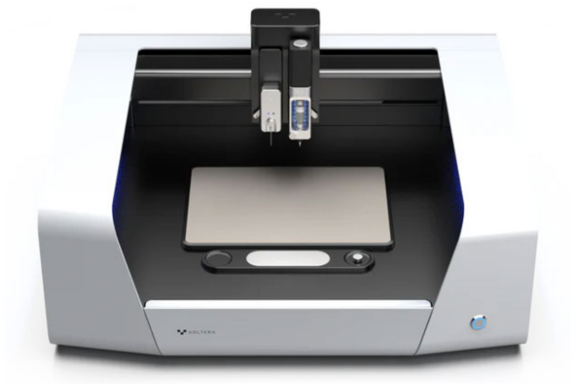

(a) Voltera NOVA

(b) Voltera Smart Dispenser

(c) Voltera Probe

Figure 2.11: Voltera NOVA DIW electronics printer.

- *Dispense Pressure*: the pressure exerted on the plunger to extrude the ink [arb. units].
- *Print Speed*: the speed at which this dispense head moves [mm/min].
- *Print Height*: the height of the nozzle above the substrate [μm].
- *Printed Line Width*: the post-cure width of a printed ink trace [μm].
- *Printed Line Height*: post-cure height of the a printed ink trace [μm].

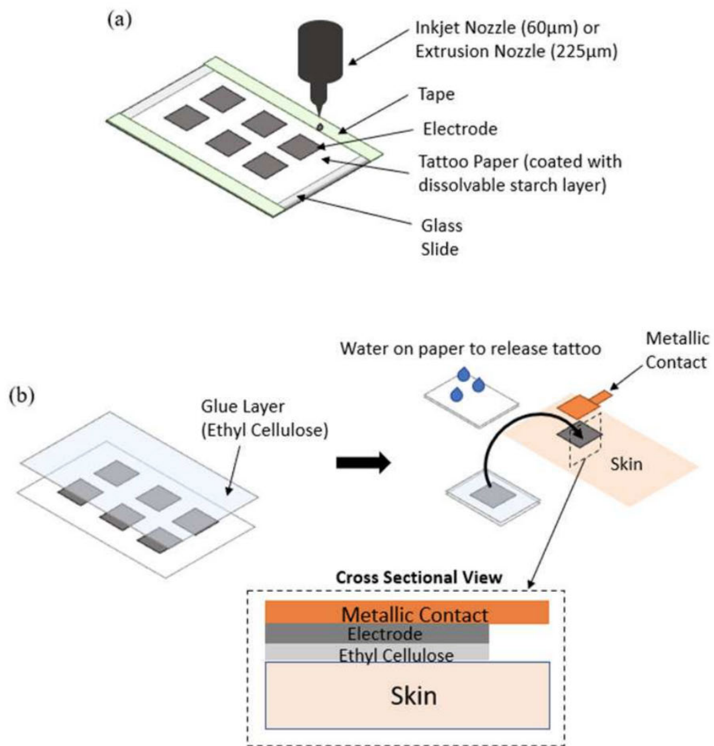

(a) Printed biomedical tattoo (©IEEE 2022). Y. El-Hajj, M. Ghalamboran, and G. Grau, "Inkjet and extrusion printed silver biomedical tattoo electrodes," in 2022 IEEE International Conference on Flexible and Printable Sensors and Systems (FLEPS), pp. 1–4, 2022.

(b) Printed smart facemask. Reproduced from [32] under the terms of the Creative Commons Attribution (CC BY) License.

Figure 2.12: Examples of extrusion printed devices from the literature using the NOVA.

- *Nozzle Size*: inner diameter of the nozzle [μm].

For a given ink and substrate combination, calibration of the NOVA is required to dial in the print parameters through a trial-and-error process. For example, more viscous inks may require a much higher dispense pressure and slower print speed than a thinner-viscosity ink. For the ink used in this thesis, Voltera recommends the profile in Table 2.3, however there is no information on how much the quality of the ink trace changes with variations in these process parameters.

Table 2.3: Voltera Conductor 3 recommended printing parameters.

Print Speed	650 mm/min
Print Height	60 μm
Dispense Pressure	700 arb. units
Nozzle Size	150-225 μm

2.3.0.1 | COMSOL Simulations

The simulations performed in this thesis use COMSOL Multiphysics version 6.1 [34], a finite element method (FEM) solver. A 2D or 3D model is discretized into a mesh of adjacent polygonal elements. Depending on the desired physics or coupled physics to be simulated, the governing partial differential equations (PDE) are solved numerically in each element. Given material properties and boundary/initial conditions, real-world physical phenomena can be simulated. The physics interfaces used in this thesis are the Solid Mechanics, Electric Currents, and the Heat Transfer in Solids modules. The governing PDEs are as follows. For Solid Mechanics, COMSOL solves:

$$\vec{\nabla} \cdot \mathbf{S} + \vec{F_V} = 0$$

where **S** is the Cauchy stress tensor (depicting internal volumetric stresses) and F_V is any volumetric force(s) acting on the body. The Electric Currents module solves:

$$\vec{E} = -\vec{\nabla} V$$
$$\vec{J} = \sigma \vec{E}$$

where $\vec{E}$ is the electric field, V is the electric potential, $\vec{J}$ is the current density, and σ is the charge density. The Heat Transfer in Solids module solves:

$$\vec{\nabla} \cdot (-k\vec{\nabla} T) = Q$$

where T is temperature, k is thermal conductivity, and Q is a heat source. The heat source used in this thesis is Joule heating, available with the Electromagnetic Heating multiphysics module, where Q is:

$$Q = \vec{J} \cdot \vec{E}$$

The main mode of heat flow is conduction, contained within the simulated devices, whereas radiative and convective are less likely to occur. This is because the devices are simulated in open air with no nearby thermal conductors or masses, although some negligible heat may be lost to the air via convection. Also used in this thesis is the Thermal Expansion multiphysics coupling, whose governing equation is:

$$\varepsilon = \alpha(T - T_0)$$

where ε is the strain, α is the coefficient of thermal expansion, and T_0 is a reference temperature.

3

DC Electric Field Sensor

The following chapter describes the development of a printed electronics DC electric field sensor. To begin with, a brief background on current DC electric field sensors from the literature is highlighted. Then, the chosen sensing topology's theory of operation and design equations are derived and presented. Next, the lithographic comparison design is shown, as well as the development of the printed electronics design. Within the printed electronics design, the silver ink used to fabricate the printed electronics sensor is characterized by finding the dependence of line width/height on print parameters such as print speed and dispense pressure. Young's modulus of the ink for use in simulation is also found. The designs are then simulated, fabricated and tested, and the chapter closes with a brief comparison to other MEMS DC electric field sensor designs.

3.1 | Background

DC electric field sensors are essential devices in the energy sector to assess risks of dangerous high voltage shocks to electrical and safety workers near high voltage direct current and low-frequency AC sources. Additionally, they are used as test equipment to ensure

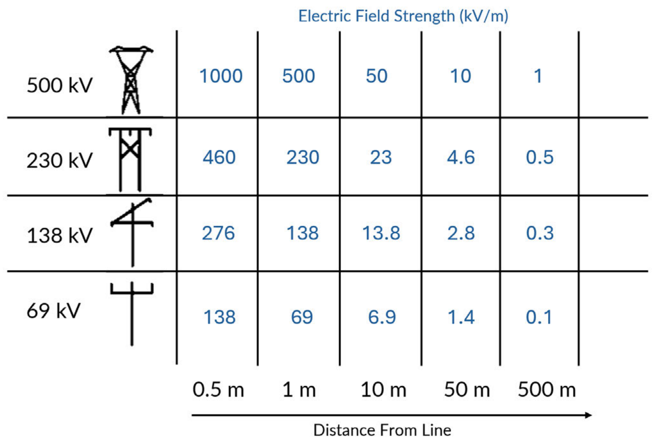

Figure 3.1: Electric field strengths as a function of distance from single transmission lines.

the fields produced by high voltage direct current (HVDC) transmission lines are within government-regulated levels [35]. For example, Fig. 3.1 shows electric field strengths for different HVDC sources, assuming a single-wire transmission line. For 60 Hz lines, the recommended level is around 5 kV/m for the general population [36].

Measuring DC electric fields is quite difficult in comparison to AC fields, which can easily be measured with low-cost off-the-shelf inductive sensors. This is due to several factors, such as skewed and/or drifting readings due to electrostatic induction of nearby conductors and dielectrics, charge accumulation and saturation, as well as atmospheric noise and ion currents in the air. Traditionally, the measurement of DC electric fields is carried out with electric field mills (Fig. 3.2). A grounded shutter periodically exposes and covers a conducting plate from the incident field, accumulating charge and conducting it away upon each cycle [37]. The time-varying induced charge is converted into a voltage and processed into a DC output proportional to the field strength. While effective and robust to many of the challenges faced with DC field measurement, they are large, cumbersome, and inefficient to operate. Additionally, the power-hungry DC motor may wear out over time, requiring routine maintenance and battery replacements. The electric field mill from [38] can measure electric fields down to 1.9 V/m.

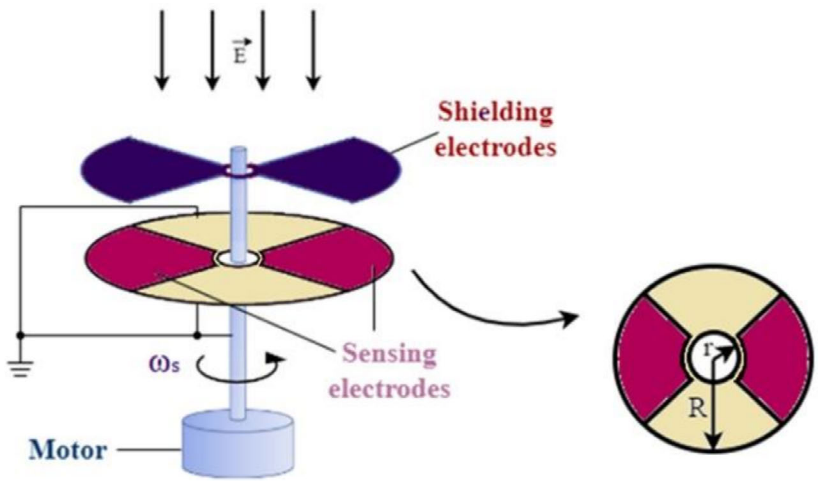

Figure 3.2: DC electric field mill. Reproduced from [37] under the terms of the Creative Commons Attribution (CC BY) License.

To combat the shortcomings of the electric field mill, there have been an advent of MEMS DC electric field sensors introduced in the last two decades [35]. These include MEMS electric field mills and electrostatic force-deflected sensors, with various methods of interrogation and readout.

The MEMS electric field mills work similarly to their macroscopic counterpart, cyclically exposing and covering a sense electrode with a grounded electrode. The shutter can be actuated either thermally using a thermal actuator mechanism [39] or electrostatically using a comb-drive which actuates based on the electrostatic force [40] (Fig. 3.3). In the thermal actuator design from [39], the shutter electrodes are connect to a bent-beam thermal actuator. When current is passed through it experiences in-plane bending which consequently moves the shutter to expose the sense electrodes to the field. This design can measure fields down to 42 V/m. For the electrostatic comb-drive electric field mill in [40], a large potential is placed on the actuator comb electrodes and pulls the shutter comb downward, exposing the sensing electrodes to the incident field. This device can measure fields down to sub-kV/m.

The MEMS electrostatic force-deflected sensors work by having a spring-suspended plate which feels an electrostatic force due to an incident electric field and deflects, and then sensing this deflection in some manner. Common methods of interrogation include optical and capacitive readout (Fig. 3.4[1]). In the optical case, such as the design from [41], a torsional spring suspended electrode is biased with asymmetric AC voltage. The DC voltage induced by the incident electric field modulates the amplitude of oscillation. A laser is shone obliquely upon the sensor and the reflected light is measured by a photo-diode to interrogate the oscillation amplitude and, thus, the electric field strength, measuring fields down to 3 V/m. The capacitive readout is simpler, which treats the moving electrode and a reference as a parallel plate capacitor, and a capacitance-to-digital converter is used to interrogate the change in capacitance as the electrode deflects due to the incident field [42]. This design allows for electric field measurements as small as 400 V/m.

In this thesis, the chosen design is the capacitively-interrogated force-deflected sensor, since the simple planar design facilitates the use of PE. Also, the MEMS design in [42] fabricated via lithography offers a good baseline for comparison for the PE version explored in this chapter.

[1] *(a) reproduced from [41] under the terms of the Creative Commons Attribution (CC BY) License.*

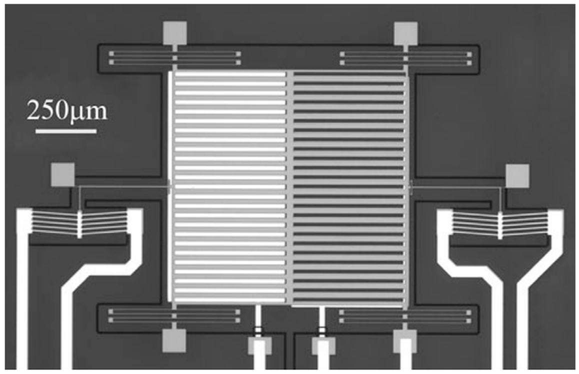

(a) Thermally-actuated MEMS electric field mill (©IEEE 2007).

B. Bahreyni, G. Wijeweera, C. Shafai, and A. Rajapakse, "Design and testing of a field-chopping electric field sensor using thermal actuators with mechanically amplified response," in TRANSDUCERS 2007 - 2007 International Solid-State Sensors, Actuators and Microsystems Conference, pp. 1397–1400, 2007.

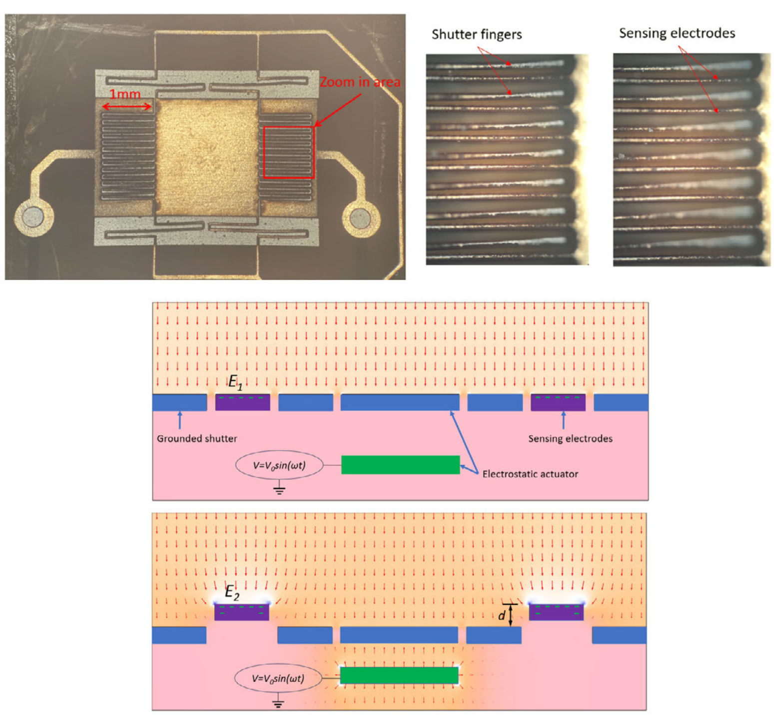

(b) Electrostatic comb-drive MEMS electrical field mill. Reproduced from [40] under the terms of the Creative Commons Attribution (CC BY) License.

Figure 3.3: MEMS electric field mills.

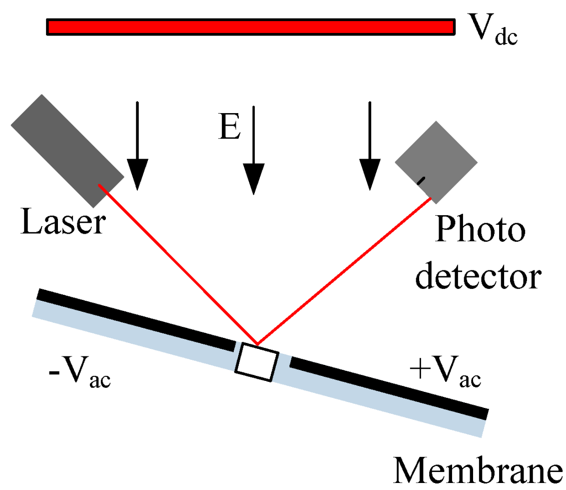

(a) Torsional force-deflected electric field sensor with optical readout. Reproduced from [41] under the terms of the Creative Commons Attribution (CC BY) License.

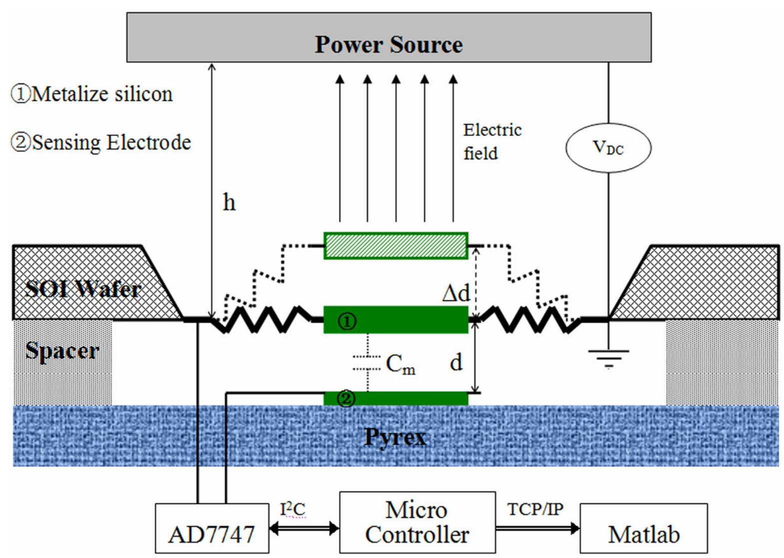

(b) Force-deflected electric field sensor with capacitive readout (©IEEE 2013).

Tao Chen, "MEM electric field sensor using force deflection with capacitance interrogation," 2013 IEEE Power & Energy Society General Meeting, Vancouver, BC, pp. 1-4, 2013.

Figure 3.4: MEMS force-deflected electric field sensors.

3.2 | Theory and Design

3.2.1 | Theory of Operation

The capacitive force-deflected DC electric field sensor (Fig. 3.4 (b)) selected for this thesis operates as follows. A grounded, spring suspended electrode with area A experiences an electrostatic force due to the incident electric field E generated by a nearby voltage source V_{DC} a distance h away:

$$F_E = \frac{1}{2}\epsilon_0 A E^2 = \frac{1}{2}\frac{\epsilon_0 A V_{DC}^2}{h^2} \tag{3.1}$$

where ϵ_0 is the electrical permittivity of free space (8.85×10^{-12} F/m). The spring-suspended electrode has a spring constant k associated with it, and, when a force is applied, it deflects a distance Δd as per Hooke's law:

$$F_S = k\Delta d \tag{3.2}$$

After the spring-suspended electrode transiently deflects due to the introduction of the incident field, it reaches a steady-state equilibrium where the electrostatic force is balanced with the spring force:

$$k\Delta d = \frac{1}{2}\epsilon_0 A E^2 \tag{3.3}$$

The spring-suspended and reference electrodes form a parallel plate capacitor, with initial capacitance C_i given by:

$$C_i = \frac{\epsilon_0 A}{d} \tag{3.4}$$

Between the spring-suspended and reference electrodes, there exists a change in capacitance ΔC upon deflection (ignoring fringing):

$$\Delta C = \epsilon_0 A(\frac{1}{d + \Delta d} - \frac{1}{d}) \tag{3.5}$$

Combining this with Eq. 3.3 yields a change in capacitance for an incident electric field, given an initial capacitance with no field present of C_i:

$$\Delta C = \frac{C_i^2}{\frac{2k}{E^2} + C_i} \tag{3.6}$$

Equation 3.6 describes the sensitivity curve of the sensor, as it describes how the output ΔC changes with an input E. One can see that the curve is inherently non-linear, as ΔC changes in proportion to E^2.

3.2.2 | Design Parameters & Constraints

From Eq. 3.6, the most important parameters to consider are spring constant k and initial capacitance C_i. Since k depends on the physical dimensions and Young's modulus, and since C_i depends on electrode area A and initial separation d, these also must be considered. For PE to work, given that the Voltera NOVA is being used, the smallest features must be >150 μm, and thicknesses must be >15 μm.

3.2.2.1 | Springs

Rectangular springs for MEMS design generally follow the same relationship, given their thickness t, length l, width w, and Young's modulus Y:

$$k \propto Yw(\frac{t}{l})^3$$

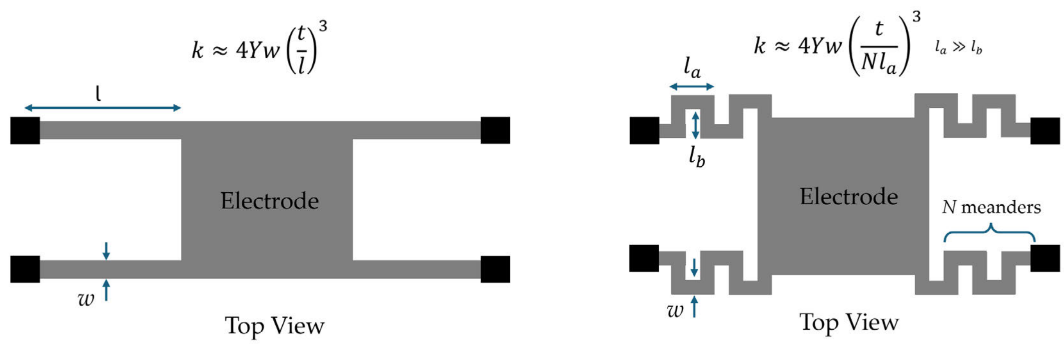

Figure 3.5: MEMS spring geometries for fixed (left) and serpentine (right).

The candidate moving electrode spring geometries were either a fixed or a serpentine flexure [43] (Fig. 3.5). This is because they are both relatively simple to print and laser-cut as well as mimic the design of the lithographic counterpart.

3.2.3 | Lithographic MEMS Design

The MEMS design chosen for comparison is the design of Fig. 3.4 (b) from [42]. Fig. 3.6 shows the fabricated device and its top spring-suspeneded electrode, utilising a serpentine flexure spring geometry. The electrode is 1.15 $\times$ 1.15 mm, spring width w is 20 μm, and is fabricated on 5 μm single-crystal silicon with a thin film of 200 nm copper. The author found the experimental spring constant k of the suspended electrode to be 0.136 N/m, and used an initial separation d of both 27 μm and 2 μm. Table 3.1 summarises the design of the lithographic MEMS sensor.

Table 3.1: MEMS DC electric field sensor lithographic design.

Electrode Area A $[m^2]$	1.32×10^{-6}
Spring Constant k $[N/m]$	0.136
Initial Separation d $[\mu m]$	$2, 27$
Spring Width w $[\mu m]$	20
Thickness t $[\mu m]$	5.2

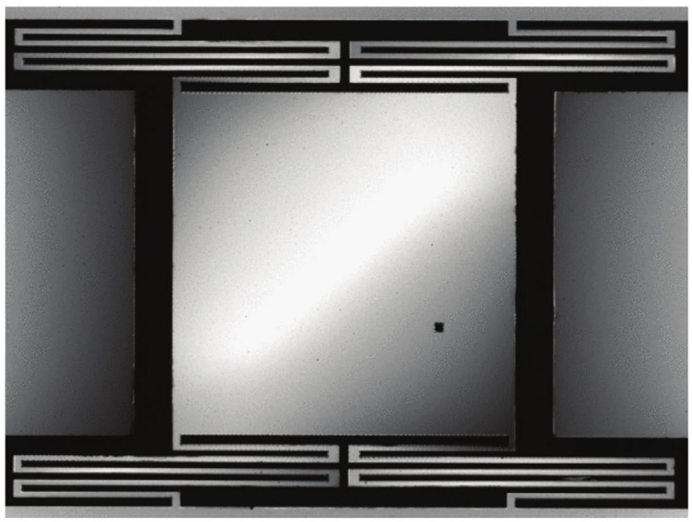

Figure 3.6: MEMS DC electric field sensor top view (©IEEE 2013). Tao Chen, "MEM electric field sensor using force deflection with capacitance interrogation," 2013 IEEE Power & Energy Society General Meeting, Vancouver, BC, pp. 1-4, 2013.

3.2.4 | Printed Electronics Design

The design for the PE version of the DC electric field sensor took a similar form as the lithographic counterpart, but needed to be scaled up to make PE allowable. The limiting factor in the design, in context of the Voltera Conductor 3 ink's 200 μm minimum line width, was the width of the springs, since they were the smallest feature. In order to maximize ΔC for a given E field and C_i, the spring constant should be made as small as possible by Eq. 3.6. This means setting w to be 200 μm, which is 10$\times$ the lithographic version. Also, the thinnest readily available PI substrate was 25 μm film [44], and, in addition to a minimum printed ink thickness of 15 μm, this brought the theoretical thickness to 40 μm.

To get a feel for roughly how big the electrode should be, a desired response was first chosen somewhat arbitrarily. Assuming an initial distance of 100 μm and a spring constant of roughly 0.5 N/m, an acceptable response would be 0.5 pF per 50 kV/m change in electric field. Given these, an area of 0.00016 m^2 was determined from Eq. 3.6, corresponding to approximately a 1 cm $\times$ 1 cm electrode. Note that the spring constant of 0.5 N/m was a generous initial guess. Therefore, for simulation, a 1 cm square electrode was chosen.

Next, the spring geometry was chosen. More specifically, the length of the springs was the only parameter left unknown. Again, to get a general feel for how long they should be, given the arbitrary spring constant of 0.5 N/m, width 200 μm, thickness 40 μm, and ignoring the Young's modulus of the ink, the spring length was found to be about 1 cm for a fixed flexure. Making the fixed spring into a serpentine spring only helps the sensor's response, as it effectively increases the length and thus reduces the spring constant.

Fig. 3.7 shows an initial mock-up of the fixed and serpentine spring-suspended electrodes, ready for simulation. The devices in the figure were drawn using KiCad electronic CAD and PCB layout software [45], as the Voltera NOVA requires gerber files in order to print the design.

In addition to the spring-suspended electrode, the device also required a reference electrode. This was designed to be a simple 1 $\times$ 1 cm square with contact pad and connecting trace (Fig. 3.8) to be printed on 83 $\times$ 109 mm FR4 rigid circuit board material, measuring 1.6 mm thick. The spring-suspended electrode would then sit atop the reference electrode and FR4, and to hold it in place, another similar piece of FR4 would be required to sandwich it. This was simply a piece of FR4 with a 24.85 $\times$ 24.85 mm 'window' cut out of it (Fig. 3.9). Fig. 3.10 shows a mock-up of the sensor's test setup for the case of the serpentine spring

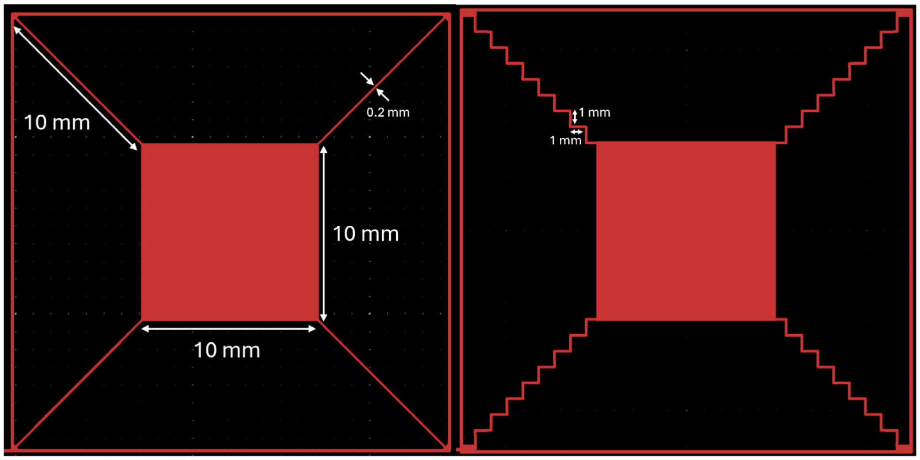

Figure 3.7: Fixed (left) and serpentine (right) spring-suspended electrode designs.

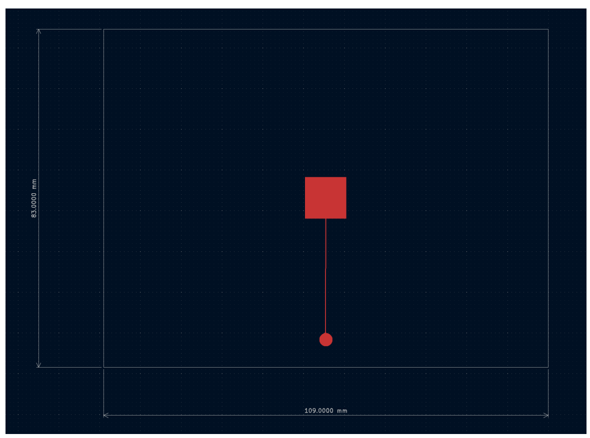

Figure 3.8: Reference electrode design in KiCad.

electrode, along with a side-on view of the stack-up complete with 100 μm PI spacer to set C_i. The next step was to find some important and previously unknown parameters of the ink, such as Young's modulus, printed line height, and printed line width.

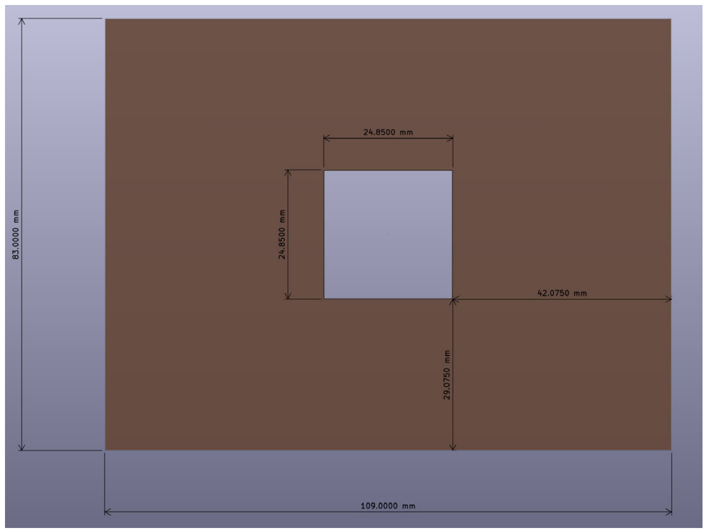

Figure 3.9: Top board required to hold spring-suspended electrode in place.

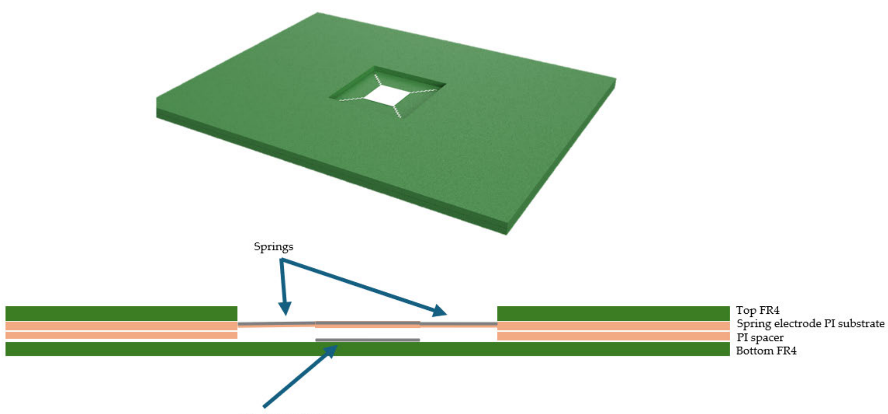

Figure 3.10: Mock-up of printed electric field sensor test setup (top) and stack-up (bottom).

3.2.4.1 | Young's Modulus of Ink

To find the Young's modulus of the cured silver ink for simulation, a 3.2 mm $\times$ 10.2 mm cantilever was made by printing silver ink on 50 μm thick PI and cured for 20 minutes at 120 °C. To bring the ink thickness to about the same thickness as the PI (so that the Young's modulus of the ink has a measurable effect), the design was printed 3 times over itself, yielding a thickness of 41.2 μm, as measured by a KLA P7 Profiler [46]. The same cantilever design was made in COMSOL software using the Solid Mechanics module.

A metal plate was placed a distance d below the cantilever. The cantilever was electrically grounded, and the metal plate biased to a voltage V of 600 VDC with a Stanford Research Systems PS310 HVDC power supply [47]; everything was placed beneath a Leica DM6-M microscope [48]. The electrostatic force present between the fixed cantilever and the metal plate below causes the cantilever to bend downwards towards the plate [49]:

$$F = \frac{1}{2}\frac{\epsilon_0 LWV^2}{d^2} \tag{3.7}$$

where $\epsilon_0 = 8.85 \times 10^{-12}$ F/m is the permittivity of free space, L is the length of the cantilever and W is the width. This force was found to be 1.8×10^{-5} N, given an initial separation d of 2.094 mm as measured with the Leica microscope. The same force was applied as a Boundary Load in COMSOL on the cantilever model. Under uniform load, the edge of a cantilever beam deflects by δ [50]:

$$\delta = \frac{FL^3}{8YI} \tag{3.8}$$

where Y is the Young's modulus and I is the moment of inertia. This deflection was found experimentally to be 5 μm using the Leica microscope, and the Young's modulus value of the ink in simulation was swept until the cantilever model also deflected 5 μm. This yielded a value of 1.781 GPa, assuming a fixed Poisson's ratio of 0.37 [51] (that of pure silver) and a Young's modulus value for PI of 3.1 GPa. Fig. 3.11 shows a schematic of the test setup, the printed and released device, and the associated COMSOL model.

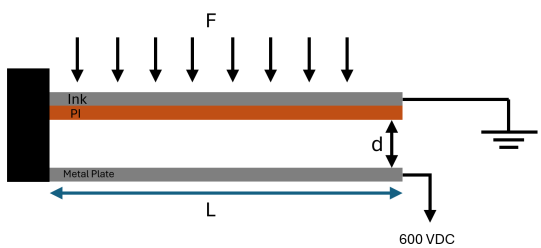

(a) Uniformly-loaded electrostatically actuated cantilever.

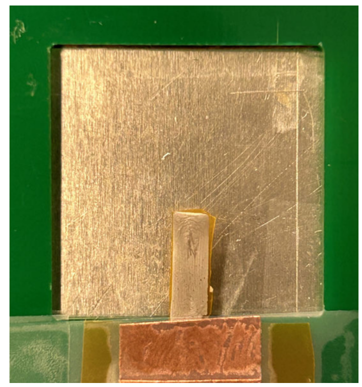

(b) Printed cantilever with metal plate below.

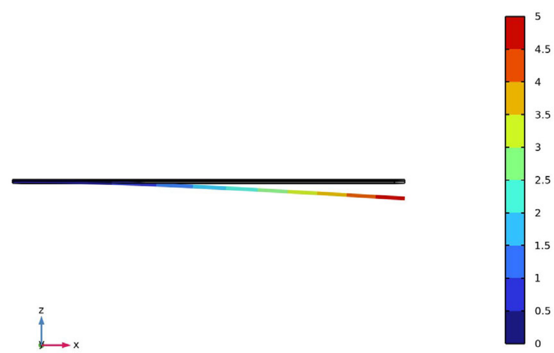

(c) Cantilever COMSOL model (deflection in μm, side view).

Figure 3.11: Printed cantilever test structure for determining Young's modulus of Conductor 3 ink.

3.2.4.2 | Printed Line Width and Height

The printed line width depends mainly on 3 printing parameters: nozzle size, print speed, and dispense pressure. Thus, an experiment was designed and carried out to investigate that dependence. In order to do so, an array of 1 cm long lines were printed at different pressures and speeds, as shown in Fig. 3.12. The pattern in Fig. 3.12 was then printed on 125 μm thick PI with a 225 μm nozzle and a print height of 60 μm, varying dispense pressure and print height but keeping all else constant as per Table 2.3. The ink was cured at 120 °C for 20 minutes.

Next, the printed ink array was cut into its constituent elements and labeled. Then, each ink trace was analyzed using a KLA P7 Profiler to determine its printed line width and height. Fig. 3.13 shows the raw data collected with the profiler, presented to more intuitively match the actual printed array.

From the plots, it can be seen that line height depends linearly on both print speed and dispense pressure, ranging from 4.7 μm to 29.9 μm. Line width, on the other hand, has less dependence on print speed and is mostly a function of dispense pressure, ranging from 159 to 445 μm in the tests.

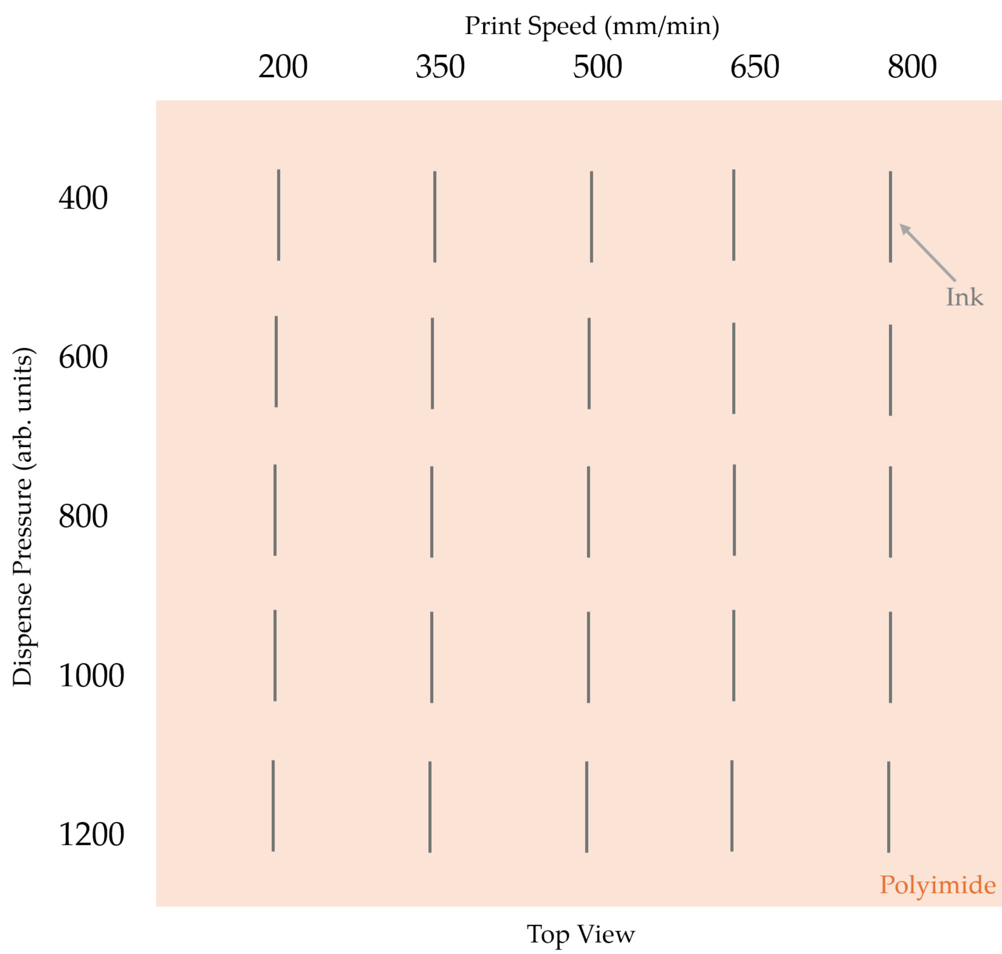

Figure 3.12: Printed line array for dependence of line width and height on print pressure and speed.

(a) Line width vs. dispense pressure and print speed.

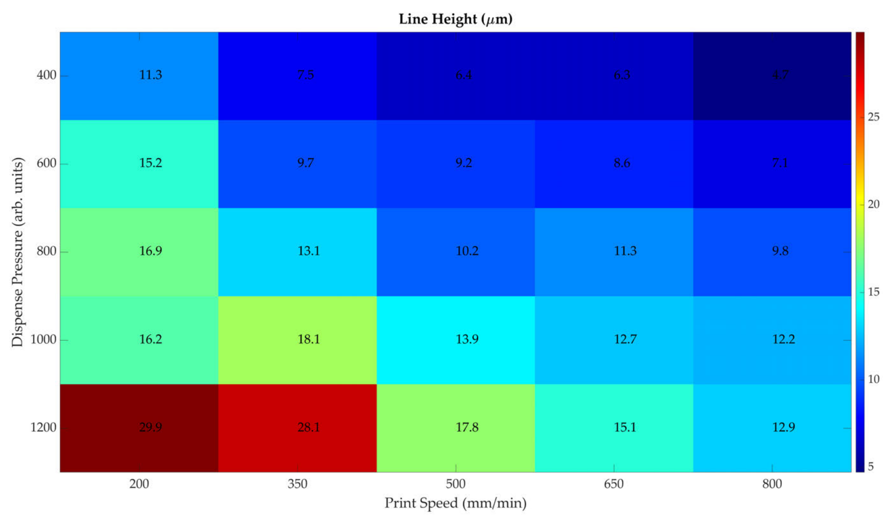

(b) Line height vs. dispense pressure and print speed.

Figure 3.13: Line width and height raw values.

3.3 | Simulation

With some useful parameters and behavior of the cured Voltera Conductor 3 ink known, the next step was to simulate the devices in COMSOL. This was done by converting the gerber file of each design - fixed and serpentine springs - and converting them into DXF files. Then, the DXF file was imported into COMSOL as a 2D layer which was then extruded in the z-direction to the specified total thickness. Subsequently, the 3D body was split in x-y plane in order to simulate the silver ink on top of the polyimide. Table 3.2 shows the simulation parameters.

Table 3.2: Printed DC electric field sensor simulation parameters.

Parameter	**Fixed**	**Serpentine**
Electrode Side Length	1 cm	1 cm
Spring Length	1 cm	1.48 cm (eff.)
Spring Width	0.2 mm	0.2 mm
Applied Boundary Force	$1 \times 10^{-5}\,\hat{k}$ N	$1 \times 10^{-5}\,\hat{k}$ N
Mesh Size	Normal	Normal

Next, a Boundary Load condition was placed on the top surface of the ink, and a Fixed Constraint condition placed at the ends of each of the four springs. A normal-sized, physics-controlled mesh was then generated. A time-independent study was then executed for each design. Then, a displacement pre-defined plot was selected to show the force-induced deflection of the electrode. Fig. 3.14 shows each of the deflections.

The fixed spring deflected 51.03 μm and the serpentine spring 102.34 μm, resulting in spring constants of 0.196 N/m and 0.098 N/m, respectively, by Eq. 3.2. The aim was to keep the spring constant small while the electrode area large in order to obtain a greater change in capacitance for a given electric field, and the serpentine spring offered a 50% reduction in spring constant compared to the fixed spring electrode while keeping the area constant.

For an initial electrode separation of 100 μm, and thus an initial capacitance C_i of 8.85 $\times 10^{-12}$, the response curve of ΔC vs. E was normalized and plotted for each design and is shown in Fig. 3.15. It can be seen that the response of the serpentine spring electrode is roughly 35% higher than that of the fixed for the same field. Also, both designs avoid saturation in the region of 0-250 kV/m, and their response is mostly linear in the region >50 kV/m.

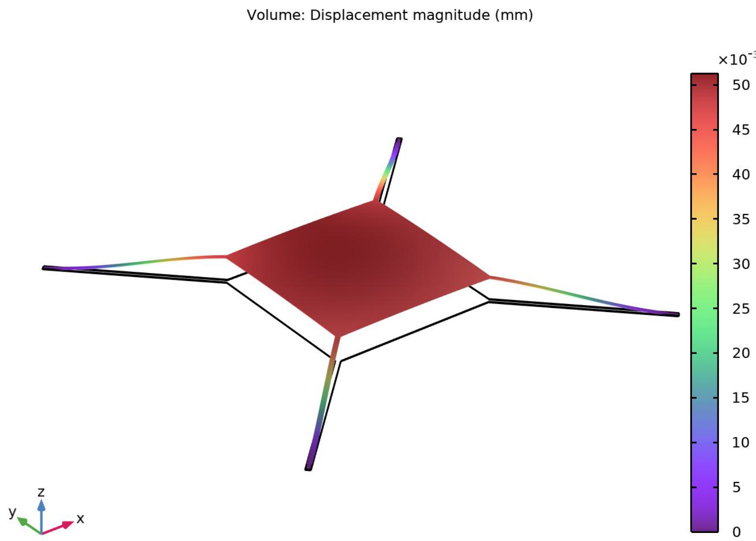

(a) Fixed spring.

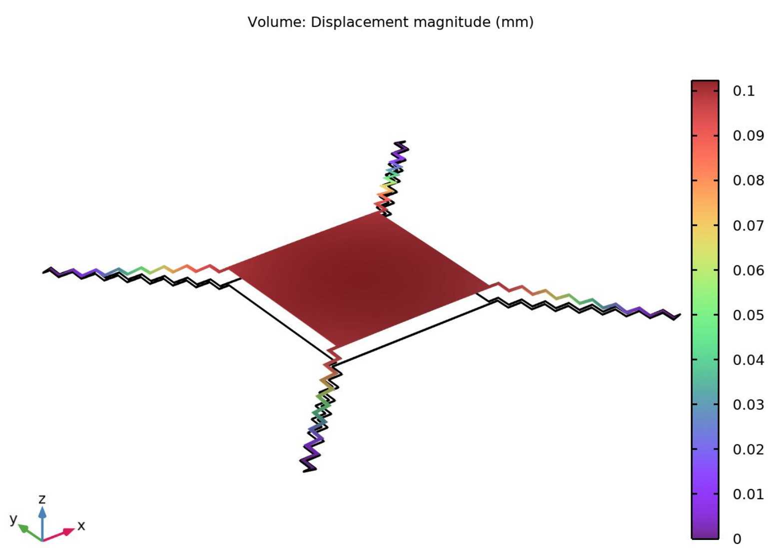

(b) Serpentine spring.

Figure 3.14: Simulated deflections of each spring design.

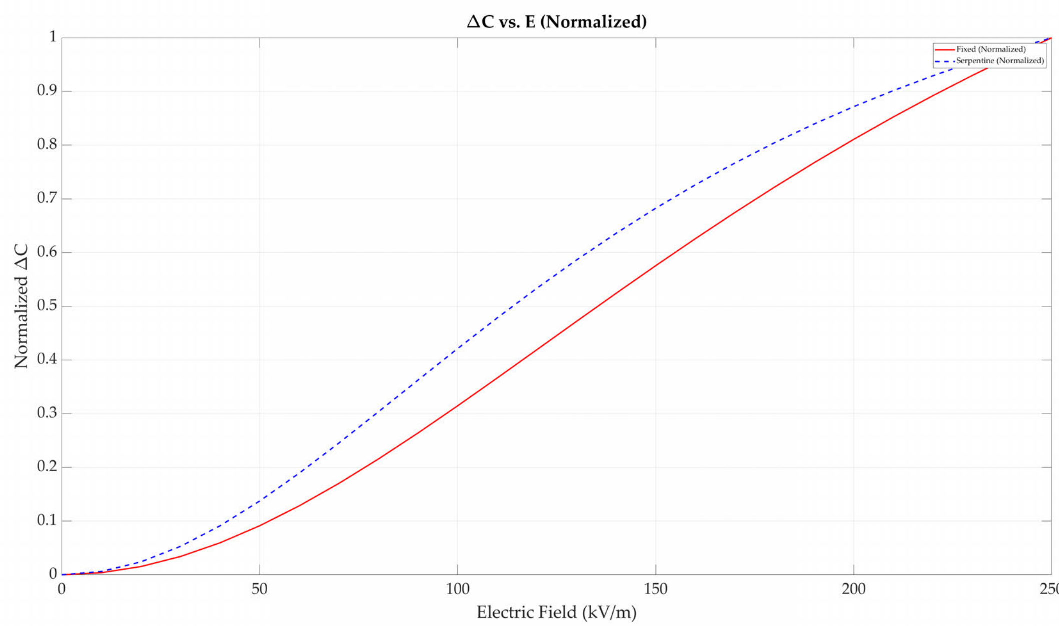

Figure 3.15: Simulated normalized response of fixed and serpentine spring electrodes.

3.4 | Fabrication

The two designs of Fig. 3.7 were uploaded to Voltera's proprietary browser-based software for interfacing with the NOVA printer. Firstly, the 25 μm PI was cut into a 10 $\times$ 5 cm rectangular piece and placed on the vacummed printing stage. Next, the substrate was aligned and probed by the NOVA's smart probe, which creates a map of the z-height to compensate for relatively large undulations in the surface topography of the substrate. NOVA uses a downward-facing camera and overlays the gerber file in the live feed to allow the user to align the print on the substrate accurately. Both the probe and dispense head first calibrate themselves by touching a small thumbscrew touch sensor button next to the calibration plate. This compensates for lash in the stepper motors as well as zeros the coordinates for the gantry head.

Table 3.3: Printed DC electric field sensor print parameters.

Dispense Pressure	750 (arb. units)
Nozzle Size	150 μm
Print Speed	650 mm/min
Print Height	60 μm
Cure Temperature	120 °C
Cure Time	20 min

After probing and aligning the substrate, the ink cartridge was loaded into the NOVA's smart dispenser, followed by the 150 μm nozzle. A nozzle size of 150 μm was chosen as they were readily available and sold by Voltera and were below the desired 200 μm printed line width, considering the width aspect ratio of the nozzle. The print height was set to 60 μm. The thumb screw at the top of the dispenser, which manually controls the plunger mechanism, was then turned until the ink *just* begins to come out the nozzle, then backed-off about a 1/4-turn. This primes the nozzle with ink and pushes out any air in the system.

Then, the dispenser is mounted on NOVA's gantry. Upon connection, the smart dispenser begins heating the ink to 35 °C. This is a preset value that allows the ink to flow at its specified viscosity (15 Pa s for Voltera Conductor 3). Since the ink is stored in a refrigerator, it may take a while for the ink to warm up. Therefore, the dispenser has a built-in heater element to expedite this process. Once the ink was heated, the dispense head then needed to be calibrated. This involves repeatedly printing 3 parallel lines, approximately 2 cm in length, on NOVA's calibration plate (Fig. 3.16) until the print quality is satisfactory.

Figure 3.16: NOVA dispense calibration plate (left, circled in red); calibration pattern on plate (right).

Once calibrated, the design from the gerber file was printed; since the dispenser is primed and calibrated, this step usually only needs to be performed once for most design topologies. Initially, a dispense pressure of 600 was chosen, however, in the serpentine spring section some breaks in the ink formed due to the nozzle moving too quickly through the jagged pattern, with the ink not coming out fast enough. This was partially solved by at first decreasing the print speed from 650 to 400 mm/min, but this resulted in spreading of the ink; too much ink coming out of the nozzle relative to its motion through the serpentine pattern. Then, it was decided that perhaps the best option was to keep the print speed at 650 mm/min, but instead slightly increase the dispense pressure until no breaks formed, and this occurred at a pressure of 750. In between failed prints, the ink easily wiped off the PI substrate with IPA and tissue paper. After the dispense procedure concluded, the substrate was placed in a box oven at 120 °C for 20 minutes for curing. More prints were made by simply swapping out the finished print for a fresh substrate. Fig. 3.17 shows the process flow.

Some issues encountered in printing on the NOVA are outlined below, along with their solutions:

- **Problem**: The substrate moving slightly when the probe quickly touched down and took off again to take a measurement. **Cause**: This was because the size of the substrate relative to the expanse of the vacuumed printing stage was too small, and so it could not generate sufficient suction to hold it in place. **Solution**: This was solved by placing scrap pieces of PI around the target substrate on the printing stage.
- **Problem**: Line breaks after repeated printing. **Cause**: This was due to the nozzle losing its prime due to small air pockets in the ink cartridge, long after the initial priming. **Solution**: This was solved by removing and re-priming the cartridge; one could also increase dispense pressure by 100-500 arb. units, depending on severity.
- **Problem**: Gantry head stepper motors stall or skip repeatedly. **Cause**: This was because the motors can become misaligned over time and use. **Solution**: This was solved by taking the top plate off which reveals the steppers, loosening their mounting screws, re-aligning them to be centered, then tightening them back down.
- **Problem**: Dispense head or probe failed to calibrate. **Cause**: This was found to be due to the thumbscrew touch sensor button being loose. **Solution**: The thumbscrew touch sensor was tightened down to finger-tight.

- **Problem**: Ink getting past the plunger inside the cartridge-dispenser assembly. **Cause**: This was due to the o-ring on the plunger losing its seal by being either coated in dried ink and becoming rigid, or becoming disfigured after many uses and losing its seat. **Solution**: The o-ring was cleaned in IPA; alternatively, it could be replaced.

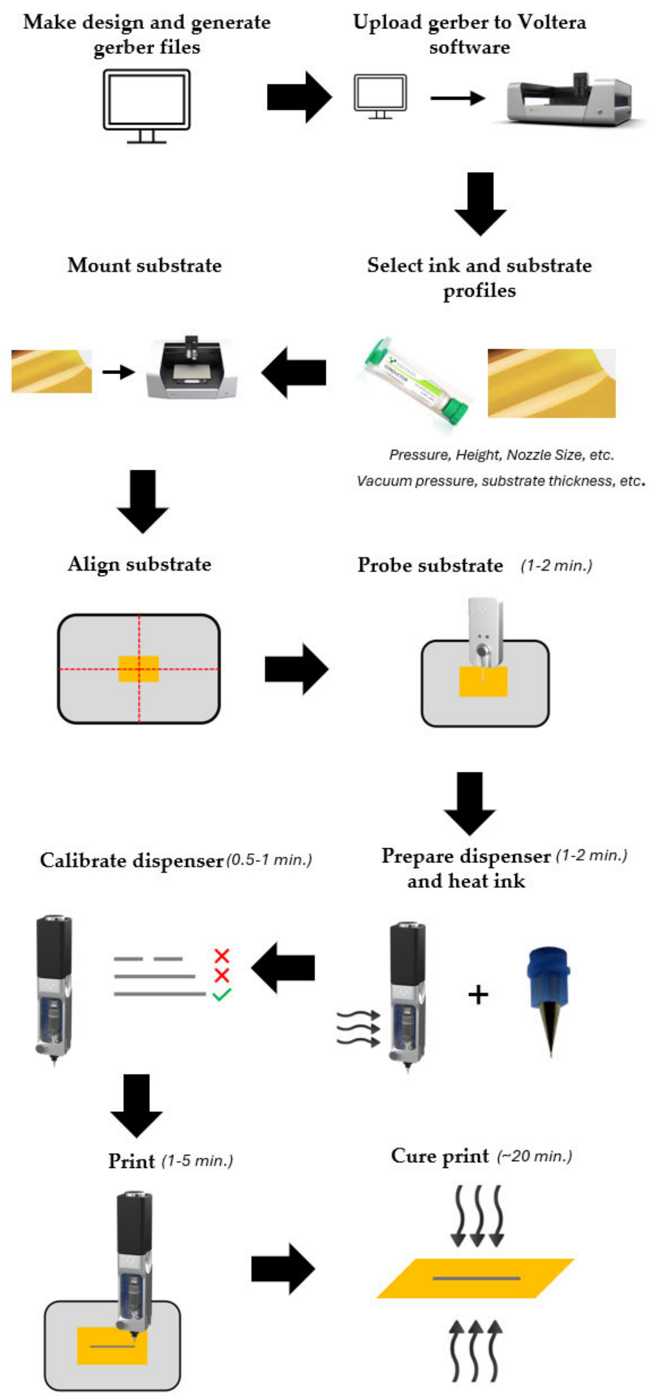

Figure 3.17: Printing process on Voltera NOVA.

The resulting print of both devices, fixed and serpentine, is shown in Fig. 3.19. The trace extending outward to the left is the contact pad for grounding the spring suspended electrode, as seen in Fig. 3.4 (b). The quality of the print was characterized by 3D profilometry, using a KLA P7 Profiler. Three consecutive 2D scans were stitched together in Mountains8 Apex imaging software [52] to create a 3D profile of one of the printed ink traces. The result of this is shown in Fig. 3.18. The printed traces ended up having an average height of 21 μm and width of 325 μm. These values did not agree with the experimental data in Fig. 3.13; however, those plots do not serve as a definitive guide or look-up table, but instead illustrate how printed line width and height is relatively affected by dispense pressure and print speed.

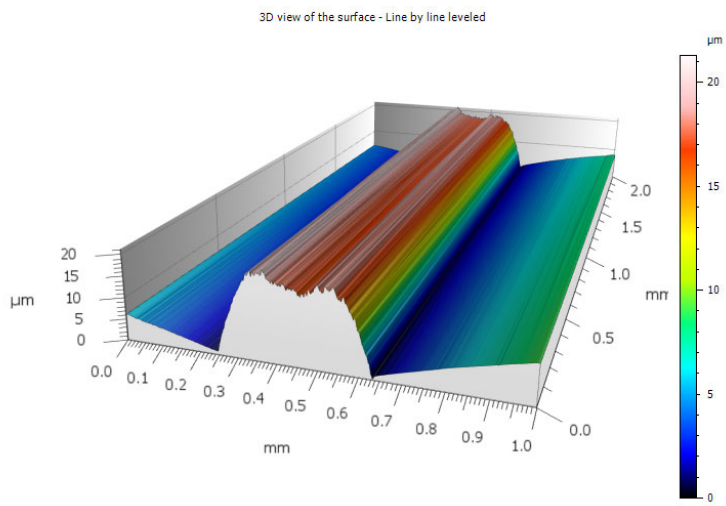

Figure 3.18: 3D scan of printed trace.

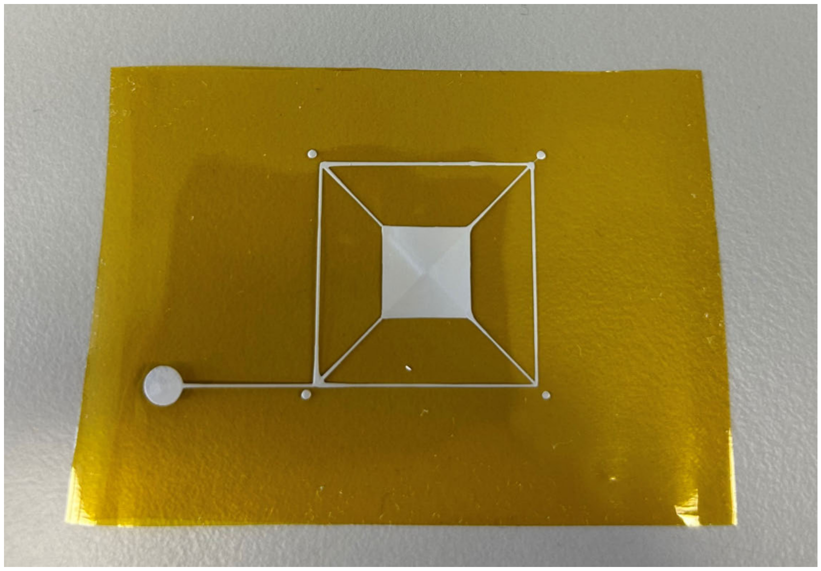

(a) Fixed spring post-print.

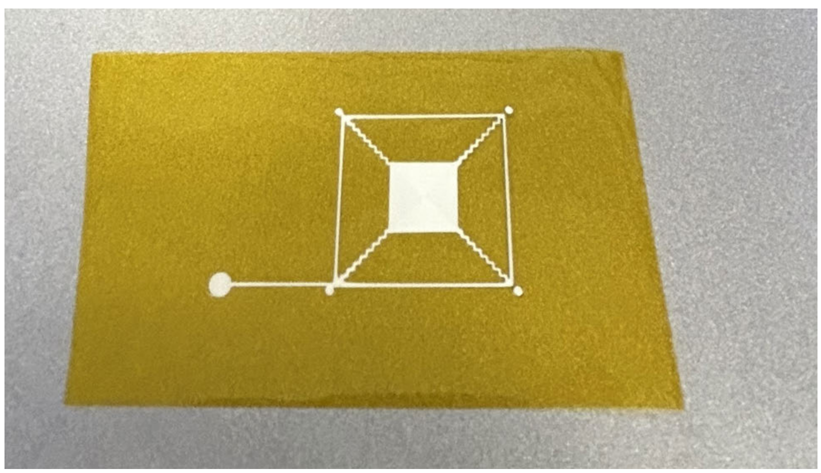

(b) Serpentine spring post-print.

Figure 3.19: Post-print for fixed (left) and serpentine (right) spring-suspended electrodes.

After inspection of the prints, it was ready to release the electrode and springs. This was done by laser cutting with a Oxford Series-A laser, which is a 355 nm, 32 mW laser pulsing at 400 Hz. The design in KiCad was outlined to create the cut path for the laser, which was then imported into AlphaCam software [53] to generate G-code for the stepper motors which direct the laser. The generated G-code file is then imported into Oxford's laser micro-machining software. With cut speed set to 1 mm/s and laser power set to 5% (1.6 mW), approximately 30 cut passes were required to cut through the 25 μm thick PI substrate. Fig. 3.20 shows the released fixed-spring electrode. It was evident that, on the springs, some ink traces de-laminated from the substrate. Only two of the four springs de-laminated for the fixed spring, and one for the serpentine spring, so no open circuits were accidentally created. However, it was clear that surface prep should have been performed on the PI substrate, especially for devices with small deformable structures such as springs, to aid in adhesion.

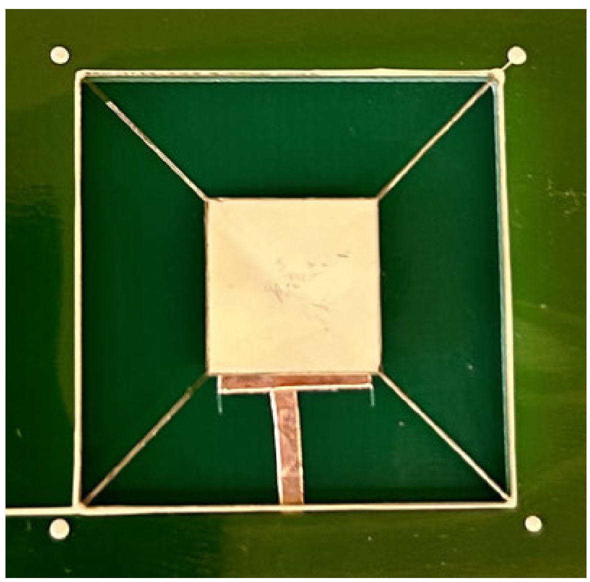

Figure 3.20: Fixed spring-suspended electrode post laser cutting.

The reference electrode design of Fig. 3.8 was loaded into NOVA software and printed on 1.6 mm thick FR4 rigid circuit board material. This followed virtually the same process as Fig. 3.17, except for the mounting procedure; rigid materials are mounted to the NOVA printing area with thumb screws instead of the vacuum stage. All print settings were exactly the same as with the electrodes on PI otherwise, using Voltera Condcutor 3 again.

3.5 | Testing and Results

3.5.1 | General Test Setup

The test setup of Fig. 3.10 was built in the lab, shown in Fig. 3.22. Both types of electrodes were placed between the two pieces of FR4, and a 100 μm piece of PI was placed between the spring-suspended and reference electrodes. Conductive copper tape was used to make contact with the pad on the spring-suspended electrode substrate for grounding, which then made contact at a SMB connector. The reference electrode was also connected to an SMB connector. This allowed the use of shielded cabling, which offered reduced noise and parasitic capacitance due.

The two wires, signal and ground, were connected to an Analog Devices AD7747 capacitance-to-digital converter chip [54]. The chip can measure up to 17 pF in a single-ended configuration, with a theoretical resolution of 20 aF. It works by exciting the capacitor with an AC voltage and measuring the response to infer capacitance. The chip was interfaced with an STM32F401RE microcontroller [55], for which a firmware driver for the AD7747 chip was written in low-level C++ [56]. At first, just the chip on a breadboard was used, but the breadboard and associated wiring presented too much parasitic capacitance to the chip, at some points saturating it. Therefore, the EVAL-AD7747 board was used, a PCB manufactured by Analog Devices that has on-board SMB connectors (Fig. 3.21). The shielding is connected to the SHLD pin of the AD7747, which sends a signal identical to the capacitance excitation signal, effectively isolating the signal wire and preventing it from capactively coupling to any nearby conductors (i.e. wires in the circuit). The AD7747 was configured with a 124 ms ADC conversion time, lending a bandwidth of approximately 4 Hz via Nyquist sampling theorem. The EVAL-AD7747 communicated over I^2C communication with the microcontroller. The microcontroller then communicated with a serial terminal on a laptop via UART over a USB cable for data collection, processing, and analysis. The sample rate of the AD7747 was set to 45 Hz. Fig. 3.23 shows a schematic of the test setup.

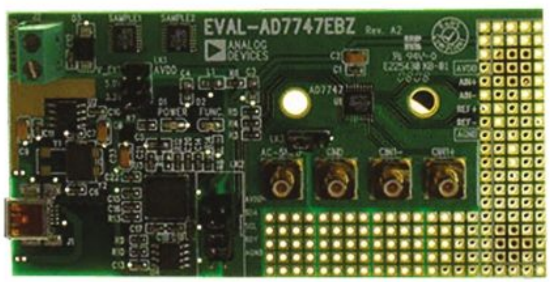

Figure 3.21: Analog Devices EVAL-AD7747

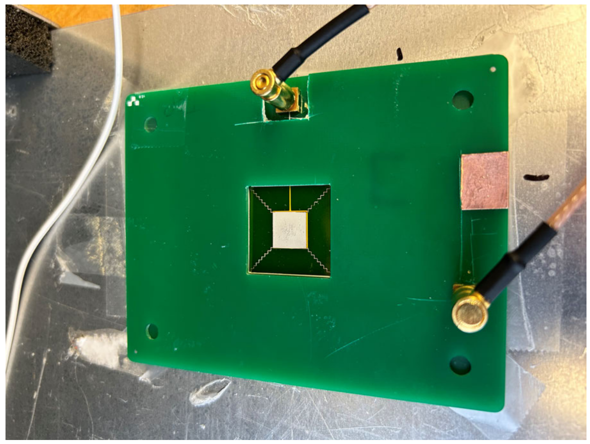

Figure 3.22: Lab test setup (serpentine spring electrode shown).

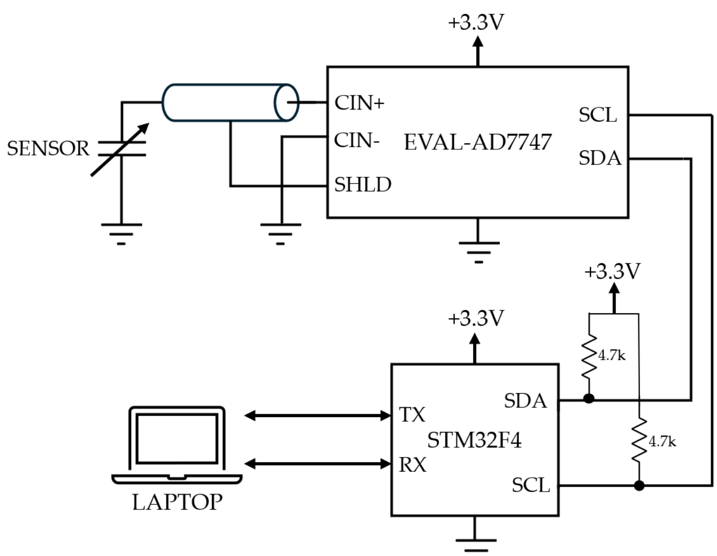

Figure 3.23: Schematic of test setup.

3.5.2 | Serpentine vs. Fixed Spring Tests

In order to see how the two designs compare, each was loaded into the test setup rigging and a metal plate was placed atop the top FR4 board (Fig. 3.24) and biased to 600 V with respect to the grounded spring-suspended electrode, using a HVDC power supply. Since the metal plate was 1.6 mm away from the electrode, this meant that the field strength was around 312 kV/m. Fig. 3.25 shows the two responses for toggling the 312 kV/m field.

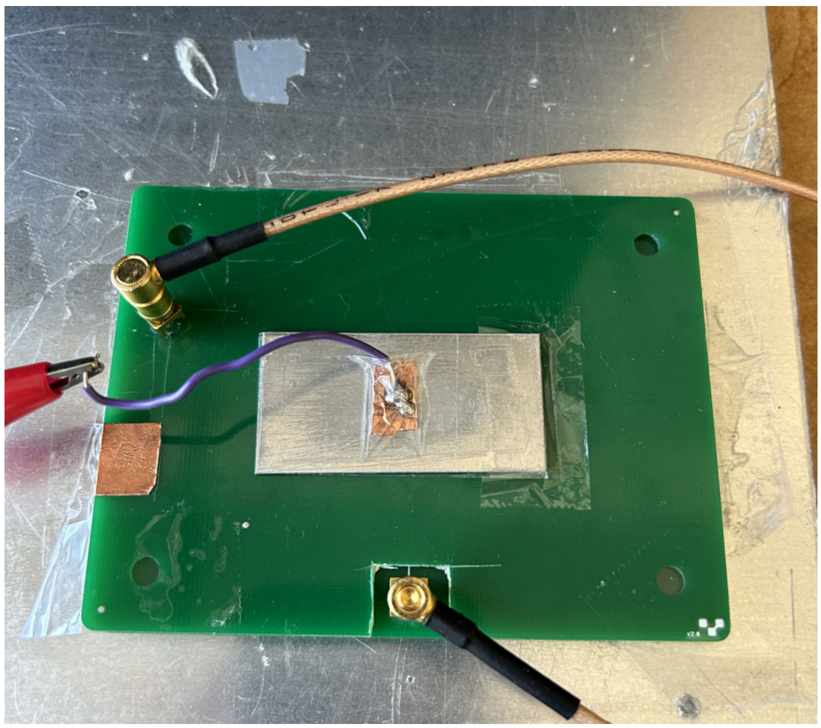

Figure 3.24: Test setup with HVDC biased metal plate.

The serpentine spring electrode had better sensitivity, with a ΔC of about 0.37 pF when the field was turned on, compared to 0.27 pF for the fixed spring. This was an increase in sensitivity by about 37% which agreed with simulation. Also, the serpentine spring had superior signal-to-noise ratio (SNR), given by:

$$SNR(dB) = 20 \log_{10} \frac{\bar{x}}{\sigma_{noise}}$$

where $\bar{x}$ is the time-average of the signal and σ_{noise} is the standard deviation of the noise. The serpentine spring possessed a SNR of 69.77 dB, whereas the fixed spring had 58.49 dB. Therefore, moving forward, only the serpentine spring was used for further study. The results were published in [57].

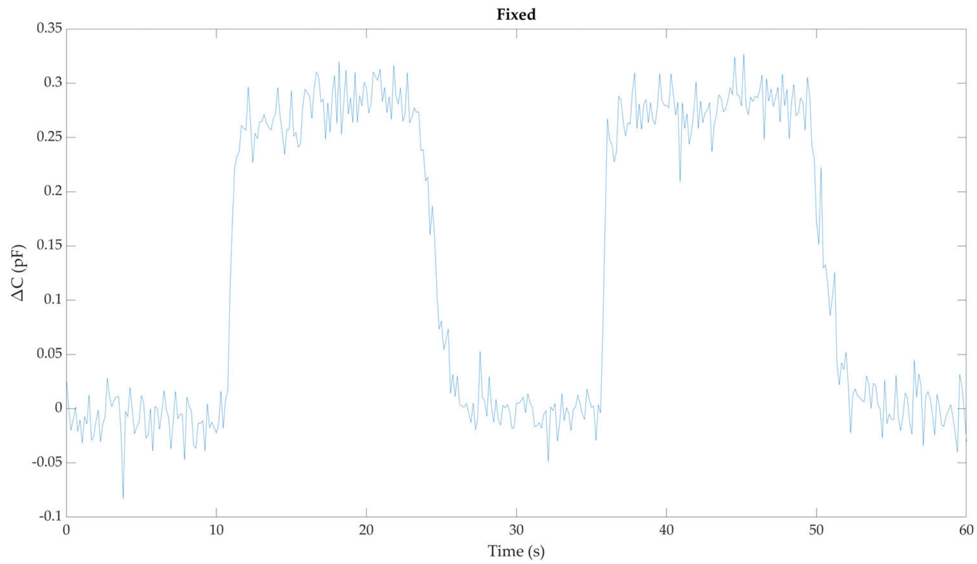

(a) Fixed spring result.

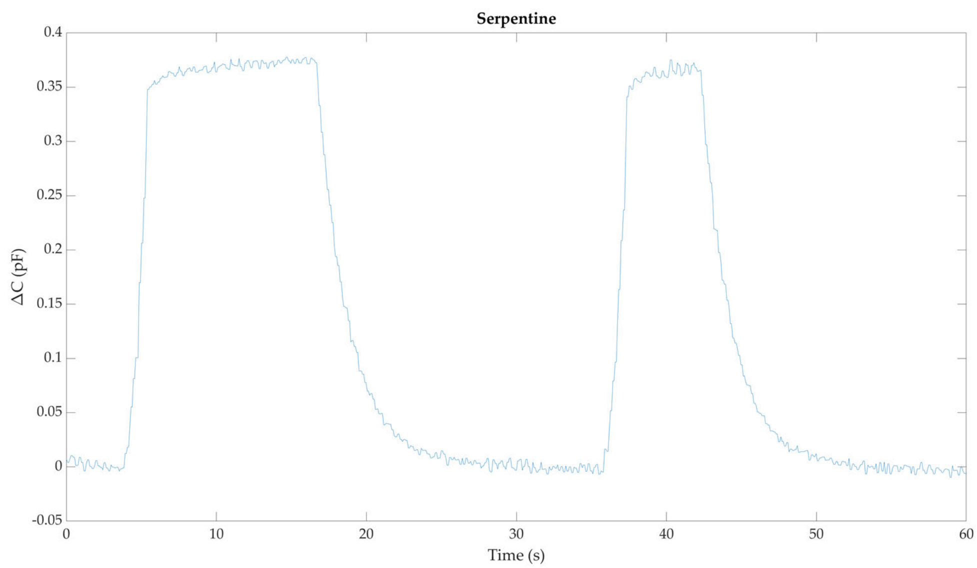

(b) Serpentine spring result.

Figure 3.25: Comparison of fixed vs. serpentine spring electrodes for toggling a 312 kV/m DC electric field.

3.5.3 | Serpentine Spring Test Results

To characterize the sensitivity and resolution of the printed MEMS device for comparison to the lithographic device in Fig. 3.4 (b), the metal plate was swept from 0-400 V in steps of 25 V. Each step was held for approximately 5 seconds, resulting in a sweep of electric field strength from 0-250 kV/m in steps of 15.6 kV/m. The received data, sampled at 45 Hz, was down-sampled to 5 Hz using a moving average to clean the signal. The resulting data over time is shown in Fig. 3.26, whereas the associated ΔC vs. E curve is shown in Fig. 3.27.

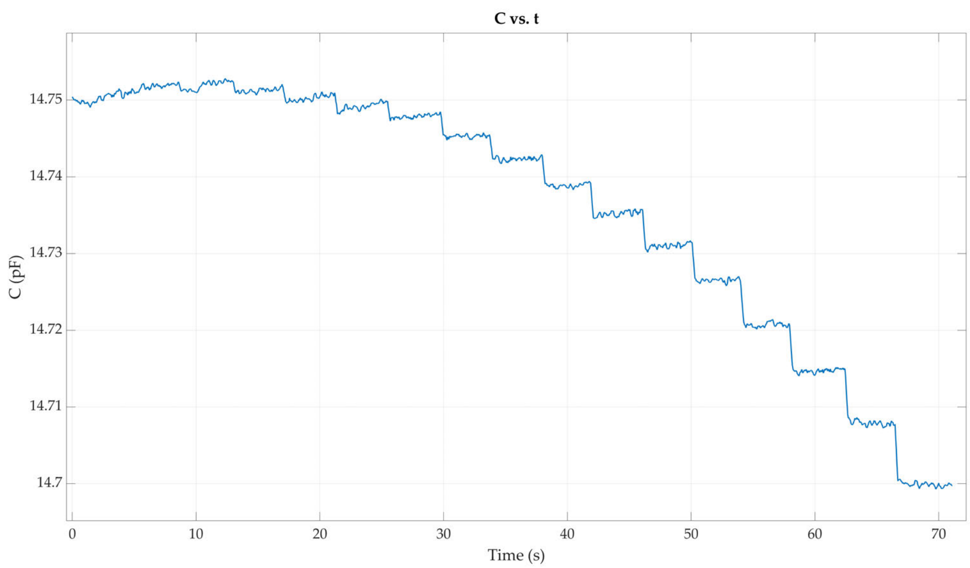

Figure 3.26: Capacitance vs. time for sweeping DC electric field.

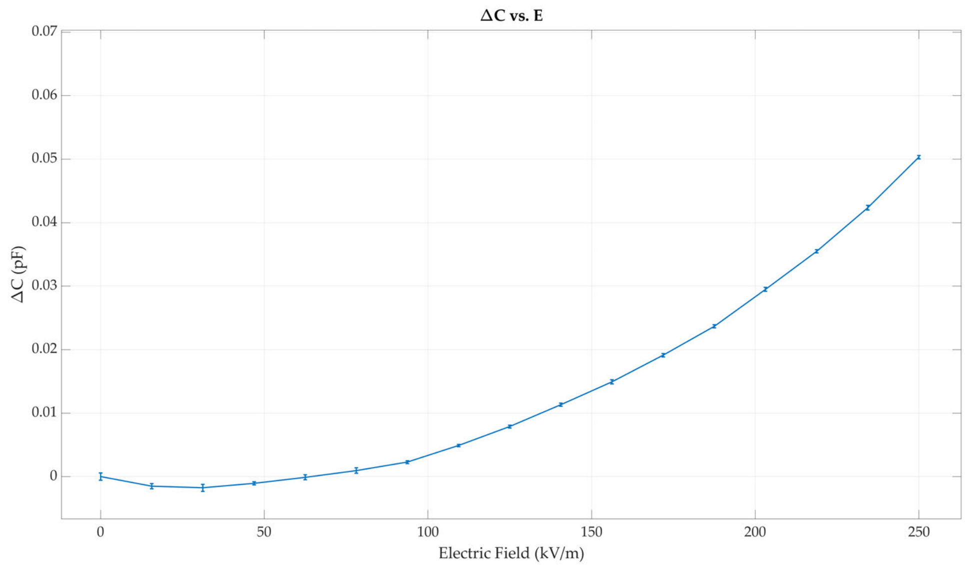

Figure 3.27: ΔC vs. electric field.

Based on the standard deviation of the noise at 156 kV/m, the noise-limited resolution of the sensor was 4.7 kV/m, and 11.1 kV/m without signal averaging. This was defined as 3 standard deviations:

$$Resolution = 3\sigma_{noise}$$

The sensitivity in the linear region of Fig. 3.27 (100-250 kV/m) was 2.67 $\times 10^{-4}$ pF/kVm^{-1}, based on the slope between adjacent data points in the near-midpoint of this region, around 171 kV/m.

The lithographic MEMS device [42] of Fig. 3.6 had a resolution of 16.2 kV/m and a sensitivity of 6.17 $\times 10^{-5}$ pF/kVm^{-1}. Therefore, the PE device had a better resolution with and without signal averaging, but a worse sensitivity. The superior resolution could be attributed to the large area of the sense electrode, but the large structure and correspondingly stiffer spring constant makes the device less sensitive to changes in the electric field. Other lithographic MEMS DC electric field sensors and their resolutions are shown in Table 3.4. Note that most of these devices achieve their impressive resolution through complex signal modulation and filtering process, whereas the PE sensor in this chapter gives a raw output. The key takeaway from this chapter is that PE is certainly promising for MEMS development, yielding similar, if not better, results than lithography.

Table 3.4: MEMS DC electric field sensors and their resolutions.

Work	**Resolution**
T. Chen et al. [42]	16.2 kV/m
B. Hill et al. [58]	4.6 V/m
S. Liyanage et al. [41]	3 V/m
G. Wijeweera et al. [59]	42 V/m
This work	4.7 kV/m

4

Lorentz Actuator

This chapter outlines the development of a printed electronics Lorentz actuator. The chapter begins with an introduction to Lorentz actuators and gives some examples from the current literature. Then, the theory and background behind their operation is given, along with some relevant design equations and the design of the lithographic device chosen for comparison. The design of the printed electronics device is developed and some ink parameters are determined, such as resistivity, adhesion, and coefficient of thermal expansion. A device that is 4.8× the scale of the lithographic counterpart is designed and simulated, as well as one that is 1.5×. The two devices are then fabricated, tested, and compared to each other and the lithographic device.

4.1 | Background

MEMS Lorentz actuators are devices that convert electrical energy into mechanical motion through the interaction of electric currents and a magnetic field [60]. They do so via the Lorentz force, the force felt by a current-carrying conductor in an external magnetic field, balanced by a spring restoring force. The actuator is usually a current-carrying conductor, such as a wire or a coil, supported by springs near a permanent magnet. The result is an actuator whose deflection depends linearly on the supply current. The Lorentz actuator has several advantages to other actuation methods. For example, thermal actuators utilise Joule heating to obtain a deflection, but consume a large amount of power. Electrostatic actuators burn little to no power, but rely on large supply voltages and have a non-linear response. Lorentz actuators, on the other hand, have relatively low supply voltages, linear and fast response, little to no hysteresis effects, and can have large strokes depending on design choices. Applications of MEMS Lorentz actuators include optical switches, variable optical attenuators, microscanners, adaptive optics, and more [60].

The design of Lorentz actuators are fairly simple, and it is generally desirable to maximize deflection for a given applied voltage. This can be achieved by refining the spring geometry and orientation of current flow with respect to the magnetic field direction. Examples of common spring geometries used are leaf springs [61], curved springs [62], serpentine springs [63], and folded beam or meandering springs [64, 65].

Some example Lorentz actuators from the literature are shown in Fig. 4.1. The authors in [63] realized a micro-actuator from a coil supported by serpentine springs to control a lens (Fig. 4.1 (a)). [62] designed and fabricated a dual-axis in-plane Lorentz actuator with curved beam support springs (Fig. 4.1 (b)). B. Park et al. [64] created a deformable mirror for wavefront control in adaptive optics from an array of Lorentz actuators. Each Lorentz actuator consists of a current-carrying crossbar and folded beam spring suspension [66] (Fig. 4.1 (c)).

The MEMS Lorentz actuator chosen for treatment of PE in this thesis is that of Fig. 4.1 (c) [66]. This is due to its relatively simple and 2D planar design which best suits PE. Also, its shape and design is easily scalable to meet the resolution of the Voltera NOVA electronics printer. In this chapter, emphasis will be placed on the design, fabrication, and testing of

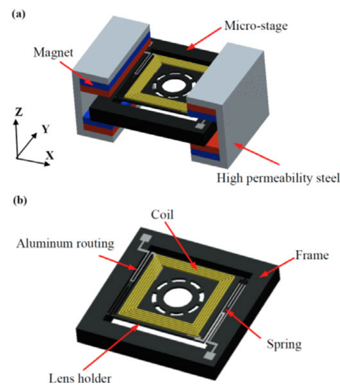

(a) Serpentine spring-suspeneded coil Lorentz actuator (©IEEE 2013).

S. . -J. Lin, C. . -C. Lee, W. . -L. Sung, F. . -Y. Lee and W. Fang, "Displacement enhancement of 1-axis Lorentz force actuator," 2013 Transducers & Eurosensors XXVII: The 17th International Conference on Solid-State Sensors, Actuators and Microsystems (TRANSDUCERS & EUROSENSORS XXVII), Barcelona, Spain, pp. 1591-1594, 2013.

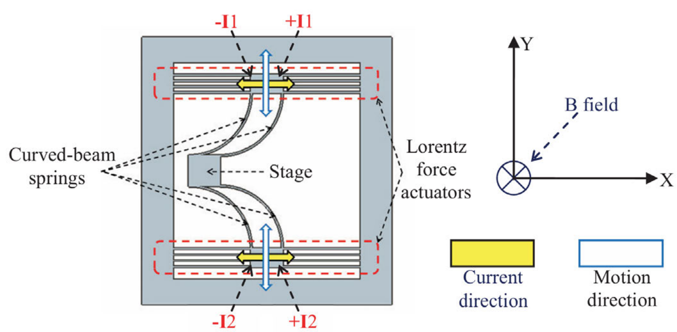

(b) Curved beam in-plane Lorentz actuator.

Reprinted from Procedia Engineering, Vol 25, Lee FY, Tang TL, Fang W, Development of a Novel Dual-axis Large-displacement Microstage Using Lorentz Force Actuators and Curved-beam Springs, pp. 689-692, Copyright 2011, with permission from Elsevier.

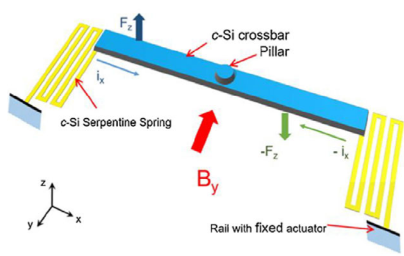

(c) Folded beam Lorentz actuator.

Reprinted from Sensors and Actuators A: Physical, Vol 280, B. Park, E. Afsharipour, D. Chrusch, C. Shafai, D. Andersen, G. Burley, A low voltage and large stroke Lorentz force continuous deformable polymer mirror for wavefront control, pp. 197-204, Copyright 2018, with permission from Elsevier.

Figure 4.1: MEMS Lorentz actuators.

a MEMS Lorentz actuator utilising PE, and the actual application of the actuator, be it for adaptive optics, optical switches, etc., is not within the scope of this thesis.

4.2 | Theory and Design

4.2.1 | Theory of Operation

The Lorentz actuator of Fig. 4.1 (c) operates via the Lorentz force:

$$\vec{F}_L = l\vec{i} \times \vec{B} \tag{4.1}$$

where l is the length of the crossbar (in blue), i is the current, and B is the magnetic flux density. The magnitude of the force depends on the length of the bar, the current, the magnetic flux density, and the angle between them θ:

$$F_L = ilB \sin\theta \tag{4.2}$$

If it assumed that i and B remain perpendicular to one another ($\theta = 90°$), then this simplifies to:

$$F_L = ilB \tag{4.3}$$

There also exists a spring restoring force given by Hooke's law (Eq. 3.2) which balances the Lorentz force at equilibrium:

$$k\Delta z = ilB \tag{4.4}$$

where Δz is the out-of-plane deflection of the crossbar and k is the combined spring constant of the folded beam springs. Eq. 4.4 can be re-arranged to solve for a deflection:

$$\Delta z = \frac{ilB}{k} \tag{4.5}$$

for specified i, l, B, and k values. Eq. 4.5 will guide the design of the scaled up PE Lorentz actuator. In particular, the spring constant is the most important consideration, and the next section will detail the analytical approach to determining the spring constant for a folded beam serpentine spring.

4.2.1.1 | Folded Beam Spring Constant

To derive the spring constant expression for a folded beam spring, we will first invoke Castigliano's second theorem, which states that the deflection of a beam δ is the partial derivative of strain energy stored in the beam U with respect to the applied force F [67]:

$$\delta = \frac{\partial U}{\partial F} \tag{4.6}$$

From beam theory, the torsional strain energy U_T and bending strain energy U_B sum together to give U [67]:

$$\begin{aligned} U &= U_B + U_T \\ U_B &= \int \frac{M^2}{2YI}\, dx \\ U_T &= \int \frac{T^2}{2GJ}\, dx \end{aligned} \tag{4.7}$$

where M is the bending moment, T is the torsional moment, Y is the Young's modulus, G is the shear modulus, I is moment of inertia, and J is the torsional constant. The integral is done over the length of the beam. There are two beam types at play in the spring design, the veritcal span beams that experience bending force, and the horizontal connecting beams that experience torsional force and bending force (Fig. 4.2). One segment consists of two horizontal and two veritcal beams, and a complete spring may have N segments. The total strain energy in an entire spring is then:

$$U = N(2U_{B,vert} + 2U_{B,horiz} + 2U_{T,horiz}) \tag{4.8}$$

For a beam of length L, the bending moment M and torsional moment T are [67]:

$$\begin{aligned} M(x) &= Fx \qquad x \in [0, L] \\ T &= FL \end{aligned} \tag{4.9}$$

Substituting these into the equations for U_B and U_T gives:

$$\begin{aligned} U_{B,vert} &= \int_0^{L_V} \frac{(Fx)^2}{2YI}\,dx = \frac{F^2 L_V^3}{6YI} \\ U_{B,horiz} &= \frac{F^2 L_H^3}{6YI} \\ U_{T,horiz} &= \int_0^{L_H} \frac{(FL_V)^2}{2GJ}\,dx = \frac{F^2 L_V^2 L_H}{2GJ} \end{aligned} \tag{4.10}$$

where L_H and L_V are defined according to Fig. 4.2. Substituting these into Eq. 4.8 yields:

$$U = \frac{NF^2}{3YI}\left(L_V^3 + L_H^3\right) + \frac{NF^2 L_V^2 L_H}{GJ} \tag{4.11}$$

We can then differentiate this with respect to force F to find the deflection δ (Eq. 4.6):

$$\begin{aligned} \delta &= \frac{\partial U}{\partial F} \\ &= \frac{2NF}{3YI}\left(L_V^3 + L_H^3\right) + \frac{2NFL_V^2 L_H}{GJ} \end{aligned} \tag{4.12}$$

From Hooke's law, we know that spring constant k is force divided by deflection:

$$
\begin{aligned}
k &= \frac{F}{\delta} \\
&= \frac{1}{N}\left(\frac{2}{3YI}\left(L_V^3 + L_H^3\right) + \frac{2L_V^2 L_H}{GJ}\right)^{-1}
\end{aligned}
\tag{4.13}
$$

Eq. 4.13 can then be used to find the spring constant of a folded beam, given properties such as the moment of inertia I, torsional constant J, Young's modulus Y, shear modulus G, and lengths L_H and L_V, as well as a specified number of spring segments N. From [66, 67], the formulae for shear modulus, torsional constant, and moment of inertia for a beam are:

$$
\begin{aligned}
G &= \frac{Y}{2(1+\nu)} \\
I &= \frac{wt^3}{12} \\
J &= \frac{wt^3}{3}\left(1 - \frac{192}{\pi^5}\frac{t}{w}\sum_{n=1,3,5,\ldots}^{\infty}\left(\frac{1}{n^5}\tanh\left(\frac{n\pi w}{2t}\right)\right)\right)
\end{aligned}
\tag{4.14}
$$

where thickness t and width w are defined in Fig. 4.2, and ν is Poisson's ratio.

A MATLAB script was written to compute k for varying values of t, w, L_V, L_H, N, and material properties Y and ν. The summation within J was taken to 101 rather than ∞.

4.2.2 | Lithographic MEMS Design

The design of Fig. 4.1 (c) [66] has the features outlined in Table 4.1 and defined in Fig. 4.3. The figure shows both a zoomed-in section of the spring and the full device, with labels for +/- voltage supply, current, magnetic flux density, and Lorentz force (the $\odot$ symbol means 'vector out-of-page'). The lithographic design uses single-crystal silicon for the structure and a Ti/Al/Ti coating for the conductor; this will be discussed more in the Fabrication section of this chapter.

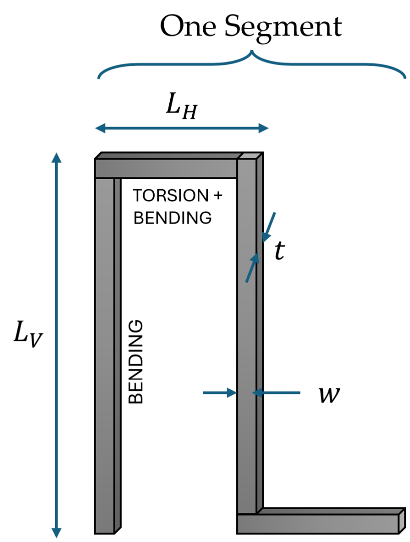

Figure 4.2: One segment of a folded beam spring.

Table 4.1: Design parameters of lithographic MEMS Lorentz actuator.

L_V	700 μm
L_H	50 μm
t	5.5 μm
w	29 μm
N	2
L_C	2.08 mm
w_C	200 μm
t_c	25 μm

4.2.3 | Printed Electronics Design

The design for the PE Lorentz actuator took heavy inspiration from the lithographic MEMS device of [66]. However, the device had to be scaled up to meet the resolution requirements for the Voltera NOVA printer (>150 μm). This involved setting the smallest parameter of Fig. 4.3 to 150 μm, and then scaling everything somewhat proportionally from there. This

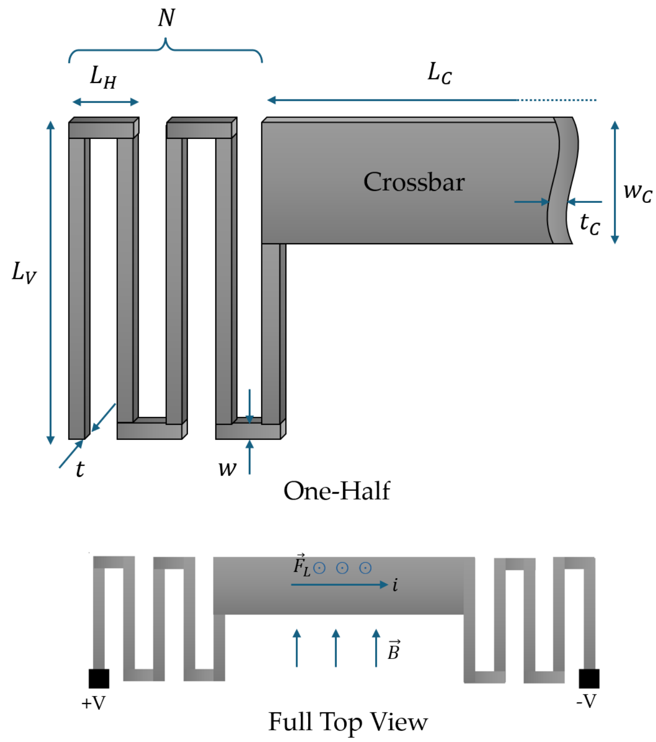

Figure 4.3: Lithographic MEMS Lorentz actuator design.

was w, the width of the springs, so w = 150 μm. From Table 4.1, the scale factors were L_C = 71.7w, L_H = 24.1w, L_V = 1.7w, w_C = 6.9w, and t = 0.16w, which resulted in L_C = 1.0 cm, L_H = 255 μm, L_V = 3.6 mm, w_C = 1.0 mm, and t = 24 μm. It was then decided that the device could be printed on 25 μm PI, with $t = t_C$, so as to closely mimic the scaled thickness as possible. The silver ink, too, would add thickness as well, but 25 μm was the thinnest available PI. In the end, the overall scale factor was 4.80×. From Eq. 4.13, this gave a theoretical spring constant of 0.045 N/m for each spring considering that the thickness was due to PI and the ink (approximately 40 μm), and $N = 2$. Since the two springs on either side are in parallel, their spring constants add, yielding a total spring constant of 0.09 N/m. The lithographic device had a spring constant of 0.14 N/m by similar analysis.

Next, the task was to couple the mechanical and electromagnetic behavior of the device, using Eq. 4.5. From [66] (case C), the author used a 0.48 T field for testing and obtained a maximum deflection of 50 μm at 15 mA of current. Therefore, with k = 0.09 N/m, B = 0.48 T, l = L_C = 1.0 cm, and Δz = 50 μm, the required current was i = 1 mA for the PE device. To obtain this current, the resistance of the ink pattern had to be known. Therefore, an experiment was carried out to determine the resistivity of Voltera Conductor 3 silver ink, as well as how it varies with curing time.

4.2.3.1 | Resistivity of Ink

For the Lorentz actuator, in order to determine how much applied voltage was necessary for a specified current, the resistance of the conduction path (springs, crossbar, etc.) was required. Thus, the resistivity ρ of Voltera Conductor 3 ink had to be characterized. Furthermore, the dependence of resistivity of the ink as a function of cure time was explored.

Four ink squares, measuring 1.5 $\times$ 1.5 cm, were printed on 125 μm thick, un-treated PI with the same printing parameters as previous section. First, the thickness t of each square was determined using a KLA P7 Profiler. Then, a Veeco FPP5000 [68] four point probe was used to find the resistance R of each sample using the V/I function, related to the resistivity by:

$$\rho = 4.532Rt$$

where the 4.532 coefficient is a correction factor characteristic of the FPP5000. The four point probe differs from a normal resistance measurement in the fact that it eliminates the effect of contact resistance (Fig. 4.4). In a conventional ohmmeter, two probes both supply current to the sample and measure the voltage simultaneously, thus yielding the resistance of the sample via Ohm's law:

$$R = \frac{V}{i}$$

However, the measured voltage is the combined voltages across the contact resistances and the resistance of the sample. In a four point probe, the current supply and voltmeter are separate. The voltmeter only measures the voltage drop across the sample and not the sample in series with the contact resistances. This method yields a more accurate resistance reading than a conventional ohmmeter.

The results obtained from the four-point probe are collected in Table 4.2. For reference, the Voltera Conductor 3 datasheet specifies 1.27 $\times 10^{-7}$ $\Omega\cdot$m [26]. Fig. 4.5 shows a plot of resistivity of the ink vs. cure time. As the ink spends more time in the oven, more and more solvents evaporate and the ink NPs sinter further, reducing resistivity.

Table 4.2: Four point probe measurements for Voltera Conductor 3.

Cure Time (min.)	**Thickness (μm)**	**Resistance (10^{-3} Ω)**	**Resistivity (10^{-7} $\Omega\cdot$m)**
15	15.5	2.14	1.50
20	12.6	1.88	1.07
25	13.6	1.60	0.98
30	13.3	1.52	0.91

Clearly, curing for a longer time results in better resistivity (lower voltage for same current, thus lower power consumption). However, curing for extended periods of time was thought to have adverse affects on adhesion of the ink to the PI substrate. Therefore, an experiment was carried out to look at how cure time affects adhesion, with and without surface preparation, and how surface preparation affects printed line width and height.

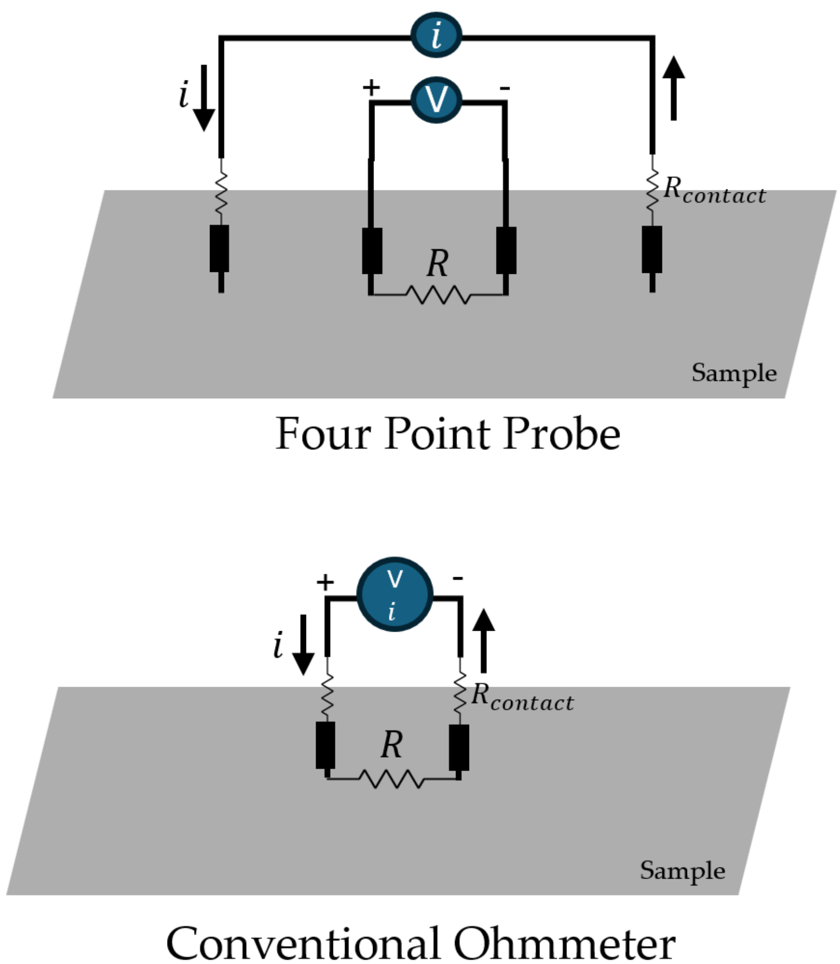

Figure 4.4: Four point probe vs. conventional ohmmeter.

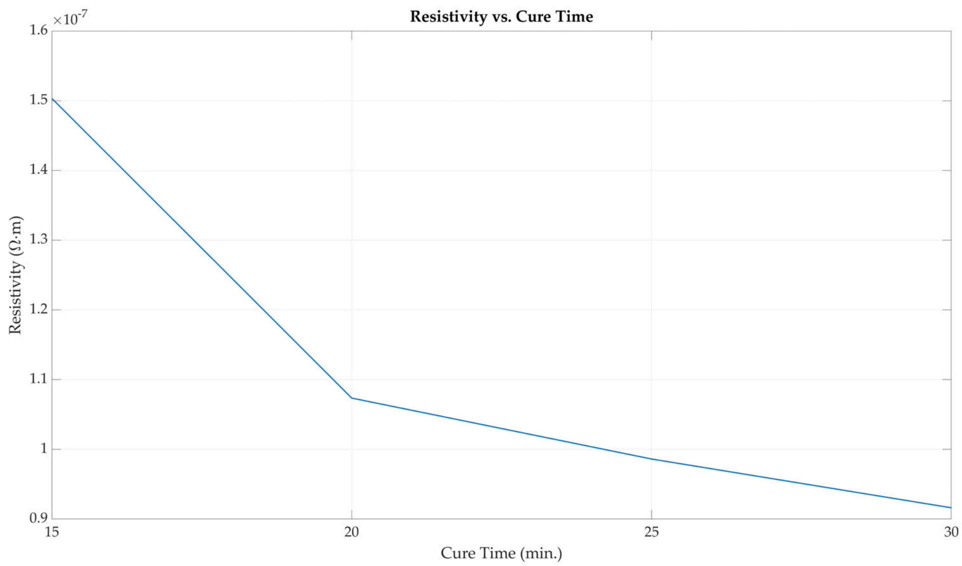

Figure 4.5: Resistivity of Voltera Conductor 3 vs. cure time.

4.2.3.2 | Polyimide Surface Adhesion and Preparation

From the previous chapter, it was evident that on small springs made of ink and PI, the ink can delaminate from the PI and cause open circuits. To mitigate this, it was thought that roughening the surface by some means would help increase the surface energy of the substrate and thus enhance adhesion. For example, the authors in [69] used UV plasma to etch PI to increase adhesion of thin copper films. An easier and more cost-effective method, as mentioned by [70], is to roughen the surface with sandpaper. Although not as controlled as plasma etching or sandblasting, it can greatly increase surface energy and promote adhesion, similar to results obtained by plasma etching. Of course, it depends on the grit of the sandpaper; according to the literature, it seemed that 800-1200 grit sandpaper was the most commonly used [71, 72].

First, an experiment was carried out to investigate ink-PI adhesion with respect to surface pre-treatment and cure time. A piece of 125 μm thick PI had half of its area roughened with 800 grit sandpaper. 7×7 mm squares were printed on both un-treated and pre-treated PI, and cured for 15, 20, 25, and 30 minutes at 120 °C. Dispense pressure was 800 and print height was 60 μm, with a 225 μm nozzle. Fig. 4.6 shows the print outline.

The test for adhesion utilised ASTM D3559 method B [73]. This involved cutting each sqaure into an evenly spaced 6×6 cross-hatch pattern, placing 3M Scotch tape firmly over top, then quickly and consistently peeling the tape back over itself. Then, under a Leica DM6-M microscope, the remaining cross-hatch pattern is analysed and adhesion is graded according to Fig. 4.7. The results are collected in Table 4.3.

From the adhesion grading results, it was clear that 20 minutes was the best cure time for adhesion, as it progressively got worse in either direction. Also, un-treated PI performed better than treated in the grading. However, where un-treated PI failed in the cross-

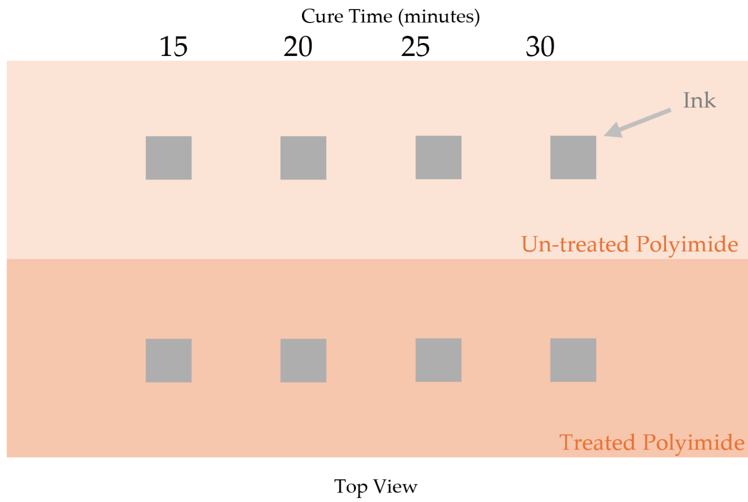

Figure 4.6: Print outline for surface preparation experiment.

Table 4.3: ASTM D3359-B cross-hatch adhesion test results for Voltera Conductor 3 on polyimide.

Cure Time	Un-treated	Treated
15 min.	3B	3B
20 min.	5B	4B
25 min.	4B	2B
30 min.	2B	3B

hatch test, almost whole squares were removed cleanly, whereas with treated PI only edges of squares flaked off. So, there is a tradeoff between the two; treated PI's edges may flake but it still may uphold the integrity of the circuit, whereas with un-treated PI, if delamination occurs, it may result in an open circuit. In short, it depends on the application; if a large expanse of ink is to be printed, such as an electrode, then un-treated may be favored, whereas for narrow interconnects and traces, treated may be preferred.

Next, the effect of surface preparation on printed ink line profile, height, and width was examined. Again, a 125 μm thick piece of PI had half of its area roughened with 800 grit

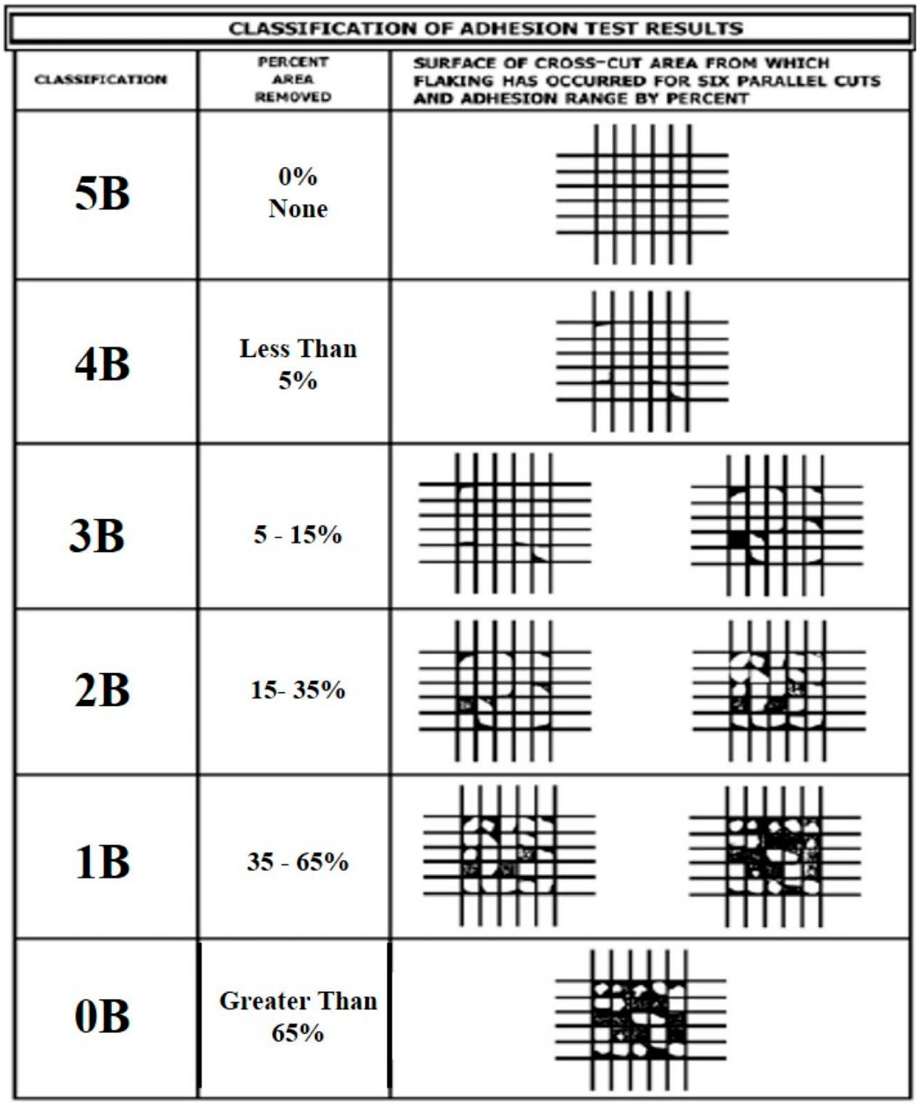

CLASSIFICATION OF ADHESION TEST RESULTS		
CLASSIFICATION	PERCENT AREA REMOVED	SURFACE OF CROSS-CUT AREA FROM WHICH FLAKING HAS OCCURRED FOR SIX PARALLEL CUTS AND ADHESION RANGE BY PERCENT
5B	0% None	
4B	Less Than 5%	
3B	5 - 15%	
2B	15- 35%	
1B	35 - 65%	
0B	Greater Than 65%	

Figure 4.7: ASTM D3359-B standard for adhesion tape testing. Reproduced from [74] under the terms of the Creative Commons Attribution (CC BY) License.

sandpaper. Then, two 2 cm lines were printed; one on the pre-treated PI, and one on the un-treated. Dispense pressure was 800 and print height was 60 μm, with a 225 μm nozzle. Then, the two traces were cured at 120 °C and examined on a KLA P7 profiler. A 2000 $\times$

90 μm 3D scan was conducted, with results shown in Fig. 4.8. Also, the two traces were examined on a Leica DM6-M microscope (5x objective lens) and images captured, shown in Fig. 4.9.

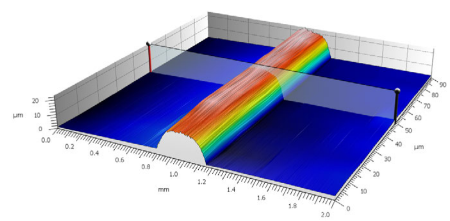

(a) Un-treated 3D scan.

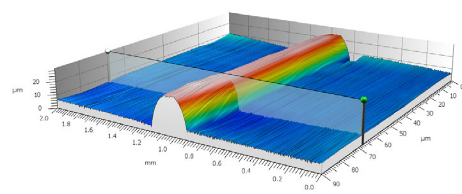

(b) Pre-treated 3D scan.

Figure 4.8: Pre-treated vs. un-treated 3D scans.

It was seen that pre-treating results in a narrower and higher line, whereas un-treated is wider and lower. Printed line height was increased by 16% for pre-treated compared to un-treated (from 21.2 to 24.6 μm), and printed line width was reduced by 20% (from 360 to 287 μm). This was because, with a lower surface energy, the un-treated PI allowed the ink to spread out more across its surface, whereas the rougher pre-treated PI resisted ink spreading.

From the previous two experiments, it was clear that a tradeoff exists between cure time, resistivity, and adhesion (Fig. 4.10). So, a 20 minute cure time at 120 °C is best moving forward to achieve good adhesion, with or without surface preparation, and acceptable resistivity. Continuing on, the resistance R of the PE Lorentz actuator can be found by summing the individual series resistances of the folded beam springs and the crossbar using:

$$R = \rho \sum_i \frac{l_i}{w_i t} \tag{4.15}$$

where l_i and w_i are the lengths and widths of the i-th resistive segment, t is thickness, and ρ is the resistivity (1.07 $\times 10^{-7}$ $\Omega \cdot m$ for 20 minute cure time). This gives a total resistance of 1.57 Ω. For 1 mA of current, this requires an applied voltage of 1.57 mV by Ohm's law, consuming roughly 2.5 μW of power at maximum stroke.

A consequence of running current through the actuator is Joule heating. This makes the device behave doubly as a thermal actuator as well as a Lorentz actuator, since their respective deflections Δz_J and Δz_L both depend on the current. Ideally, $\Delta z_J << \Delta z_L$, since Δz_J is non-linear with respect to current. To see how Δz_J changes with actuation current, a COMSOL simulation was carried out. But first, the coefficient of thermal expansion of the ink had to be known for the simulation to be accurate, so an experiment was done to determine it, similar to how Young's modulus was found in the previous chapter. Then, in the Simulation section, the effect of Joule heating on the Lorentz actuator will be explored, as well as the device's overall performance.

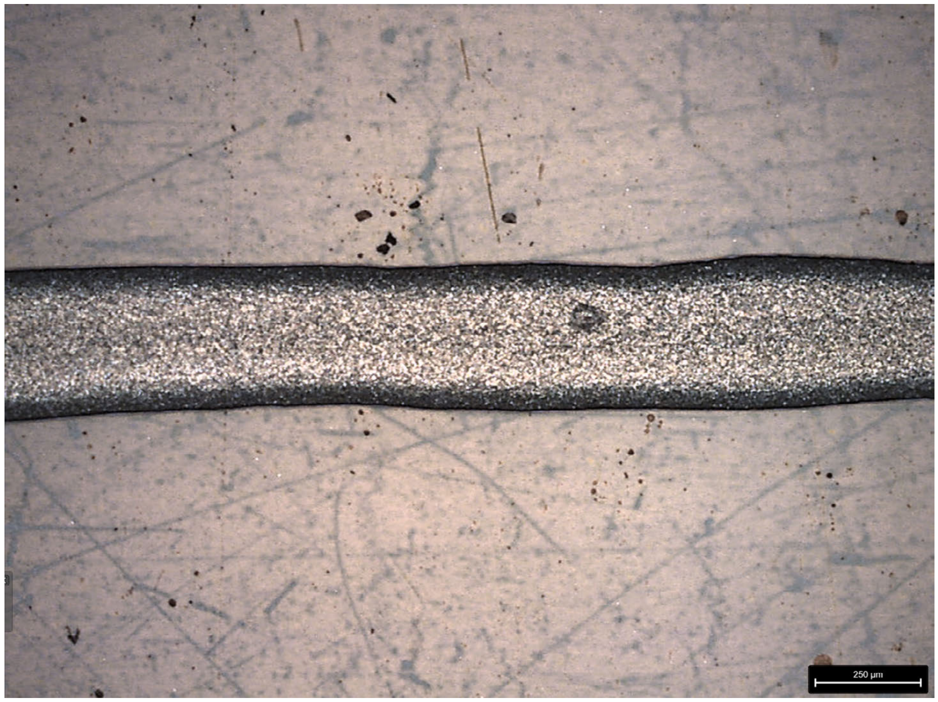

(a) Un-treated microscope image.

(b) Pre-treated microscope image.

Figure 4.9: Pre-treated vs. un-treated microscope images.

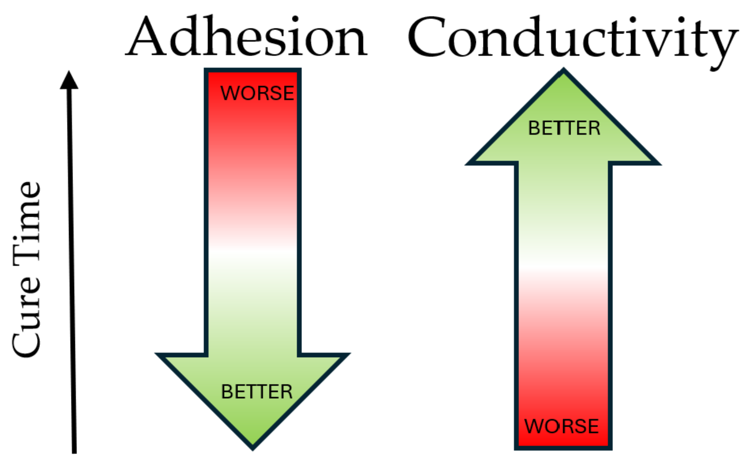

Figure 4.10: Adhesion vs. conductivity tradeoff.

4.2.3.3 | Coefficient of Thermal Expansion

Coefficient of thermal expansion was determined by utilising a digital twin in COMSOL software to narrow in on the value based on real-world experiment. A simple U-shaped bi-morph thermal actuator [74] was printed on 125 μm PET flexible substrate with same print settings as Table 3.3. Using the KLA P7 profiler, ink thickness was found to be 13.6 μm. The trace had a resistance of 0.9 Ω as measured by an Agilent 34401A muiltimeter [75]. The actuator was then released using the Oxford laser cutter. Applying a voltage of 0.7 V yielded a current of 710 mA, which caused the actuator to deflect by 120 μm as measured by the Leica microscope. The same device was modeled in COMSOL using the Solid Mechanics, Heat Transfer in Solids, and Electric Currents modules, in addition to multiphysics couplings Electromagnetic Heating and Thermal Expansion. The two ends were fixed and had a terminal applied at each one; a current terminal with 710 mA on the left and a ground (0 V) voltage terminal on the right. A Temperature boundary condition was placed on the bottom PET layer, set to 293.15 K. The coefficient of thermal expansion of the ink was then swept until the model also deflected 120 μm, at which point a value of 40 $\times 10^{-6}$ 1/K was found. This assumed a fixed coefficient of thermal expansion for PET of 59.4 $\times 10^{-6}$ 1/K [76], as well as the same thermal conductivity as silver (429 W/m·K) for the ink. Fig. 4.11 shows a schematic of the bi-morph thermal actuator, the printed and laser-cut device, and the COMSOL model.

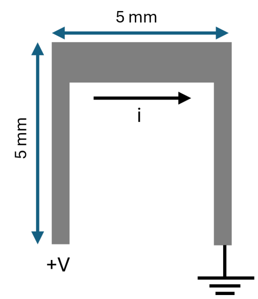

(a) Bi-morph thermal actuator.

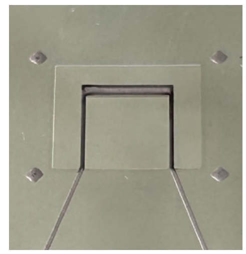

(b) Printed/released thermal actuator.

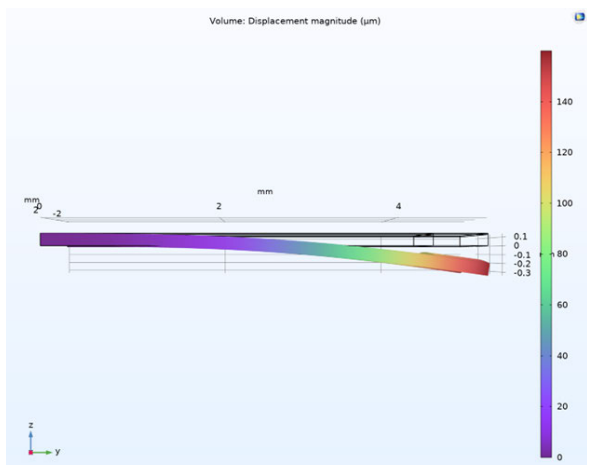

(c) Thermal actuator COMSOL model (side view).

Figure 4.11: Bi-Morph thermal actuator for finding coefficient of thermal expansion.

4.2.4 | Scaled Down Device Design

For the applications that use Lorentz actuators, size is a big factor. At 4.8× the size of the lithographic design, the proposed dimensions of the PE device can make it unwieldy. At an attempt to scale the PE device down to around the same size as the lithographic actuator in [66], it was thought that instead of explicitly printing the springs and crossbar, they could be cut out of a printed ink plane. In both cases, a laser mill is required to release the actuator, so there would be little to no change in the fabrication workflow.

However, scaling the device down, while keeping the thickness of the ink and substrate constant, would have an adverse affect on spring constant and device performance. Therefore, a simulation was carried out in COMSOL using the Solid Mechanics module to examine the effect of spring constant vs. scale. The scale factor was swept, starting from the lithographic dimensions and ending at the proposed PE dimensions; 1 to 4.8. The scaling was performed isotropically in the planar x-y dimensions, but the thickness was held constant at $t_{ink} + t_{PI}$. Along the way, the Lorentz force was applied to the device and the deflection measured to yield the spring constant for a given scale factor, with 30 mA current and a 0.48 T field. Note that the force is related to the scale factor since it depends on the length of the crossbar, L_C. Fig. 4.12 shows the plot of spring constant vs. scale factor. From this, a scale factor of 1.5 was chosen for the scaled down PE device, showing an increase in stiffness of about 10× from the scaled-up version, but being around 70% smaller in size. Table 4.4 shows the design parameters of the scaled down device, as well as the 4.8× scale device.

Table 4.4: Design parameters of PE MEMS Lorentz actuators.

Parameter	**4.8×**	**1.5×**
L_V	3.3 mm	1.1 mm
L_H	645 μm	200 μm
t	40 μm	40 μm
w	150 μm	75 μm
N	2	2
L_C	9.9 mm	3.12 mm
w_C	1 mm	315 μm
t_c	40 μm	40 μm

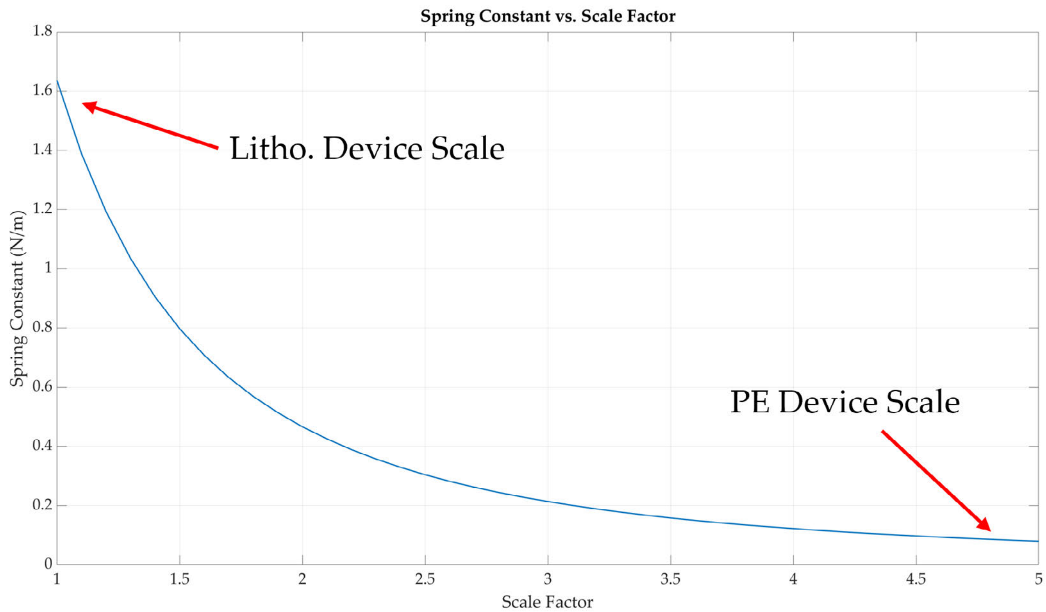

Figure 4.12: Spring constant vs. scale factor of device, thickness held constant.

4.3 | Simulation

This section highlights the simulations carried out in COMSOL software for the PE Lorentz actuator. First, the design in Fig. 4.13 was made in KiCad software. The resulting gerber file was converted to DXF format, which was then imported as a geometry into COMSOL. The 2D geometry was extruded to $t_{ink} + t_{PI}$ = 40 μm, where t_{ink} = 15μm and t_{PI} = 25 μm. Then, the 3D device was sliced in the x-y plane at z = t_{PI} to split the device into two layers: substrate and ink. Next, the top ink surface was split into crossbar and spring boundaries. Then, materials were assigned to each layer. Fig. 4.14 shows the device in COMSOL.

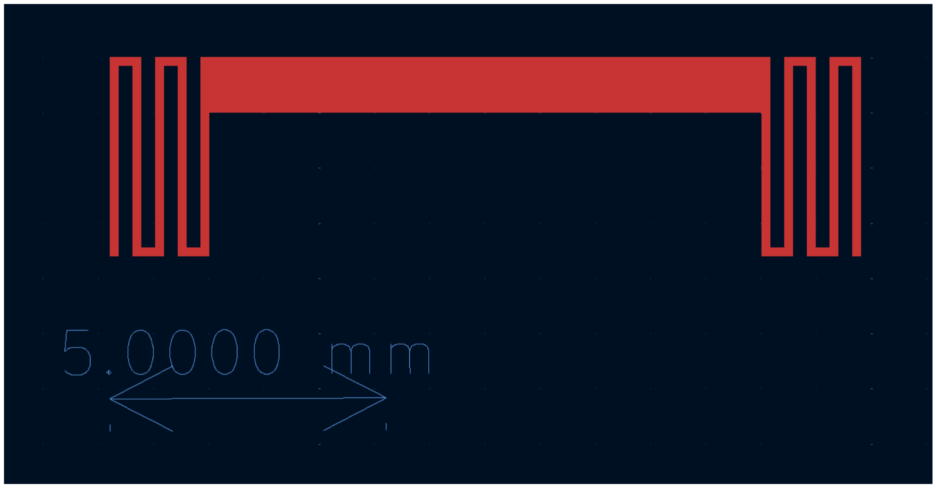

Figure 4.13: PE Lorentz actuator in KiCad.

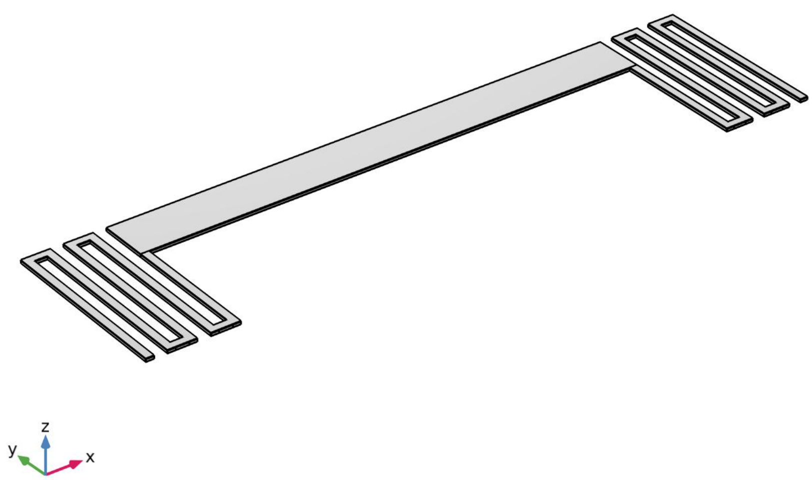

Figure 4.14: PE Lorentz actuator component in COMSOL.

4.3.1 | Lorentz Force

The first simulation that was carried out was to look at how the deflection of the PE Lorentz actuator varies with actuation current. For this, only the Solid Mechanics module was used in COMSOL software. The ends of the springs were given a Fixed Constraint, and the top surface of the crossbar was given a Boundary Load condition with a total force of $\vec{F} = iL_C B\hat{k}$. A normal-sized physics-controlled mesh was constructed, and then a Parametric Sweep study was applied and computed, sweeping the current i from 1 to 30 mA in steps of 0.2 mA. The field B was set to 0.48 T.

Fig. 4.15 shows the deflected device at 2.6 mA of current, where a 50 μm deflection occurs, which is off from the theorized 1 mA of actuation current. This could be due to the fact that Eq. 4.13 does not take into account the dynamics of the crossbar, which would increase the spring constant. Fig. 4.16 shows the response of maximum deflection vs. actuation current, which is perfectly linear with a sensitivity of 19.7 μm/mA.

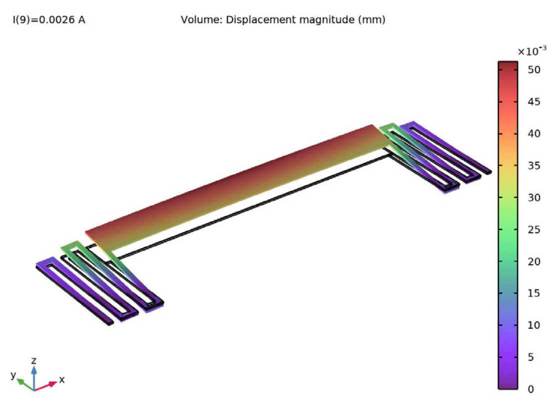

Figure 4.15: Simulated Lorentz force in COMSOL.

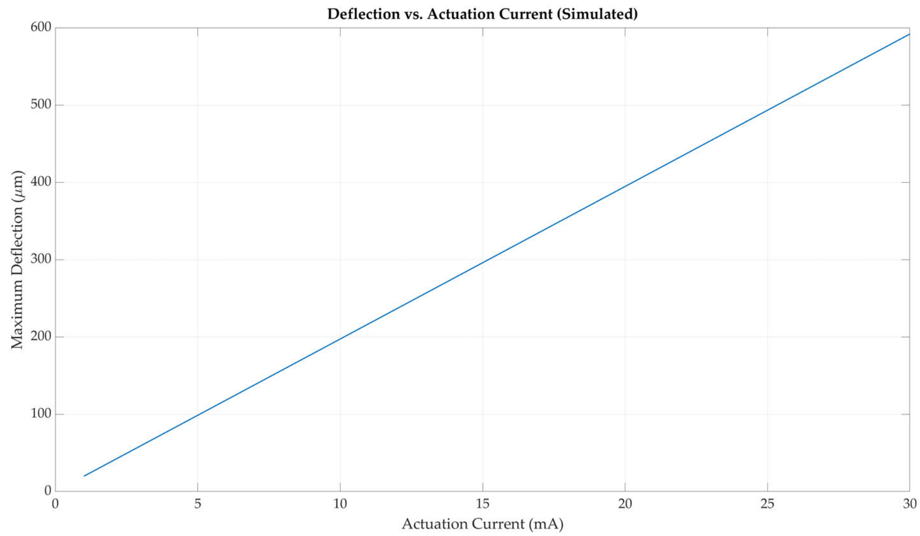

Figure 4.16: Simulated deflection due to Lorentz force in COMSOL.

4.3.2 | Joule Heating

The next simulation to be done was to see if the effect of Joule heating due to conduction could be neglected or not. The same model of Fig. 4.14 was used, with similar modules used as for finding coefficient of thermal expansion before. The current was then swept from 1 mA to 30 mA in steps of 5 mA (step size was increased from the Lorentz force simulation since the Joule heating simulation is significantly more computationally intensive). Fig. 4.17 shows plots for deflection due to Joule heating and temperature change. For currents in the range 0-30 mA, it appeared that deflections for Joule heating were roughly 0.013% that of the Lorentz force. Also, the temperature variation at 30 mA was only 0.03 K more than at 0 mA; therefore, the effect of Joule heating was neglected moving forward.

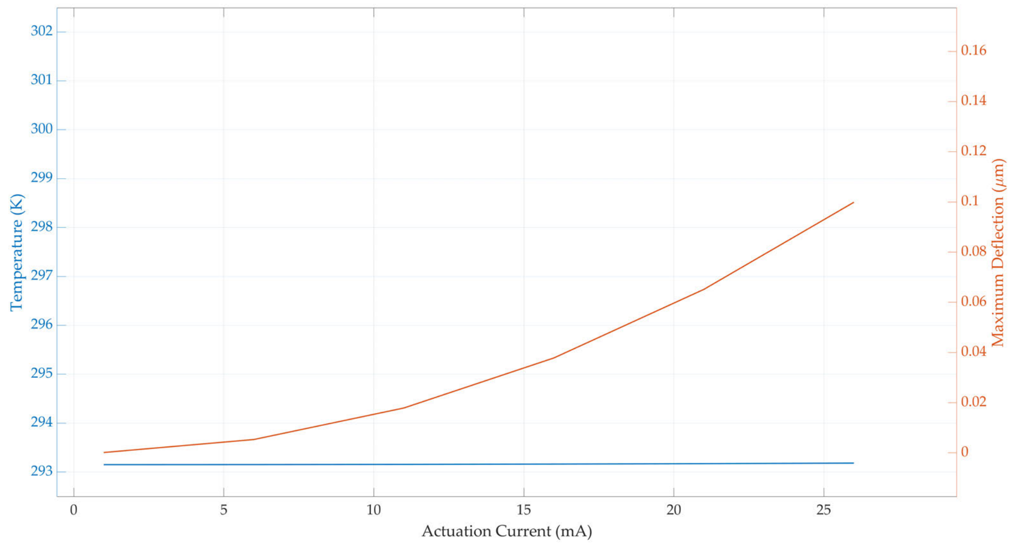

Figure 4.17: Joule heating effects for the PE Lorentz actuator.

4.3.3 | Scaled Down Device

The scaled down device (1.5× the lithographic dimensions, thickness same for PE) was simulated with the Lorentz force in an identical manner in COMSOL to the scaled-up PE device, sweeping the current from 0 to 30 mA. Fig. 4.18 (a) shows the deflection vs. actuation current curve for the scaled down device, which is again linear in its response with a sensitivity of 1.8 μm/mA. However, looking at Fig. 4.18 (b), it is clear that the scaled down device requires about 10× the amount of current to achieve the same deflection as the scaled-up actuator. Also, using the Electric Currents module in COMSOL, the resistance of the scaled down actuator was found to be 1.95 Ω. For a 50 μm stroke, 28 mA of current is required, resulting in 1.5 mW of power consumption; roughly 600× that of the scaled up device.

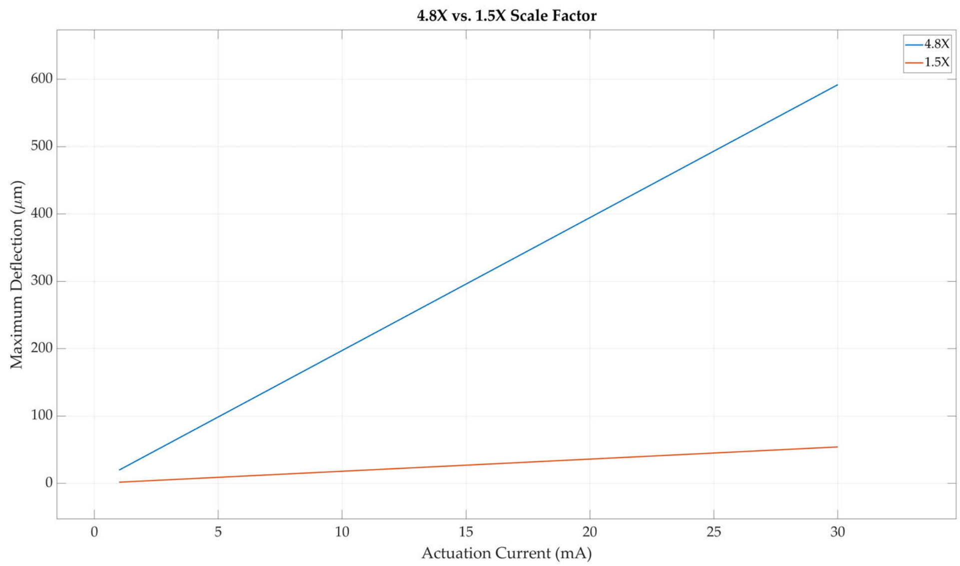

Figure 4.18: Scaled down device deflection vs. actuation current.

Since this device burned much more power than the scaled up version, the effect of Joule heating was explored briefly in COMSOL, similar to the previous section. Fig. 4.19 shows the results. Joule heating did not significantly influence the deflection, with a magnitude 2% that of the Lorentz-induced deflection. Also, temperature increased only 0.5 K over the range of actuation current. These results indicate that Joule heating may not be detrimental to the intended operation of the device, but the effect may be noticeable in real-world experiments.

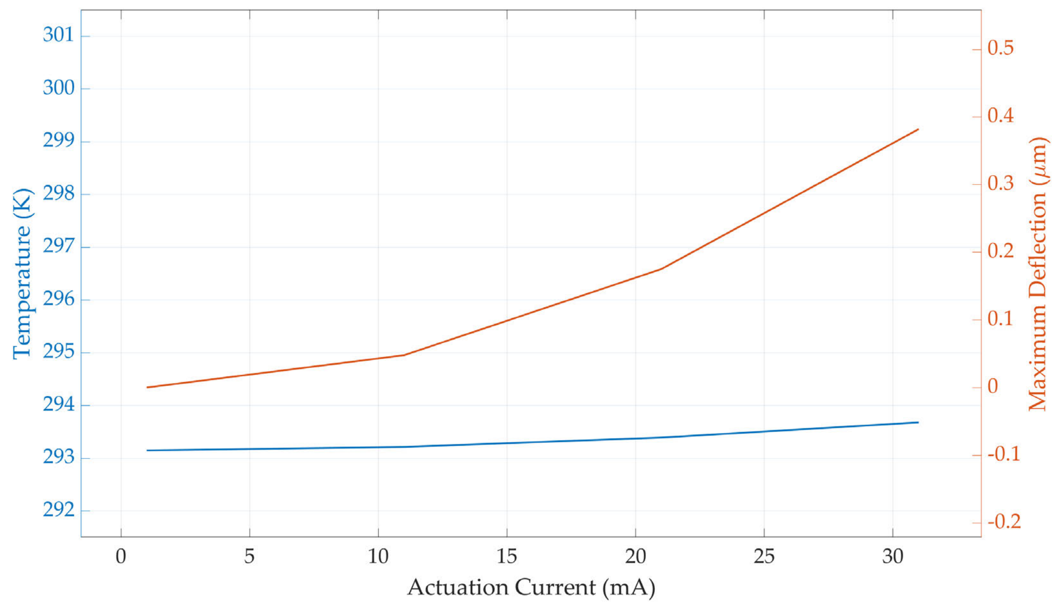

Figure 4.19: Effects of Joule heating on scaled down device.

4.4 | Fabrication

4.4.1 | Scaled Up Actuator

The method of fabrication for the scaled up PE Lorentz actuator was similar in execution and workflow as for the DC electric field sensor in the previous chapter. 25 μm PI was pre-treated with 800 grit sandpaper to improve adhesion. It was found that only sanding one side caused the PI to roll up due to uneven stress caused by asymmetrically removing material, so both sides were pre-treated to eliminate this effect. The design of Fig. 4.20 was printed with a 150 μm nozzle, 600 dispense pressure, 650 mm/min print speed, and 60 μm print height.

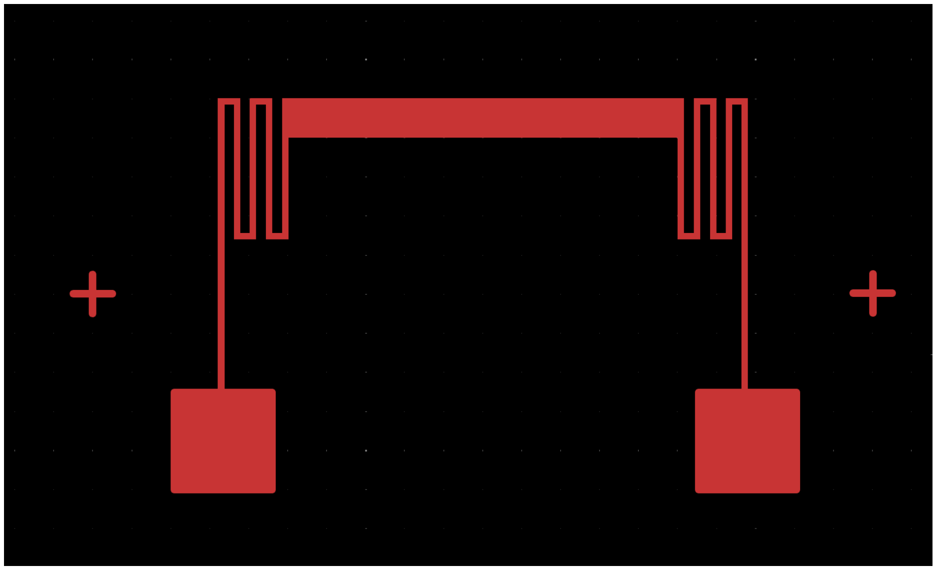

Figure 4.20: Scaled up Lorentz actuator design in KiCad.

The print was cured at 120 °C for 20 minutes. Then, the device was released via the Oxford laser cutter. Initially, the laser cut path followed the edges of the ink traces. However, in the corners of the spring bends, the ink spread unevenly (Fig. 4.21), almost causing an open circuit. Therefore, the cut path was relieved from the spring corners by a line width (200 μm) to compensate for this.

4.4.2 | Scaled Down Actuator

The scaled down Lorentz actuator was printed with identical substrate, print settings, and curing as previous section. The design of Fig. 4.22 (a) was printed, and the cut paths in Fig. 4.22 (b) were cut with the Oxford laser cutter; same cutting parameters as previous chapter.

Fig. 4.23 (a) shows both actuators, side-by-side, after printing and curing. Fig. 4.23 (b) and (c) show the scaled up and scaled down devices post laser cutting, respectively.

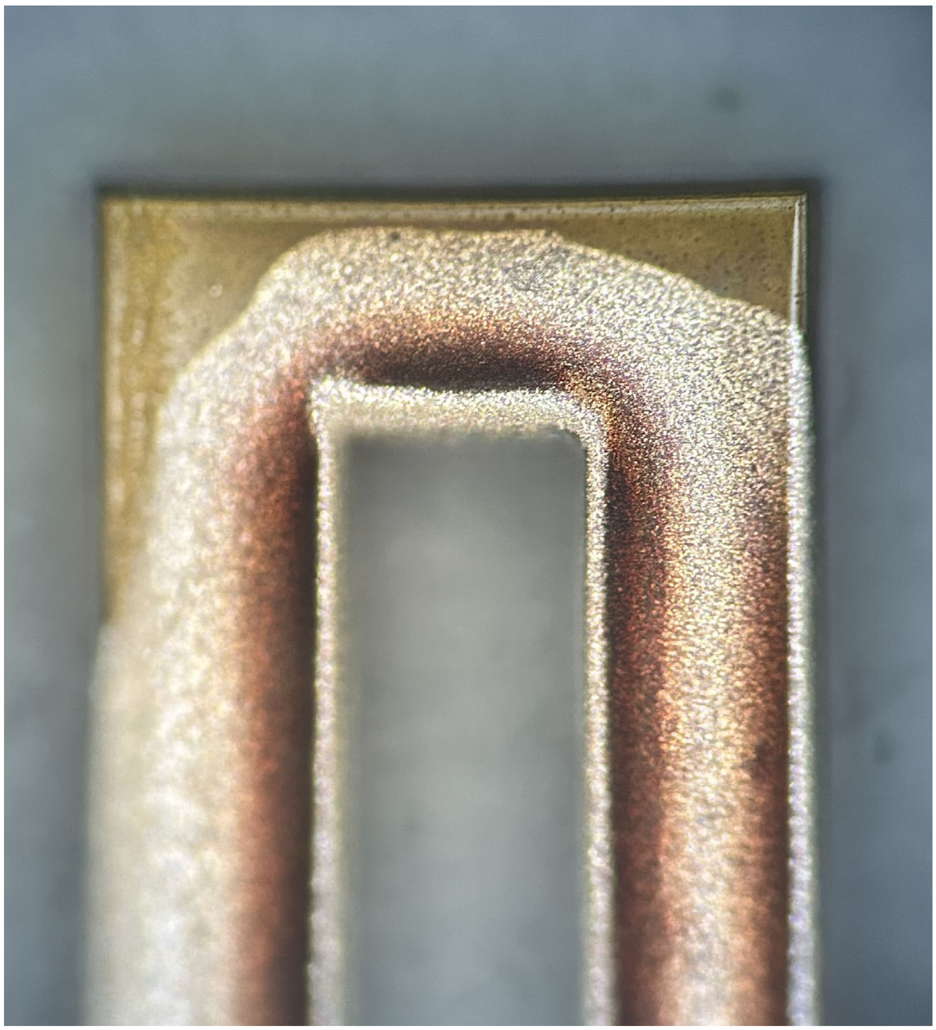

Figure 4.21: Springs without relief in laser cut path in bend corners.

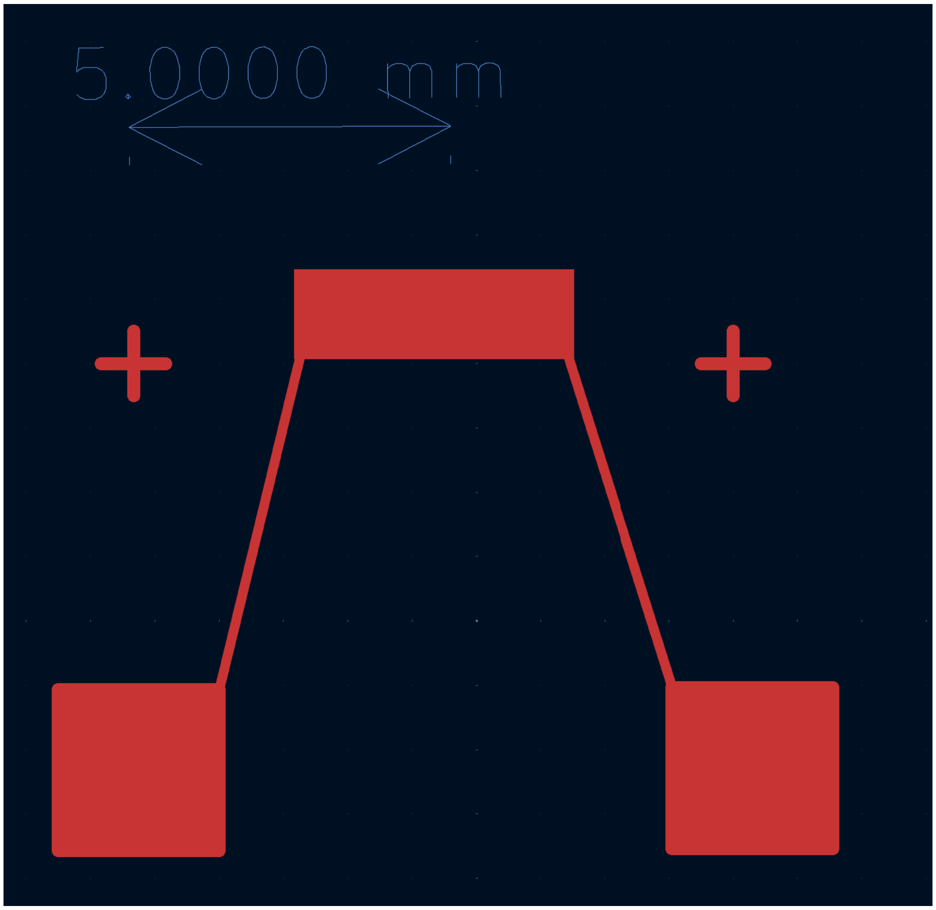

(a) Whole design.

(b) Laser cut paths.

Figure 4.22: Scaled down device design in KiCad.

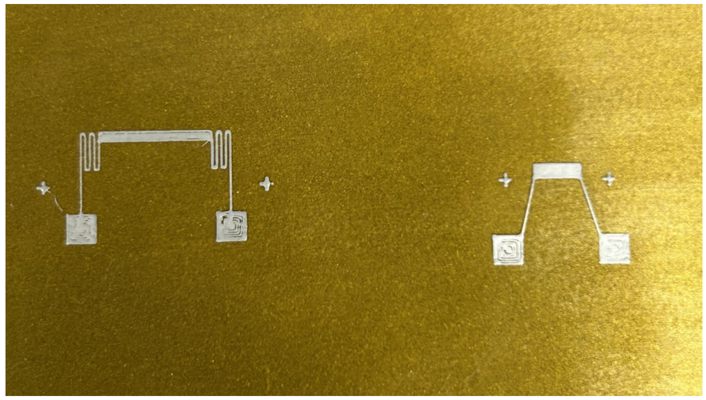

(a) Post-print.

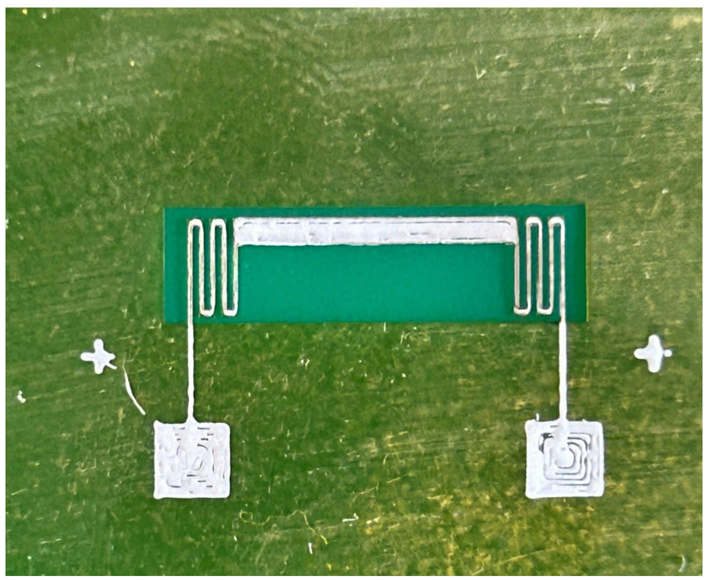

(b) Post-cutting, scaled up.

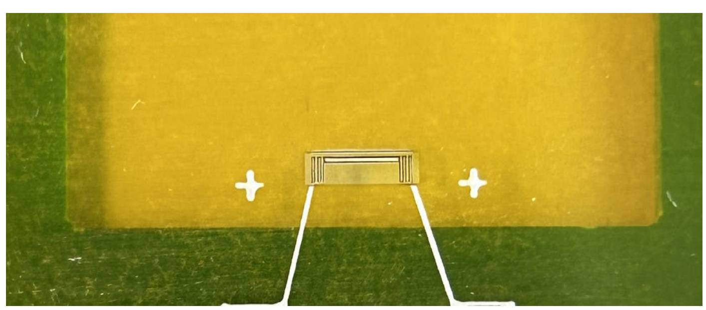

(c) Post-cutting, scaled down.

Figure 4.23: Printing and cutting results for Lorentz actuators.

4.5 | Testing and Results

4.5.1 | General Test Setup

The following test setup was used for both Lorentz actuators. The top piece of FR4 used to sandwich the DC electric field sensor of the previous chapter (Fig. 3.10) with the window cut-out was utilised. Each Lorentz actuator was taped down carefully and evenly atop the window, and a hard disk drive magnet was placed 1.6 mm below the device, underneath the FR4. Wires were soldered to copper tape with conductive adhesive, which were then attached to each printed contact pad for connection to a DC power supply. The entire apparatus was then placed beneath a Leica DM6-M microscope, as shown in Fig. 4.24. An Agilent E3640A [77] DC power supply was connected across the device and a series current-limiting resistor, and the resulting deflection was measured with the microscope.

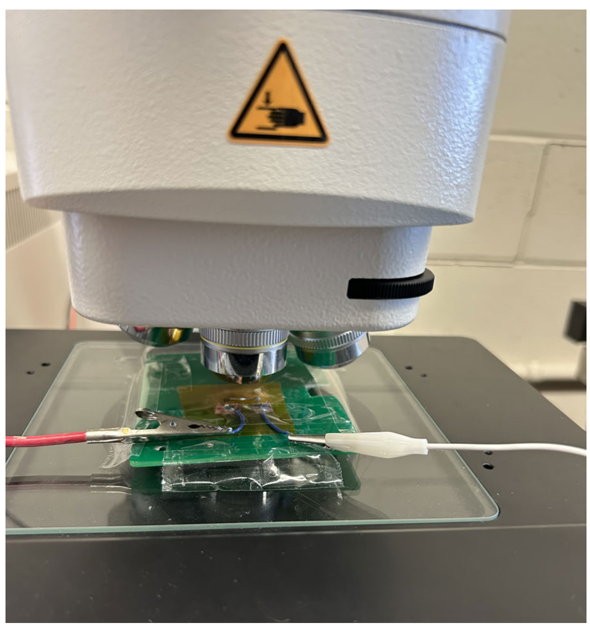

Figure 4.24: Lorentz actuator test setup.

4.5.2 | Scaled Up Actuator

The 4.8× scale Lorentz actuator was paired with a 560 Ω series resistor, and the current was swept from 0 to 30 mA. Since the device was found to have a total resistance of 1.4 Ω, this corresponded to a voltage sweep of 0 to 16.6 V. An AlphaLab Model GM2 gaussmeter was used to measure the field at the crossbar as 0.54 ± 0.1 T, perpendicular to the crossbar in the plane. The test results are shown in Fig. 4.25. The simulation results are scaled by a factor of 0.54/0.48 = 1.125, since they were found with a theoretical field of 0.48 T. The results closely matched simulation, further instilling confidence in the ink/PI COMSOL model. Also, the response was quite linear, justifying the neglection of Joule heating effects. The spring constant was calculated to be 0.23 N/m.

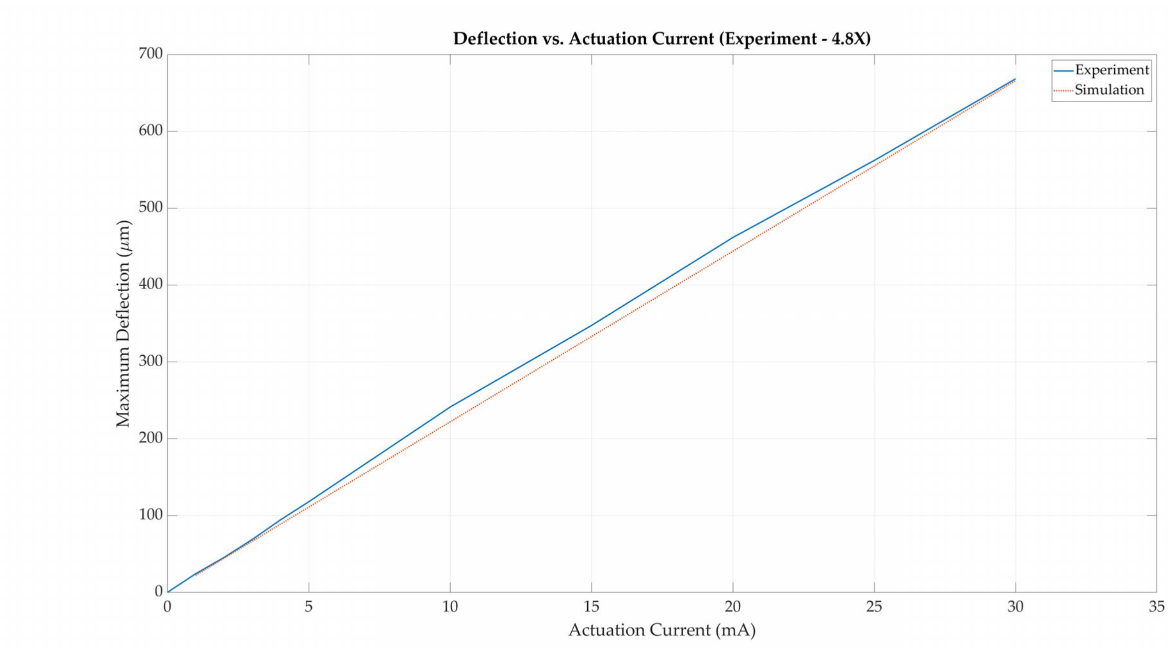

Figure 4.25: 4.8× Lorentz actuator test results.

4.5.3 | Scaled Down Actuator

The 1.5× scale Lorentz actuator was found to have a resistance of 6.4 Ω, and it was placed in series with a 56 Ω resistor. The current was swept from 0 to 30 mA in steps of 5 mA, corresponding to a voltage sweep from 0 to 1.9 V. The field at the crossbar was found to be 0.12 T; this differs from the 0.54 T field found in the previous section since the field present around the hard drive magnet was very localized. Fig. 4.26 shows the results, with the simulation once again scaled to the correct field strength. The response roughly follows the simulation until around 20 mA, where Joule heating effects begin to seep in. The spring constant was found to be 0.53 N/m.

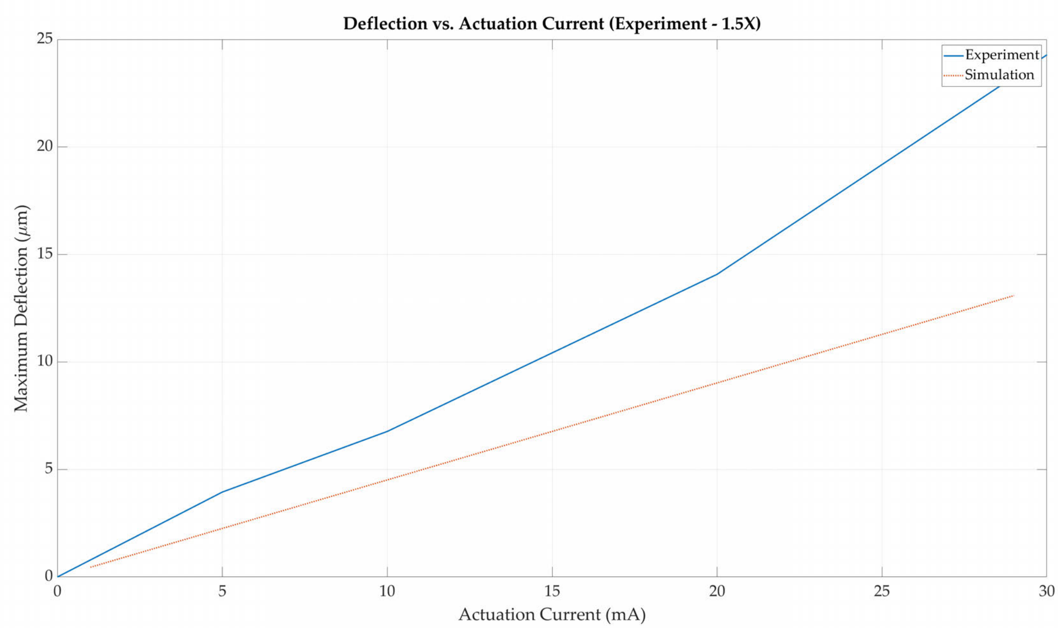

Figure 4.26: 1.5× Lorentz actuator test results.

4.5.4 | Comparison to Lithographic Device

The lithographic device [66] had a maximum deflection of 50 μm at 15 mA of actuation current, with a linear response and a sensitivity of 3.33 μm/mA. By contrast, the 4.8× device had a linear sensitivity of 23.1 μm/mA, with the tradeoff of being much larger. The 1.5× device, on the other hand, had a sensitivity of 1.42 μm/mA, while being on the same order of size as the lithographic device; the worse sensitivity attributable to the relatively larger spring constant. As for Joule heating effects, the lithographic device had a roughly 20 K increase in temperature for 10 mA of current, where as the PE devices had an increase of 0.05 K (1.5×) and 0.005 K (4.8×) for the same current. In terms of power consumption, the lithographic device consumed 14.7 mW of power at full stroke; the PE on the other hand consumed 5.8 mW (1.5×) and 1.3 mW (4.8×), consuming less power. Table 4.5 summarises the tradeoffs.

Table 4.5: Comparison of lithographic to PE Lorentz actuators.

	Litho.	**1.5×**	**4.8×**
Crossbar Length (mm)	2.08	3.12	9.90
Sensitivity (μm/mA)	3.33	1.42	23.1
Power Cons. (mW)	14.7	5.8	1.3
ΔT @ 10 mA (K)	10	0.05	0.005
Spring Constant (N/m)	0.14	0.53	0.23

Apart from performance, the PE required less processing steps and time to fabricate than the lithographic device. The fabrication steps required to manufacture the lithographic MEMS Lorentz actuator were as follows: SiO_2 deposition, KOH etch for cavity formation, KOH etch for crossbar formation, sputtering of Ti/Al/Ti, and finally actuator release. Each of these steps are both time- and resource-intensive, and may not guarantee functionality as the error accumulates at each processing step. On the other hand, both PE actuators proposed in this chapter were simply printed on the same substrate in a time-frame of 10 minutes, then subsequently cured for only 20 minutes. The laser cutting to release the PE actuators was the largest bottleneck, requiring roughly 30 minutes of cutting for each device.

Some key findings of this chapter are as follows. First, that ink resistivity decreases with cure time, as does adhesion to PI. Next, that Ag ink/PI PE yielded similar or much better results than lithography when the x-y scale factor was 4-5$\times$, and performance decreased with scaling as the spring constant grows. Lastly, for applications that don't necessarily require miniaturization below a roughly 100 μm minimum feature size, this method of fabricating MEMS devices could be a very attractive alternative to lithography in terms of cost and time savings.

5

Lorentz Actuator Relay

This chapter will explore the application of the printed electronics Lorentz actuator as a MEMS relay switch. Firstly, some background on relays is highlighted, followed by MEMS relays and their different operation modes. Then, the theory behind MEMS relays, in terms of contact types and switching response, is briefly shown, followed by the design and fabrication trials and iterations. Lastly, the device is tested and performance is compared to commercially available electromechanical and solid-state relays.

5.1 | Background

Relays are vital components of electrical systems, holding a central spot in the worlds of control systems, industrial automation, automotive, utility, and home appliances, to name a few [78]. They offer a robust and straightforward way to switch on or off AC or DC loads. Electromechanical relays often found in industrial and consumer electronics use an electromagnet to actuate a moving contact, which strikes and holds against a fixed contact to complete some circuit (Fig. 5.1 (a) [79]). Since they have no intermediate state between fully-on or fully-off, where power may be burned and let go as heat as is the case with the MOSFET, they dissipate very little heat. And, being that the input and output sides are usually physically separate systems or entities, they offer excellent isolation. Some drawbacks may include switching noise (both electrical and auditory), mechanical wear, and low switching speed compared to the MOSFET [78]. Solid state relays (Fig. 5.1 (b) [79]), on the other hand, utilise an optocoupler to switch loads. They are less noisy than electromechanical relays, and offer faster response times and longer lifetime, but suffer from heat generation as power is dissipated in the semiconductor. In designs sensitive to electromagnetic interference, and to meet compatibility standards, solid-state relays may be preferred to electromechanical.

MEMS relays typically work in much the same manner as their macro-sized counterparts, most commonly employing either electrostatic, piezoelectric, thermoelectric, or electromagnetic phenomena for actuating the contacts [80]. Electrostatic actuation involves using a cantilever or spring assembly to suspend one of the contacts over the other, under which lies a biased electrode. When a voltage is applied to the electrode, the top contact moves down to meet the fixed contact and completes the circuit. The required voltage is known as the pull-in voltage, a characteristic voltage of the dynamical system which causes the two electrodes to snap together. One of the main benefits of electrostatic actuation is near-zero power consumption; however, their main drawback is long-term reliability and wear-out, which scales exponentially with actuation voltage [81]. Piezoelectric actuation works by employing a piezoelectric material oriented to move contacts together or apart when a positive or negative polarity actuation voltage is applied to it, taking advantage of the converse piezoelectric effect. These devices are very fast and can overcome stiction, whereby the two contacts get stuck together. However, they suffer from fatigue, as the thin films of piezoelectric material wear out over many actuation cycles. Thermoelectric actuators use the principle of Joule heating and thermal expansion to move contacts together,

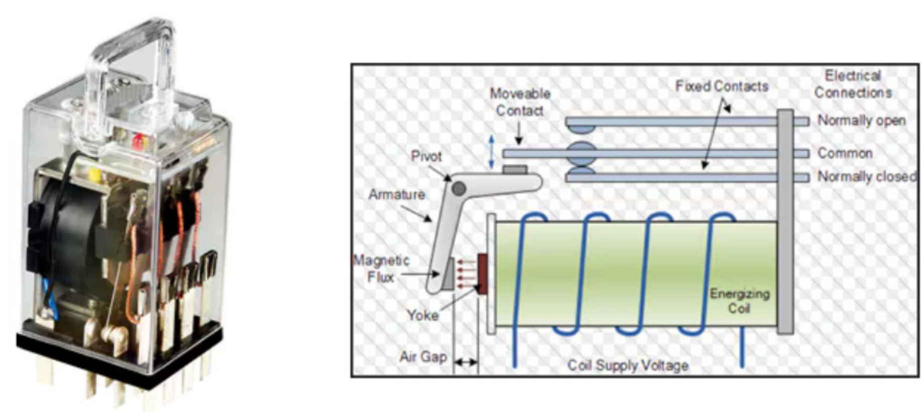

(a) Electromechanical relay.

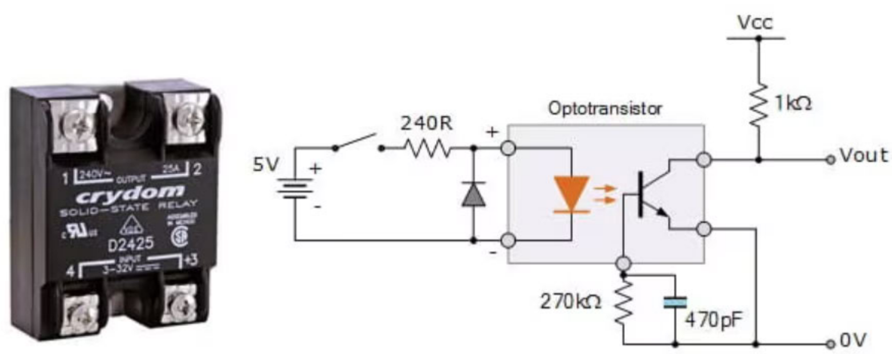

(b) Solid-state relay.

Figure 5.1: Common non-MEMS relay types.

typically in a bi-morph configuration (see Sec. 4.2.3.3). They are quite fast and can have high contact force (and therefore low contact resistance), but suffer from high power consumption for actuation. Mechanically bistable and latching topologies have been explored to mitigate the power requirements of thermoelectric actuation [82]. Lastly, electromagnetic actuation involves harnessing the Lorentz force to move two contacts together. Their designs require balancing the trade-offs of power consumption required for actuation with switching speed, physical size, processing technology, and contact force. They can also be more complex to manufacture, as they require the presence of a permanent magnet to supply the magnetic field flux. Some examples of each of the common MEMS relay types from the literature are shown in Fig. 5.2 [80, 83, 84, 85].

Due to the successful working of the Lorentz actuator (4.8$\times$ scale) from the previous chapter, it was thought that this design could be adapted into an electromagnetic relay. Its large range of motion means that, at small distances, it could produce an appreciable contact force and switching speed. The remainder of this chapter therefore discusses designing and fabricating a PE electromagnetic mechanical relay based on that actuator, and any theory or details concerned with the actuator itself will not be discussed in detail as it has already been covered in this thesis.

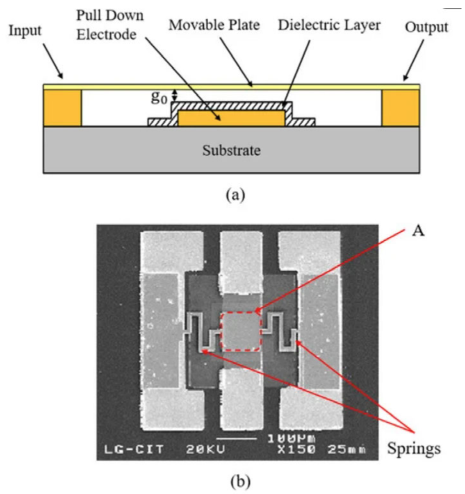

(a) Electrostatic. Reproduced from [80] under the terms of the Creative Commons Attribution (CC BY) License.

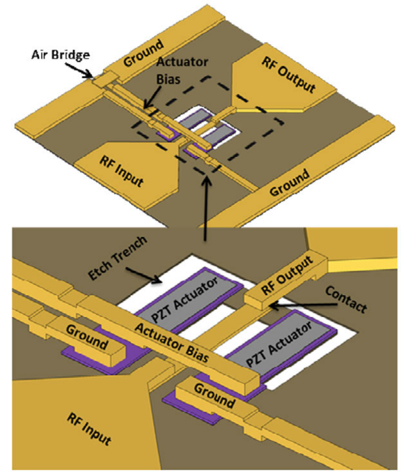

(b) Piezoelectric (©IEEE 2012). G. Schiavone, M. P. Y. Desmulliez, and A. J. Walton, "Integrated magnetic mems relays: Status of the technology," Micromachines, vol. 5, no. 3, pp. 622–653, 2014.

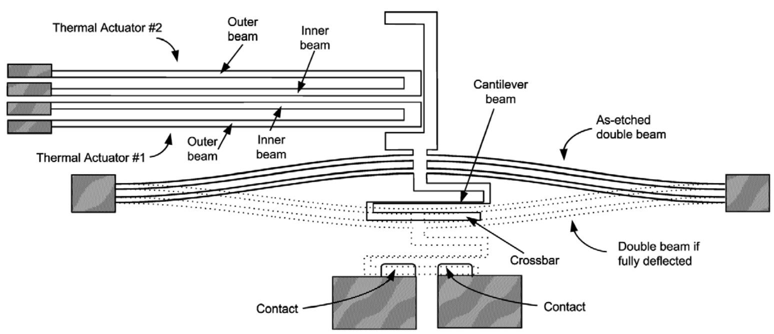

(c) Thermoelectric (©IEEE 2005). J. Qiu, J. Lang, A. Slocum, and A. Weber, "A bulk-micromachined bistable relay with u-shaped thermal actuators," Journal of Microelectromechanical Systems, vol. 14, no. 5, pp. 1099–1109, 2005.

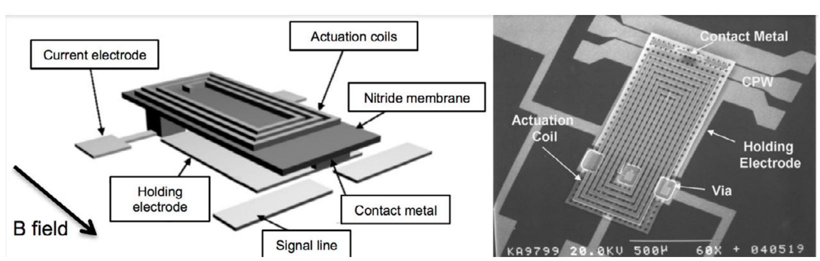

(d) Electromagnetic. Reproduced from [81] under the terms of the Creative Commons Attribution (CC BY) License.

Figure 5.2: Common MEMS relay types.

5.2 | Theory, Design, and Fabrication

5.2.1 | Theory of Operation

The following section deals with the theory behind relay contacts and switching, as well as some of the dynamics associated with switching. Although both lateral and vertical switches exist, this thesis will only concern itself with vertically-switched MEMS relays. They are more suitable to PE practices and have some advantages over lateral switches, including switching speed and contact resistance [86].

5.2.1.1 | Contacts

MEMS relays typically employ either reed [87], bridge [84], or cantilever [88] based contacts for vertical switching (Fig. 5.3).

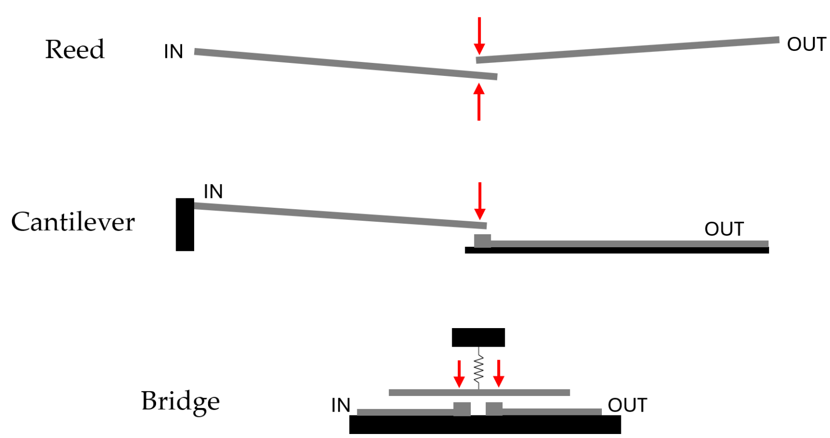

Figure 5.3: Relay contact types.

The shape of the contact is very important, as it dictates the effective contact resistance

R_C, given by [88]:

$$R_C = \frac{\rho}{2r_{eff}} \tag{5.1}$$

where ρ is the resistivity. For elastic deformation, r_{eff} is written as:

$$r_{eff} = \sqrt[3]{\frac{3F_C\delta}{4E_{eff}}} \tag{5.2}$$

where F_C is contact force, δ is radius of curvature of the contact, and E_{eff} is the effective Young's modulus. So, R_C is inversely proportional to $F^{1/3}$, and inversely proportional to $\delta^{1/3}$. Therefore, increasing both contact force and radius of curvature of the contact(s) improves (lowers) contact resistance. Contact force can be improved through mechanism design, whereas δ is a property of the contact shape and size. It is not entirely the force itself, but rather the pressure (force per unit area) which controls the resistance. A larger force over a smaller area leads to an even larger effective pressure.

5.2.1.2 | Switching

Vertical switching in MEMS relays is typically done with either cantilever or spring-suspended actuators. The actuator used in this chapter is the Lorentz actuator introduced previously, which is a spring-suspended actuator whose spring constant k can be approximated by 4.13. The behavior of the actuator due to a step input of force F_0 can be described by the differential equation [89]:

$$
\begin{aligned}
\frac{F(t)}{m} &= \frac{d^2x(t)}{dt^2} + 2\zeta\omega_0\frac{dx(t)}{dt} + \omega_0^2 x(t) \\
F(t) &= \begin{cases} F_0, & \text{if } t > 0 \\ 0, & \text{if } t \leq 0 \end{cases} \\
x(0) &= 0 \\
\frac{dx}{dt}|_{t=0} &= 0
\end{aligned}
\tag{5.3}
$$

where m is the mass and ζ is the damping ratio. After solving and applying initial conditions:

$$
\begin{aligned}
x(t) &= \frac{F_0}{k}\left(1 + \frac{s_2 e^{s_1 t} - s_1 e^{s_2 t}}{s_1 - s_2}\right) \\
s_{1,2} &= -\zeta\omega_0 \pm \omega_0\sqrt{\zeta^2 - 1}
\end{aligned}
\tag{5.4}
$$

Assuming that $\sqrt{\zeta^2 - 1} \approx \zeta - \frac{1}{2\zeta}$, then $s_1 \to -\frac{\omega_0}{2\zeta}$ and $s_2 \to -2\zeta\omega_0$. This means that the solution becomes:

$$
x(t) = \frac{F_0}{k(1 - 4\zeta^2)}\left(1 - 4\zeta^2 + 4\zeta^2 e^{-\frac{\omega_0}{2\zeta}t} - e^{-2\zeta\omega_0 t}\right) \tag{5.5}
$$

When $\zeta > 1$ the system is over-damped, when $\zeta = 1$ the system is critically damped, and when $0 < \zeta < 1$ the system is under-damped. For under-damped, the switch oscillates at ω_0. The maximum possible response time, then, would be approximately $2\pi/\omega_0$, as this is roughly the slowest it can move given a step input:

$$
t_{res} \leq \frac{2\pi}{\omega_0}
$$

5.2.2 | Design and Fabrication Trials

The following section outlines first the design constraints for the performance of the relay, then goes into the various design and fabrication trials that were endured. There were two types of relays that were designed and fabricated, a bridge-type and a cantilever-type. Reed-type was not explored.

The design of the PE Lorentz actuator relay began with a few constraints, based on commerically available relays (Songle SRD-05VDC-DL-C mechanical relay [90], LittleFuse CPC1017N solid-state relay [91]):

- Switching Time $t_{res} < 10$ ms
- Power Consumption $P < 100$ mW
- Contact Resistance $R_C < 7.1\ \Omega$
- Max DC Load Current 0.1 A $< I_{max} < 10$ A

5.2.2.1 | Bridge Contact Type

The first design that was drawn up used two parallel Lorentz actuators suspended over a bridge contact. The bridge contacts and traces for the relay load circuit were printed on FR4 using the Voltera NOVA, with same print settings and curing time/temperature as previously outlined in this thesis. At an attempt to decrease contact resistance, the traces were printed and cured first, and then the contacts were made by depositing a small dollop of ink, approximately 150 μm in height. The actuator was printed on 25 μm PI in two steps: first, the top Lorentz actuators were printed and cured until ink was dry (5 minutes), then the substrate was flipped over and the bottom contact was printed. Fig. 5.4 (a) shows the simulation model in COMSOL with one spring loop on the actuators and resulting print.

Using the Solid Mechanics module and similar simulation settings as other devices in this thesis, the deflections for one and two spring loops was 150 μm and 104 μm, with resonant frequencies of 35 Hz and 43 Hz, respectively. The one-loop design was opted for due to its slightly higher resonance.

After releasing the actuator in the laser cutter, it was laid atop the FR4 printed circuit with the contacts aligned with the bottom contact of the actuator. 200 μm thick glass slides were used as spacers between the contacts and the actuator. However, the gap distance was measured to be 100 μm with the Leica DM-6 M microscope, which was thought to be due to deformation/stress in the springs. The PI was secured with a piece FR4 with a small window cut out of it, similar to how the DC electric field sensor was tested (Fig. 5.4 (b). With a bench-top multimeter in CONT mode connected between the relay contact traces, and a 0.14 T field present across the actuators, the actuation current in the actuators was increased. The device hardly deflected, moving only 10-20 μm even with >100 mA of actuation current in each actuator. Upon closer inspection, it appeared that the actuator contact was only hitting one of the fixed contacts, and tilted transversely about it as the device actuated. It was clear that two issues were present:

- **Problem**: The device was hardly moving at all, even with appreciable amounts of actuation current. **Cause**: The two opposing Lorentz actuators both acted like cantilevers, but because they were attached to each other, they pulled on each other and re-directed some of the Lorentz force into the x-y plane. **Proposed Solution**: Abandon the dual-Lorentz actuator design in favour of a single actuator.

- **Problem**: The device sat too high above the contacts, creating unnessecary space that the actuator had to travel just to make contact. **Cause**: As the ink cures, its volume decreases due to solvent evaporating, which introduces a compressive stress on that

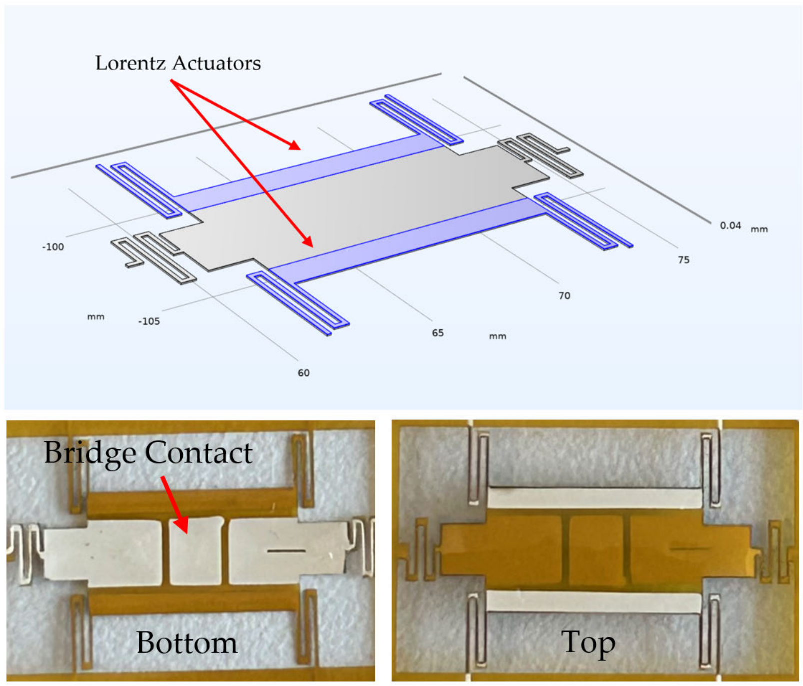

(a) COMSOL model and print.

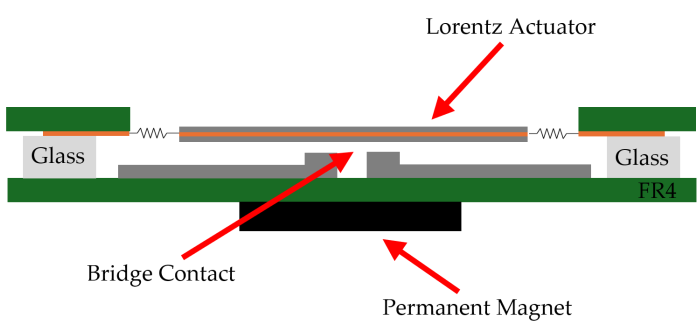

(b) Side view of test setup.

Figure 5.4: Bridge-type dual-Lorentz actuator relay.

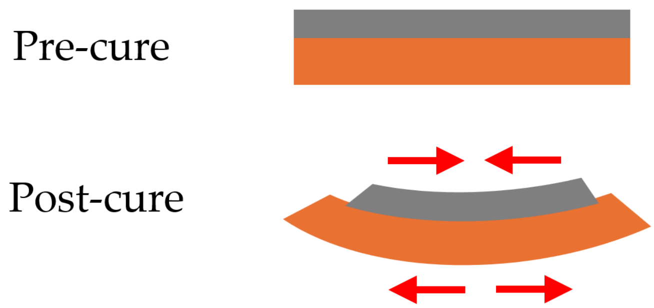

Figure 5.5: Effect of stress imbalance during curing.

side of the PI and deforms the print. On the small springs, this effect is magnified, and pulls up on the structure (Fig. 5.5). **Proposed Solution**: Print the same design on both sides to reduce stress, *or* use the stress as an advantage to decrease gap space.

To address the first issue, the Lorentz actuator design of the previous chapter was augmented to include a protruding reed (Fig. 5.6). As for the second issue, the design was printed only on one side, but flipped over when tested so that the structure was slightly bent downward as an effort to reduce gap space. COMSOL showed that this design had a resonant frequency of 35 Hz. Again, the design was aligned over the contacts and tested similarly. The structure moved much more than the dual-actuator design, with roughly 200 μm of movement for 100 mA of actuation current and 0.14 T field. However, the device was hitting only one of the contacts even still. It appeared that the problem laid in the fact that the fixed contacts were inconsistent heights, and it would be challenging to get them to be equal height. It was then thought that this design could be altered into a cantilever-type contact relay, rather than a bridge-type.

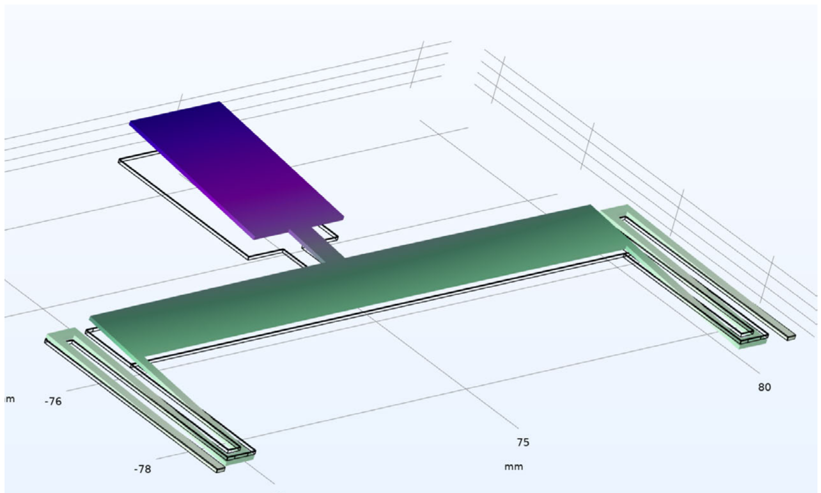

Figure 5.6: Single Lorentz actuator COMSOL model for bridge-type relay.

5.2.2.2 | Cantilever Contact Type

The design of Fig. 5.6 was not changed significantly at first. Instead of ink on only one side, the design was printed on both sides identically. This offered two benefits: 1) the stress imbalance would be resolved, and 2) the underside of the springs could be used as a conduction path for the relay load current. COMSOL showed that this affected the deflection by reducing it to roughly half that of an identical one-sided print, and that it had a resonance of 35 Hz. Only one fixed relay contact was used now, printed similarly on FR4 along with a small dollop of ink, measuring 140 μm in height. Also, the un-cut print was attached to rigid poster board material with double-sided tape before cutting, so that handling the delicate device post-cut would not present any risks of damaging the fragile springs. The entire device could then be laid upon the FR4 circuit and secured more firmly than previously with the FR4 window. Upon testing, however, another issue arose: the ink on the top (Lorentz actuator) side of the actuator was electrically connected to the bottom (relay contact) side. This was because, when laser cutting through ink-PI-ink, the two ink layers actually fused together in some places due to the heat of the laser and the relative thinness of the PI substrate. However, the cantilever-type contact in general did work, and the device was able to make full contact. So, the design was changed slightly to include a 'tail' on the underside, which provided a conduction path for the relay's load that was not directly below the Lorentz actuator's springs (Fig. 5.7). An extra spring loop was added, also, in case that the tail increased the effective spring constant by too much. This reduced the resonance to 27 Hz in COMSOL. Care was taken, also, during laser cutting, to ensure that the laser was only ever cutting through ink-PI. Fig. 5.8 shows a 3D rendering of the device top and bottom to better illustrate the ink patterns. Now that a working device was achieved, it was time to take data and characterise the relay's performance, which is shown in the next section.

5.3 | Testing and Results

Fig. 5.9 shows the test setup for the working Lorentz actuator relay. The field present, due to a permanent magnet placed below the FR4, was 0.22 ± 0.1 T. The actuator was tested at 100 mA of actuation current, requiring 0.36 V across the device (36 mW power consumption).

Firstly, response and settling time was found. This was done using 2 channels on an oscilloscope, one connected to the gate (Lorentz actuation current signal) of the relay, and the other to the drain, with a voltage source connected to the source. The step response for turn-on and turn-off was taken, and examined in MATLAB. Fig. 5.10 shows the results for response and settling time, with the zoomed-in portions showing it more clearly. The response time was found to be 0.5 ms, whereas the settling time was 1.6 ms. The noise present in the plots is thought to be due to discretization noise of the oscilloscope, with

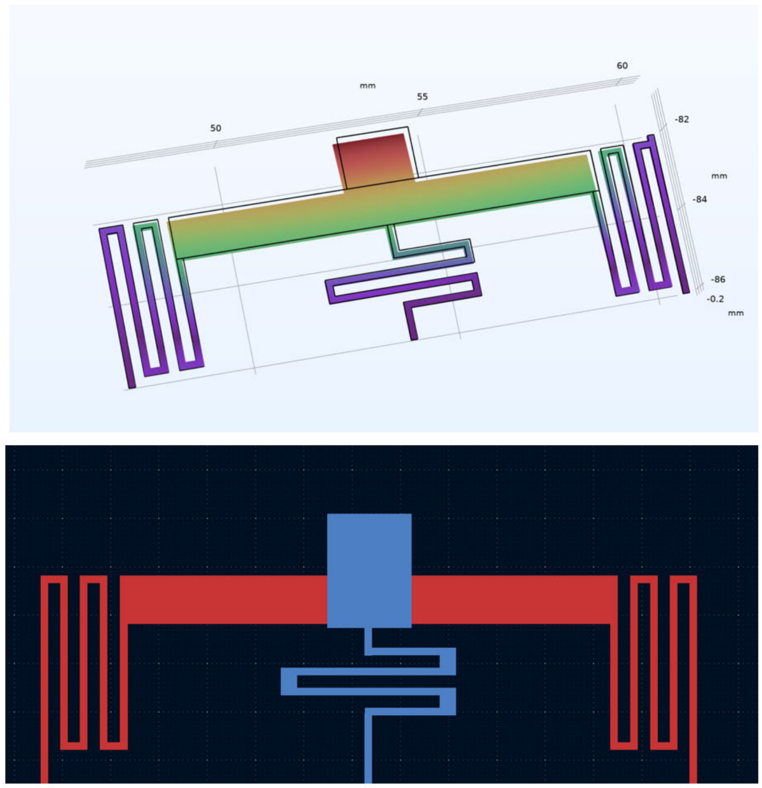

Figure 5.7: COMSOL model (top) and KiCad file (bottom, blue = bottom-side, red = top-side).

some 60 Hz mains voltage noise present when the relay is off.

Next, the contact resistance was found by creating a rudimentary current source through the closed relay and measuring the voltage across the contacts. This involved simply a 1 kΩ resistor in series with the relay. Assuming that the contact resistance was on the order of 1 Ω, then the error was around 0.1%. Applying 1 V to the source of the relay, a 7.65 mV voltage was measured across the contacts, meaning that the contact resistance was 7.65 Ω per Ohm's law. Fig. 5.11 shows a schematic of the test.

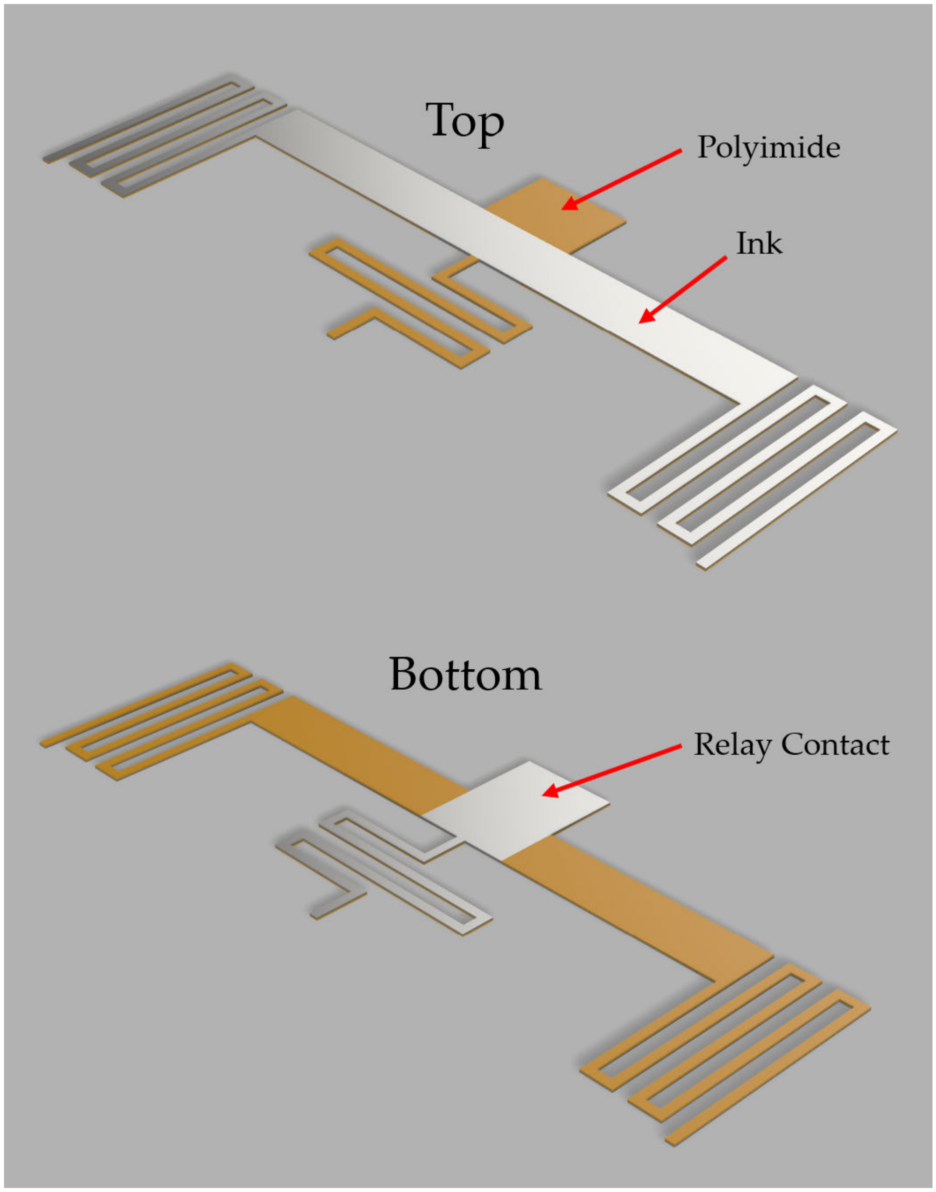

Figure 5.8: 3D view of top and bottom of PE relay.

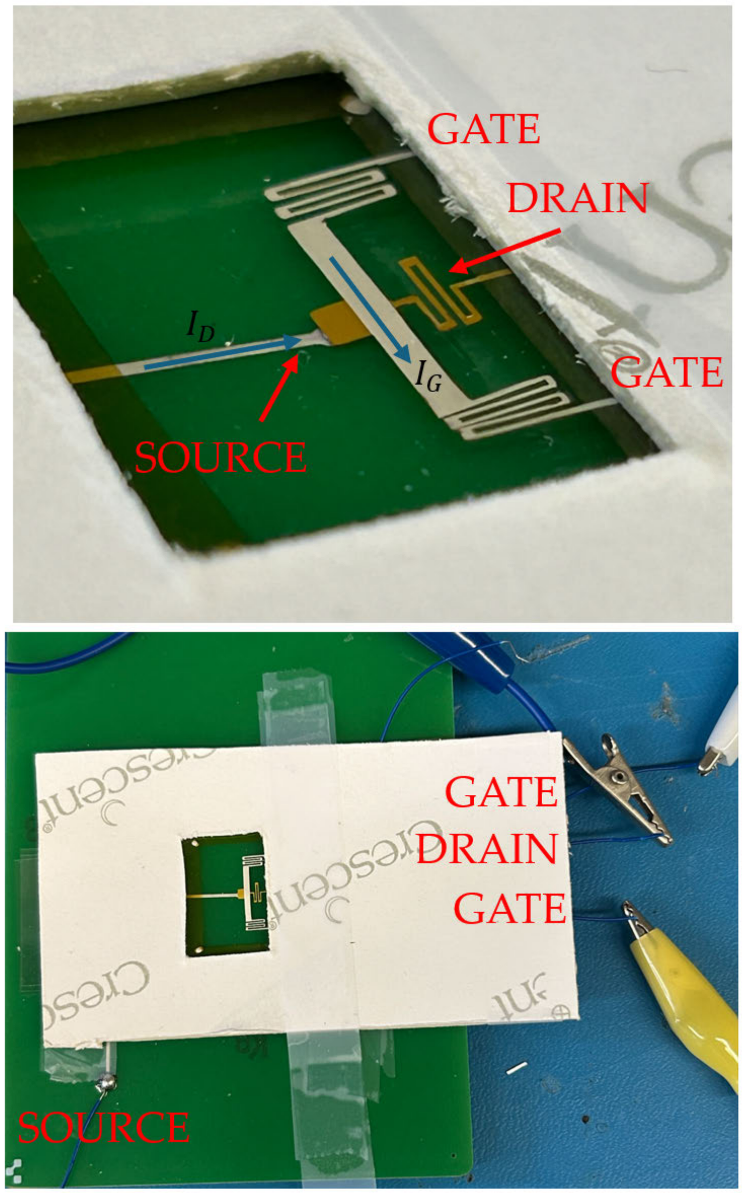

Figure 5.9: Relay test setup. I_G is actuation current for Lorentz actuator, I_D is load current for relay.

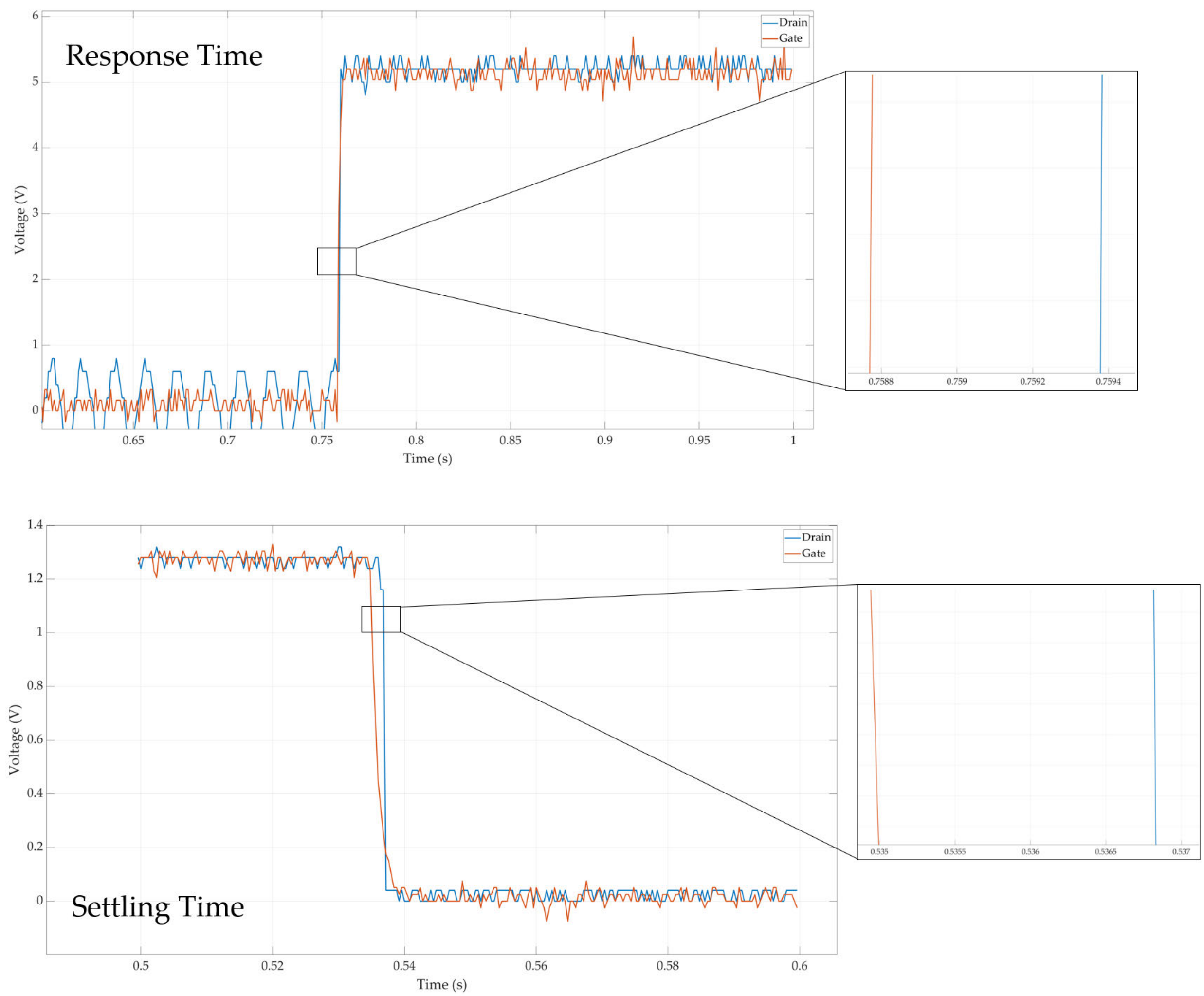

Figure 5.10: Response (top) and settling (bottom) of relay.

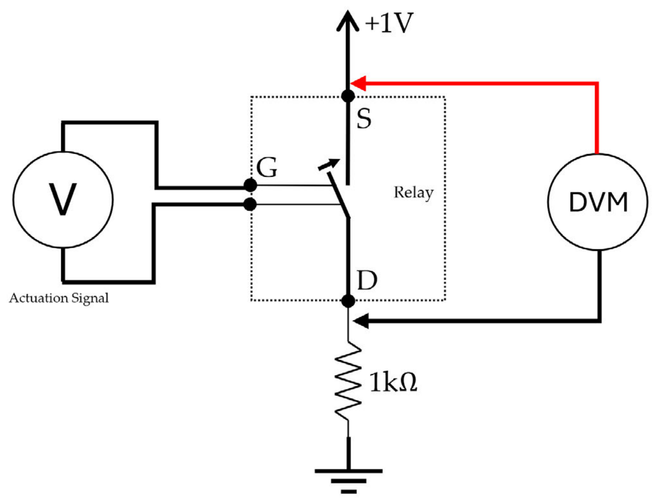

Figure 5.11: Schematic of test setup for contact resistance.

The resonant frequency was found by pulsing the actuation current at different frequencies and observing the output of the drain on an oscilloscope. In theory, at frequencies above and below resonance, the relay makes imperfect contact and the output can bounce. However, at resonance, the deflection is amplified significantly, and the device makes excellent, strong contact with minimal bouncing. Fig. 5.12 shows the different frequencies that the actuator was driven at, and it is clear that around 35 Hz, the bouncing effect is not present, and so this is where resonance lies. Note that the present of bouncing means that the spring structure is slightly underdamped, rather than the ideal situation of being overdamped.

The maximum DC load current of they relay was found by simply placing a DC power supply across the contacts, similar to Fig. 5.11 but with no external series resistor. The current was swept at a rate of 10 mA per second until the device failed, which occurred at 210 mA. Failure was concentrated at the serpentine tail, where Joule heating and thermal

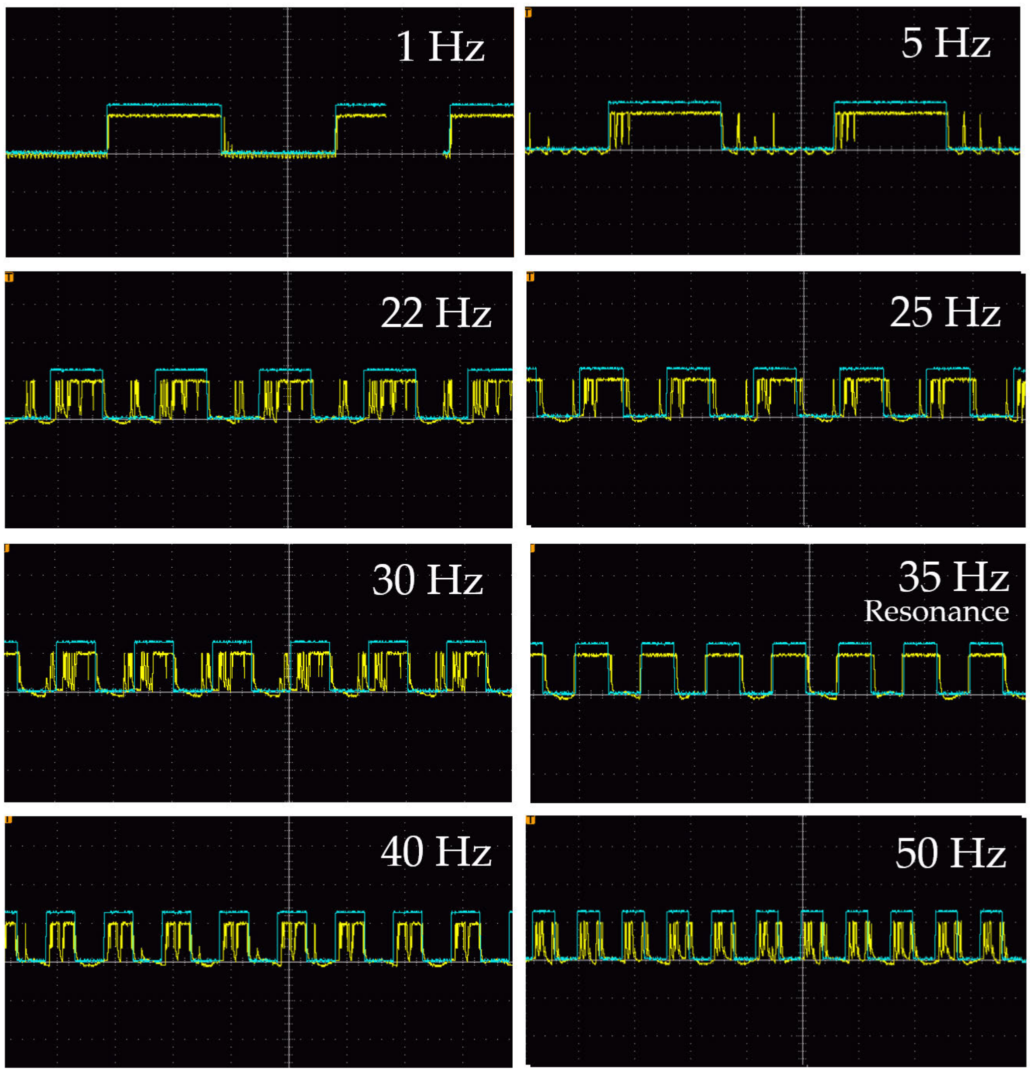

Figure 5.12: Resonance data from oscilloscope traces (blue = gate, yellow = drain).

expansion appeared to have caused the ink to separate slightly from the PI, causing an open circuit.

Lastly, reliability was tested. A small circuit consisting of an Arduino with SD card attachment was used to drive the actuator through a MOSFET, and then use on-board ADC to observe the signal at the drain and record either a successful or failed contact event on the SD card. The relay was turned on/off with 100 mA actuation current, on for one second and off for one second, and let run for approximately 64 hours (230,000 cycles), during which it did not fail.

Table 5.1 shows a comparison between this PE relay and the commercially available relays mentioned earlier (Fig. 5.13). The PE relay outperforms the mechanical relay in power consumption and switching time, but its contact resistance is an order of magnitude higher. It is comparable to the solid-state relay in contact resistance, outperforms it in switching time, but does not do as well in consumed power. The PE relay allows for more DC current flowing across its contacts than the solid-state device, but far less than the mechanical one.

Table 5.1: Comparison of PE relay to commercial relays.

	SRD-05VDC-SL-C	**CPC1017N**	**This Work**
Switching Time (ms)	10	1.2	0.5
Contact Resistance (Ω)	0.1	7.1	7.65
Power Consumption (mW)	450	0.5	36
Maximum DC Load Current (A)	10	0.1	0.21

This chapter has shown the development of a printed Lorentz actuator relay. Key takeaways are: one-sided ink-PI designs can have stress imbalance, and that this effect is minimized when printing on both sides; cutting through ink-PI-ink layers may cause the two ink layers to connect with each other; and, the PE electromagnetic relay offers comparable performance to commercially available relays, highlighting the viability of these methods

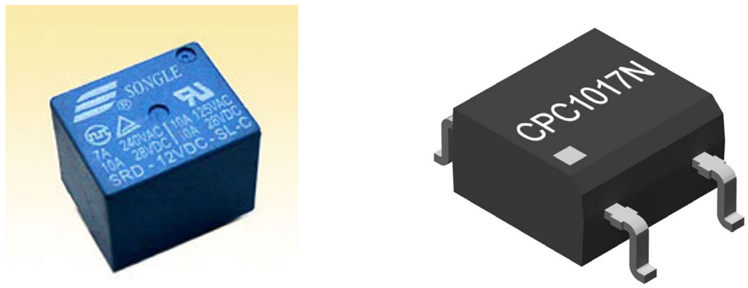

Figure 5.13: Commercially available relays; electromechanical (left) and solid-state (right).

for fabricating electromechanical devices.

6

Conclusion

This thesis demonstrated the feasibility and performance of printed electronics (PE) for the fabrication of MEMS-scale transducers using a direct-write extrusion method. Three devices were designed, fabricated, and tested: a DC electric field sensor, a Lorentz actuator, and a Lorentz actuator-based relay. Key conclusions and findings from each chapter are summarized here.

In Chapter 3, a force-deflected DC electric field sensor with capacitive interrogation was designed, printed, and tested. The sensor utilized a serpentine spring-supported electrode to enhance sensitivity while maintaining mechanical compliance. Compared to a lithographically fabricated MEMS counterpart, the printed version demonstrated a noise-limited resolution of 4.7 kV/m with signal averaging, out-performing the MEMS device (16.2 kV/m). But, the PE device was not as sensitive, attributable to its larger size and spring constant. In addition, the dependence of printed line width and height on dispense pressure and speed was found for a 150 μm nozzle configuration, showing that both width and height increase as pressure increases and speed decreases. Also, the Young's modulus value of Voltera Conductor 3 silver ink was found to be 1.781 GPa, found through comparing a real-life cantilever test structure with COMSOL digital twin simulation.

In Chapter 4, two Lorentz actuators based on a lithographic MEMS design—a 4.8× and 1.5× scale—were fabricated via extrusion printing and compared to both each other and the parent MEMS design from which they were derived. The 4.8× scale showed a linear response with sensitivity 23.1 μm/mA, closely matching simulation, and experienced negligible Joule heating effects. Its power consumption at maximum deflection was 1.3 mW. The 1.5× scale device showed some adverse Joule heating effects above 20 mA actuation current, power consumption of 5.8 mW, and a lesser sensitivity of 1.42 μm/mA due to its larger spring constant. On the other hand, the MEMS design showed a power consumption of 10 mW and sensitivity of 3.33 μm/mA, as well as enhanced Joule heating effects. In addition to the Lorentz actuator, the coefficient of thermal expansion for Voltera Conductor 3 ink was found to be 40 $\times 10^{-6}$ 1/K, as well as the dependence of ink resisitivty and adhesion to polyimide on cure time. It was found that as cure time increases, adhesion degrades but resistivity improves. At roughly 20 minutes cure time at 120 °C, adhesion is best, and resistivity is 1.07 $\times 10^{-7}$ $\Omega\cdot$m.

In Chapter 5, a relay based on the Lorentz actuator from Chapter 4 was designed, fabricated, and tested. Initially, a bridge-type contact was employed, but this did not work as the two fixed contacts could not be reliably fabricated using DIW to be the exact same height and shape. Also, the problem of un-even stress on the substrate with ink on only one side was addressed by printing the same design on both sides of the polyimide, effectively cancelling out any stress. A cantilever-type design was then utilised, with a single fixed contact. A small dollop of ink, roughly 150 μm in height, was used to achieve a pointed end, which was meant to improve contact pressure and therefore contact resistance. The design worked well, but the act of laser cutting the device fused the two opposite ink layers together. The device was re-designed so that the laser cutter would only ever cut through one layer of ink, not two, to avoid any shorting between two layers. The resulting design used a Lorentz actuator on one side for moving the relay, and the relay contact itself on the other side, which contacted the fixed contact below. This design acheived a response and settling time of 0.5 and 1.6 ms, respectively, and power consumption of 36 mW, outperforming a common electromechanical relay. Its contact resistance of 7.65 Ω was not nearly as competitive, but comparable to a common solid-state relay. Reliability was tested and the device did not fail after 230,000 actuation cycles.

Overall, this thesis has demonstrated the feasbility and viability of utilising extrusion printing of silver ink for fabricating MEMS transducers. The devices presented in this thesis have comparable metrics to their lithographic or commercially available counterparts, highlighting that extrusion printing is a valid method for fabricating and/or rapidly prototyping some MEMS designs. Some future work could include: exploring and characterizing other conductive or functional inks, as well as substrates other than polyimide; refining printing techniques, such as exploring different nozzle geometries, to achieve sub-150 μm resolution; ordering the PE designs in this thesis from a commercial PCB manufacturer and comparing performance metrics; packaging the devices from this thesis to make them robust to environmental disturbances, such as vibration, moisture/humidity, and temperature.

A

Printed Electronics Workflow

This appendix is meant to describe the step-by-step process for producing flexible/printable MEMS devices using KiCad for design layout, Voltera NOVA for printing, and the Oxford Series-A laser cutter for micromachining. This is also meant to act as a manual for those wanting to re-create the devices found in this thesis, or make their own.

A.1 | Design Layout

Design layout for this thesis was carried out in KiCad. First, create a new project and navigate to the PCB editor. Designs are created on a layer - in traditional PCB manufacturing, these layers all serve a particular purpose in the stackup of the PCB. However, for this workflow, any layer can be used. If multiple prints are present in the same design (for example, multi-layered designs, multi-ink, or multi-substrate designs), then each inhabits a unique layer of its own. Create your design using polygons, traces, etc. Fig. A.1 shows a completed 1-layer design on the F.Cu layer.

Fiducials, or alignment markers, should be included for alignment later on, whether that be with a laser micromachining tool or some other required alignment. Also, if a trace

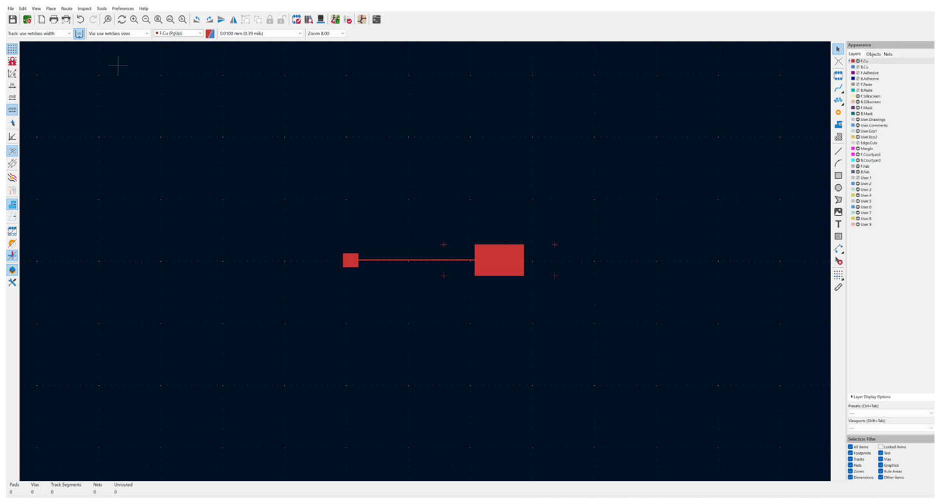

Figure A.1: Typical KiCad screen with design.

is prescribed as being 200 μm wide in a design, then the trace in KiCad should be made as thin as Voltera's software allows (typically 150 μm), then use the dispense pressure and dispense speed to get the required printed line width.

Once the design is finished, it can be exported (Fig. A.2). This is done by selecting *File » Fabrication Outputs » Gerbers*. Then, select the layers you would like to export, and press Plot. The gerber files, to be loaded into Voltera's software, will appear in the working directory.

It is also sometimes necessary to export a DXF file which contains cut paths for the laser cutter. First, the cut paths must be manually laid out, typically in the Edge Cuts layer. If the design includes small delicate springs, it is advisable to cut these first then move on to larger sections, thus having multiple DXF cut layers. Make sure to include fiducials in the cut path that align with the print's fiducial markers. Once the cut path is made (Fig. A.3), follow the same steps in exporting the layer, except now select DXF as plot format (Fig. A.4). Make sure to set units to mm, and un-check 'Plot graphic items using their contours'.

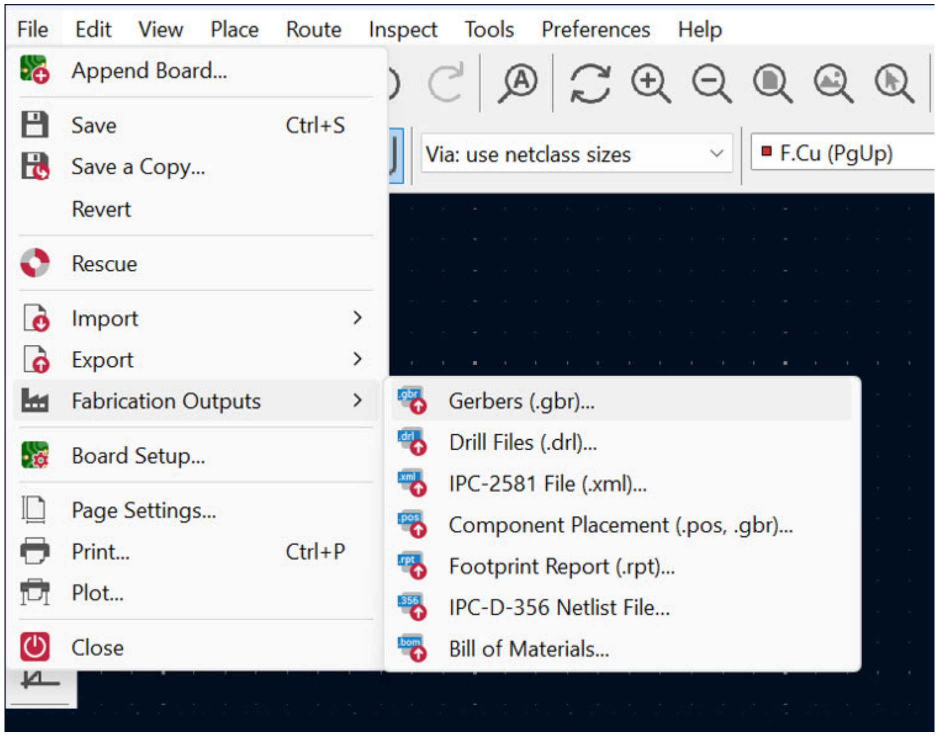

(a)

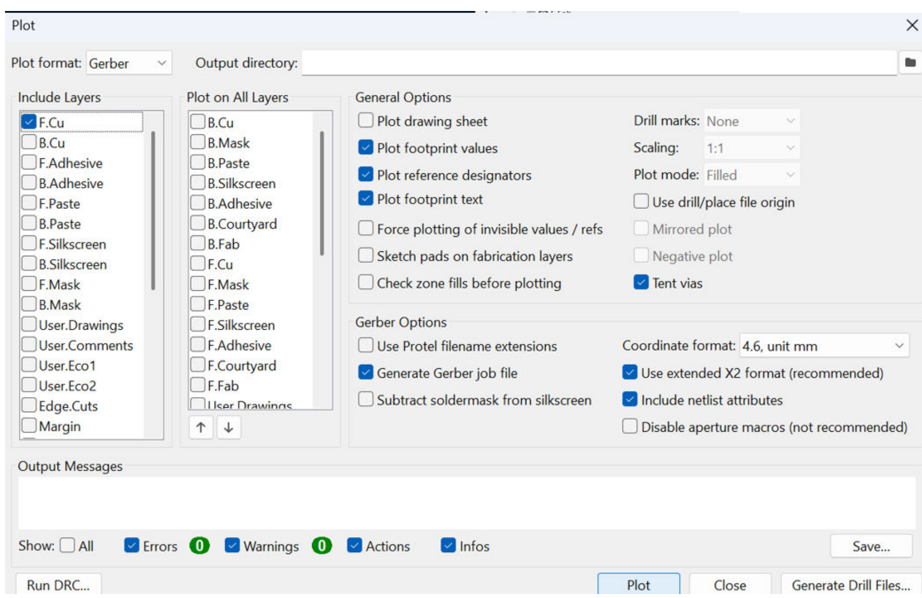

(b)

Figure A.2: Exporting layers in KiCad.

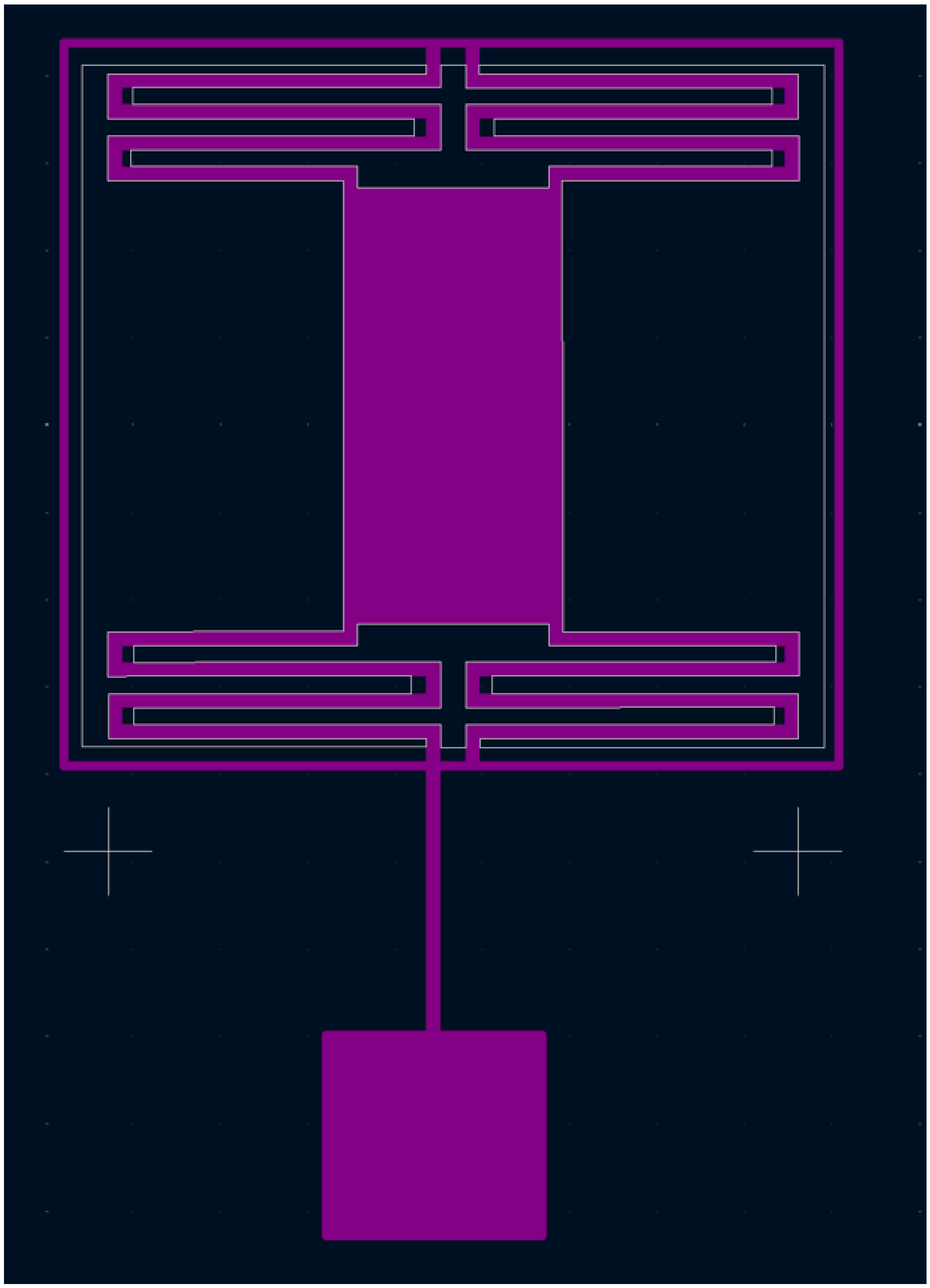

Figure A.3: KiCad design with cut path (grey).

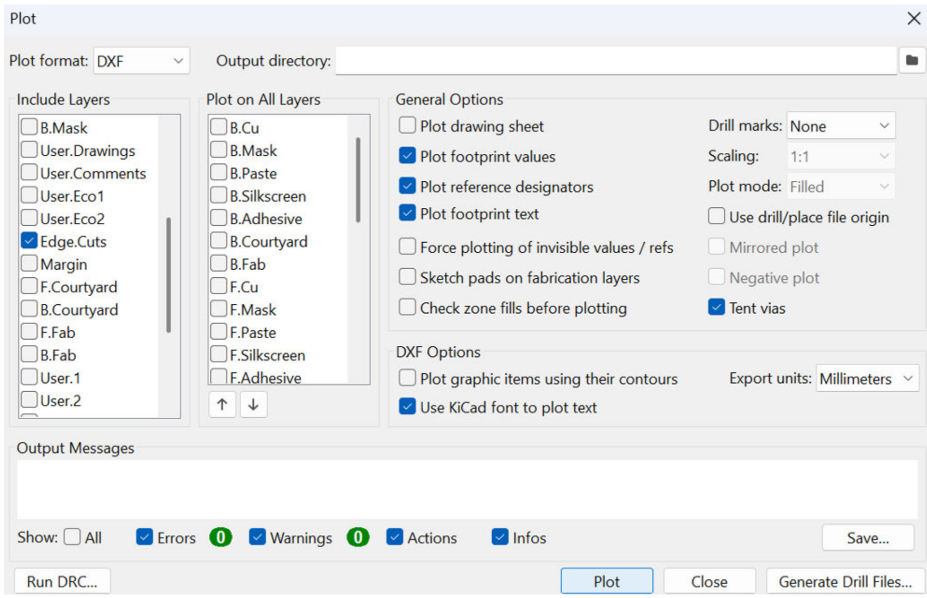

Figure A.4: Exporting DXF laser cut path in KiCad.

A.2 | Voltera NOVA

Once the gerber file has been generated for a design, it can be loaded into Voltera's software. To access the NOVA, make sure it is powered on and connected to the internet, then go to myvoltera.io. After selecting the machine, you will be greeted with the home screen. Click *Dispense*, then load the gerber file into the software and click *Next*. After this, you will need to select the ink you are using, as well as the substrate. Each has their own profile which you can either make from scratch or use from the default library. Next, mount the substrate. If it is a flexible substrate, the vacuum will turn on. Then, you will have to align the print. This is done in two steps. First, you click a reference or pivot point on the print geometry that you would like to use for positioning. Then, the camera underneath the gantry head will position itself over the substrate and overlay the print geometry so that you can move it around and make sure it either fits on the substrate or aligns with other features already present (Fig. A.5). In addition, you can set the rotation of the print.

Once the print is aligned, the substrate is probed to map the z-height profile. First, mount the probe on either of the mounting heads, and click *Probe*. The probe will first move to the calibration button and center itself, then it will probe the calibration printing plate, and lastly the substrate itself (Fig. A.6).

After probing, the dispenser can be assembled and mounted. Fig. A.7 shows the parts of the dispenser. To assemble, turn and remove the black top section off the dispenser, and undo the thumbscrew and open up the pressure sensor housing near the bottom. Insert a clean pressure sensor, then insert an ink cartridge through the top and into the pressure sensor. Re-latch and screw down the pressure sensor housing, then replace the black top section of the dispenser. Screw in a nozzle at the bottom, and then turn the top thumbscrew counter-clockwise to move the plunger down. Keep turning the plunger screw until ink *just* starts to come out of the nozzle, then back off the screw clockwise about half a turn. The dispenser is now assembled and primed. Mount it, and wait for the cartridge to heat up to the specified preheat temperature.

Next, the dispenser must be calibrated before printing. It first moves to the calibration button to center itself, then to the calibration plate to print a series of 3 lines. You can interactively adjust dispense pressure as its printing, and, in between printing sequences, you can enter the settings and adjust print speed and other factors. The goal is to get tight lines with no breaks and minimal ink spreading, which usually takes a few calibration sequences to achieve. Fig. A.8 shows this process.

After calibration, printing the loaded pattern can commence. Simply press *Start*, and the dispense head will move to the substrate location defined the in the alignment step and begin printing with the parameters from the calibration step. Again, dispense pressure can be interactively adjusted. After repeated prints, the pressure may need to be backed

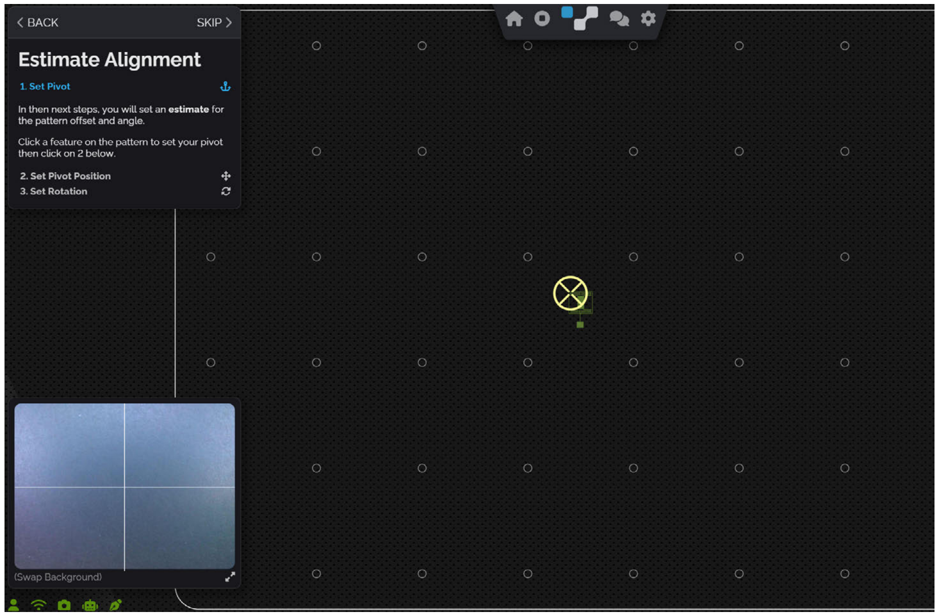

(a) Set pivot point.

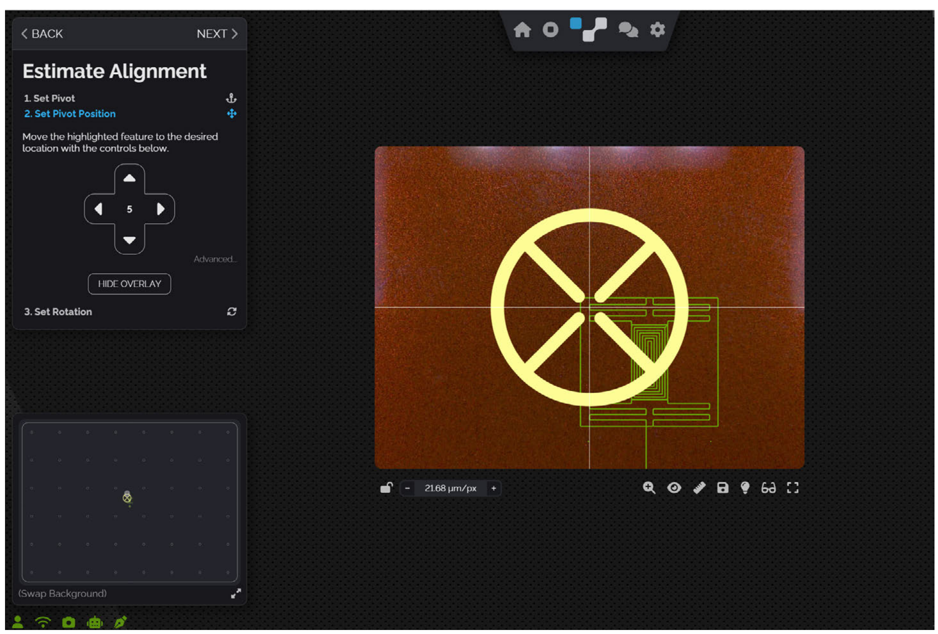

(b) Position print.

Figure A.5: Aligning print.

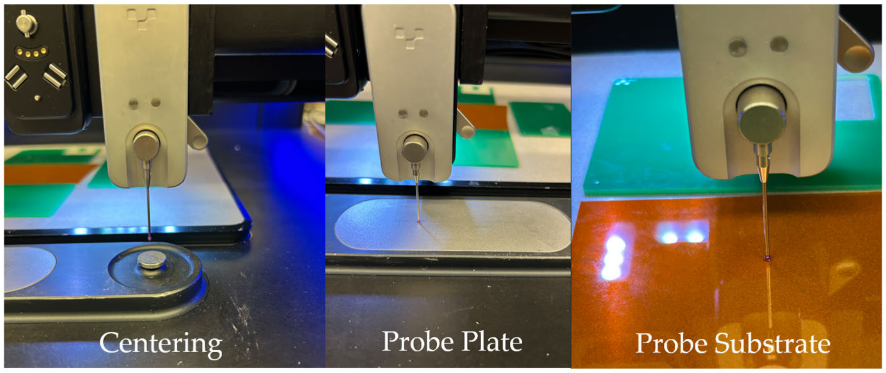

Figure A.6: NOVA probe sequence.

off slightly. If a print is unsatisfactory, simply wipe it away with IPA and try again. If certain parts of the print need printing again, click on the specific traces in the software and click *Start* again. Fig. A.9 shows the GUI and a live picture of the printing process. After printing, click *Finish* to release the vacuum and carefully remove the print from the printing stage. Place it in a box oven to cure.

A.3 | Laser Micromachining

After prining and curing the pattern, it may be necessary to laser cut and release some features. To do so, start with turning on and signing into the Oxford Series-A laser interface A.10. If the G-code for the laser cut path has not already been generated and placed in an ANC file, then it is necessary to open AlphaCam software and render the G-code. There are basically three steps in AlphaCam to generate the G-code. First, import the DXF file (*File » Input CAD*), set the tolerance for line breaks to 0.0001, and move the design so that the bottom left-most fiducial is at coordinates (0,0). Then, define the cut direction by selecting the Cut Direction option in the top toolbar. Select CW as direction and Inside as side for

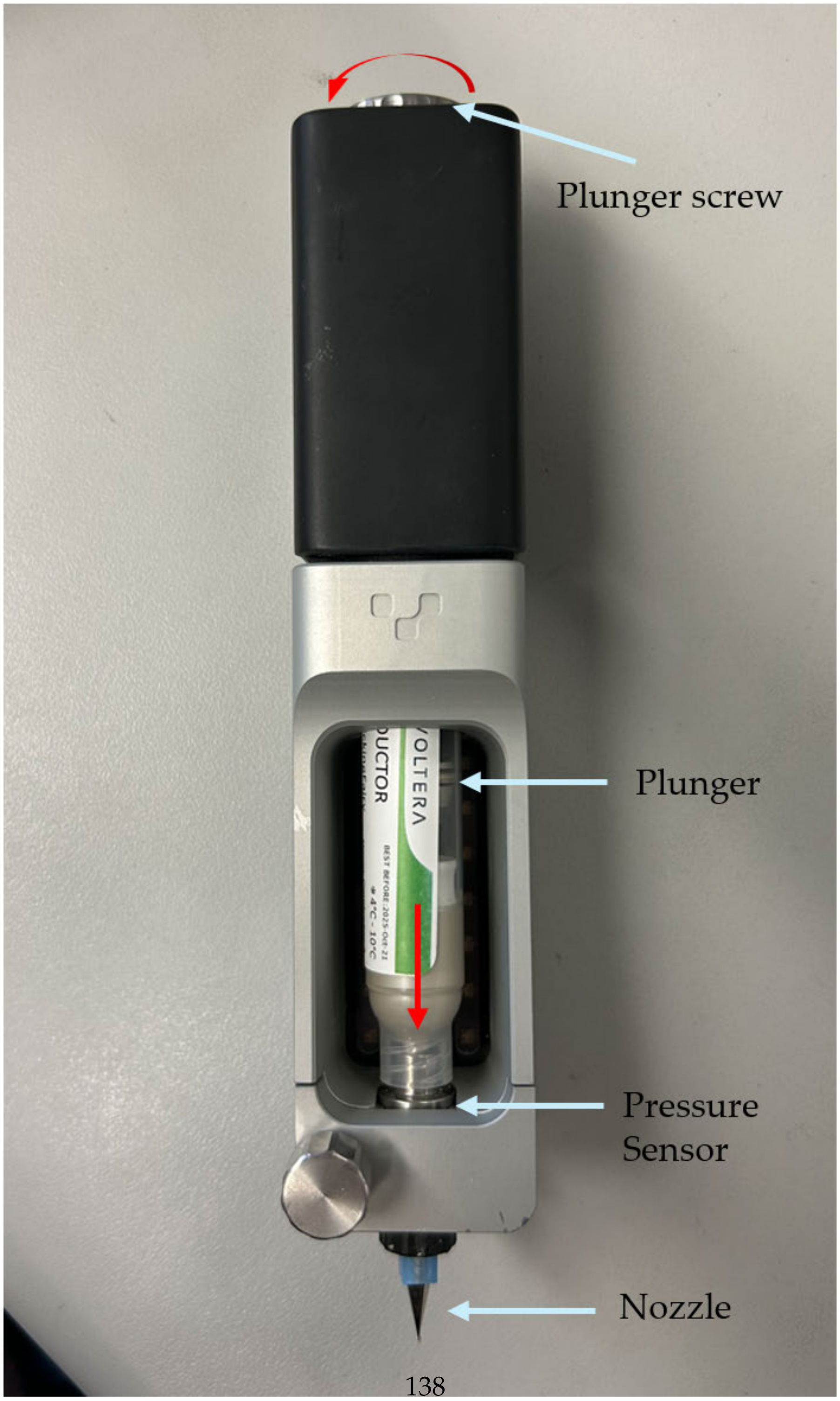

Figure A.7: NOVA dispenser.

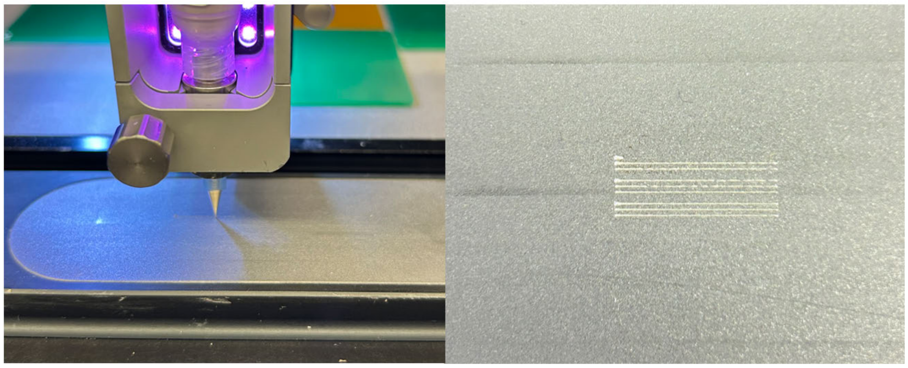

Figure A.8: NOVA dispenser calibration.

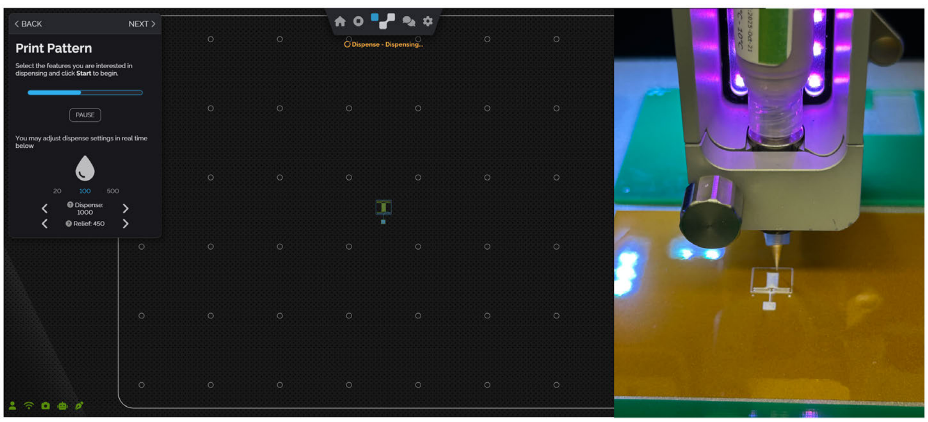

Figure A.9: NOVA dispensing process.

closed geometries, then select *All Geometries*. Lastly, select Cut Path from the top toolbar, set the *Offset Number* to 3, select the geometries you would like to cut, then hit *OK*. Then, export the ANC file (*File » Output NC*). There will then be four prompts: *Are there any percussion holes?* (No), *Are there any trepanned holes?* (No), *Are there any cut paths being used?* (Yes), and *Is there any etching required?* (No). The ANC file containing the G-code will then be generated and saved.

Once the G-code is generated and placed in a .ANC file, Cimita laser software can be

Figure A.10: Oxford Series-A laser micromachining tool.

opened in Engineer mode. The home screen is shown in Fig. A.11. First, select *Home + Enable Axes*, then turn laser on (top right corner). Select *Measure*. After measurement is taken, navigate to LASERPOWER.txt, copy the last line in the file, and paste it in the DiagnosticHistory.ods spreadsheet. This is the sign-in/sign-out routine, and must be done before and after cutting. Once the session has been recorded in this manner, one may click on the X, Y, or Z icons to toggle their respective stepper motors on or off, which allows one to load and unload samples manually on the cutting stage inside the unit. Load the sample

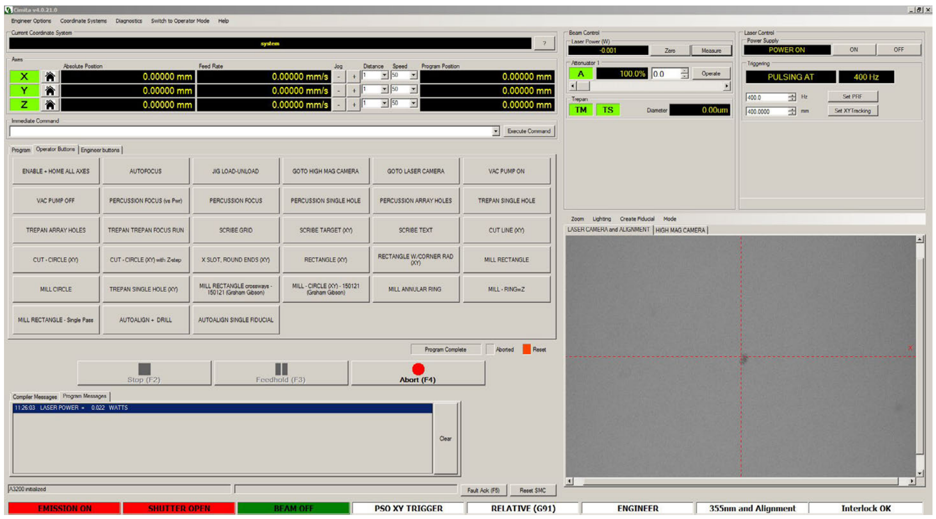

Figure A.11: Oxford Series-A laser micromachining tool.

and secure it, then re-enable all axes.

To focus the camera/laser assembly on the surface to be cut, one may manually lower the z-height using the +/- buttons next to the z-height indicator at the top of the screen, or type *G90 Zx* in the immediate command line to bring the height to 'x' mm. Focus the camera/laser assembly on the cut surface.

Next, line the cross-hairs up with a lower-leftmost fiducial in the design, or the fiducial that was placed at (0,0) in the AlphaCAM file; we will make this reference coordinate point (0,0) for our G-code file. Go to *Coordinate Systems » Edit Jigs » DLJig » Edit*. Enter the current X and Y coordinates under Absolute Position. Enter 0 degrees for rotation. Click *OK*, then go to *Coordinate Systems » Component Coordinates* and select *DLcoords*. The top bar should say *DLcoords on DLJig.X1*, and the Program Position should be at x = 0 and y = 0.

Now, move to and center on the next fiducial to the right. What we are doing here is trying to find the angle of rotation, since we cannot get the object cut perfectly aligned by hand. So, with a calculator in degree mode, find $arctan(y/x)$ with y and x from Program

Position; this is the angle of rotation. Navigate back to *DLJig*, and enter this number for the rotation value. Go to *Coordinate Systems* » *Component Coordinates* and select *DLcoords* again. The system is now aligned with our design.

Next, go to *Program* » *Load*, and load in the .ANC file. Select *Compile*, then *Start*. Select NO for autofocus, confirm focus point, and say yes to already auto-aligned. Now, the next few prompts will ask for cut speed, number of cut passes, and laser power %. For silver ink on PI μm, these values are 0.8 mm/s, 35, and 5%, respectively. For thicker PI than 25 μm, more cut passes will be required.

Once the cutting is complete, unload the sample, close the shutter, perform a measure and record it in the spreadsheet, turn laser off, close all programs, and turn the key to off.

References

[1] McKinsey. (2023) Additive manufacturing: A long-term game changer for manufacturers. https://www.mckinsey.com/capabilities/operations/our-insights/additive-manufacturing-a-long-term-game-changer-for-manufacturers#/. Accessed: 2023-04-19. [Online]. Available: https://www.mckinsey.com/capabilities/operations/our-insights/additive-manufacturing-a-long-term-game-changer-for-manufacturers#/

[2] S. Chandrasekaran, A. Jayakumar, and R. Velu, "A comprehensive review on printed electronics: A technology drift towards a sustainable future," *Nanomaterials*, vol. 12, no. 23, 2022. [Online]. Available: https://www.mdpi.com/2079-4991/12/23/4251

[3] J. Wiklund, A. Karakoç, T. Palko, H. Yiğitler, K. Ruttik, R. Jäntti, and J. Paltakari, "A review on printed electronics: Fabrication methods, inks, substrates, applications and environmental impacts," *Journal of Manufacturing and Materials Processing*, vol. 5, no. 3, 2021. [Online]. Available: https://www.mdpi.com/2504-4494/5/3/89

[4] T. Blachowicz and A. Ehrmann, "3d printed mems technology—recent developments and applications," *Micromachines*, vol. 11, no. 4, 2020. [Online]. Available: https://www.mdpi.com/2072-666X/11/4/434

[5] Voltera Inc. (2024) Voltera v-one tech specs. Accessed: 2024-09-17. [Online]. Available: https://www.voltera.io/tech-specs

[6] J. Sun, R. Sun, P. Jia, M. Ma, and Y. Song, "Fabricating flexible conductive structures by printing techniques and printable conductive materials," *J. Mater. Chem. C*, vol. 10, pp. 9441–9464, 2022. [Online]. Available: http://dx.doi.org/10.1039/D2TC01168A

[7] G.-K. Lau and M. Shrestha, "Ink-jet printing of micro-electro-mechanical systems (mems)," *Micromachines*, vol. 8, no. 6, 2017. [Online]. Available: https://www.mdpi.com/2072-666X/8/6/194

[8] W. Wu, "Introduction to Printed Electronics," in *Printed Electronics Technologies*. The Royal Society of Chemistry, 07 2022. [Online]. Available: https://doi.org/10.1039/9781788019699-00001

[9] Voltera Inc. (2023) What are precision fluid dispensing systems? Accessed: 2024-09-17. [Online]. Available: https://www.voltera.io/blog/precision-fluid-dispensing-systems

[10] D. Godec, J. Gonzalez-Gutierrez, A. Nordin, E. Pei, and J. Ureña, *A Guide to Additive Manufacturing*. Springer, 09 2022.

[11] J. Gonzalez-Gutierrez, S. Cano, S. Schuschnigg, C. Kukla, J. Sapkota, and C. Holzer, "Additive manufacturing of metallic and ceramic components by the material extrusion of highly-filled polymers: A review and future perspectives," *Materials*, vol. 11, no. 5, 2018. [Online]. Available: https://www.mdpi.com/1996-1944/11/5/840

[12] The Index Project. (2024) Voxel8. https://theindexproject.org/award/nominees/1765. Accessed: 2024-09-18.

[13] Nano3DPrint. (2024) A2200 multi-material electronics 3d printer. https://nano3dprint.com/product/a2200/. Accessed: 2024-09-18.

[14] Voltera. (2024) Ultimate guide to choosing materials for a new electronics product. https://www.voltera.io/blog/ultimate-guide-choosing-materials-new-electronics-product. Accessed: 2024-09-18.

[15] J. Zhang, M. Ahmadi, G. Fargas, N. Perinka, J. Reguera, S. Lanceros-Méndez, L. Llanes, and E. Jiménez-Piqué, "Silver nanoparticles for conductive inks: From synthesis and ink formulation to their use in printing technologies," *Metals*, vol. 12, no. 2, 2022. [Online]. Available: https://www.mdpi.com/2075-4701/12/2/234

[16] S. M. F. Cruz, L. A. Rocha, and J. C. Viana, “Printing technologies on flexible substrates for printed electronics,” in *Flexible Electronics*, S. Rackauskas, Ed. Rijeka: IntechOpen, 2018, ch. 3. [Online]. Available: https://doi.org/10.5772/intechopen.76161

[17] Can-Do Tape. (2024) What is surface energy and why is it important in bonding? https://www.can-dotape.com/blog/what-is-surface-energy-and-why-is-it-important-in-bonding/. Accessed: 2024-09-18.

[18] MorePCB. (2024) Pcb substrate materials: Everything you need to know. https://morepcb.com/pcb-substrate/. Accessed: 2024-09-18.

[19] Cadence PCB Solutions. (2020) Fr4 maximum temperature and thermal dissipation. https://resources.pcb.cadence.com/blog/2020-fr4-maximum-temperature-and-thermal-dissipation. Accessed: 2024-09-18.

[20] S. Pagliano, D. E. Marschner, D. Maillard *et al.*, “Micro 3d printing of a functional mems accelerometer,” *Microsystems Nanoengineering*, vol. 8, p. 105, 2022. [Online]. Available: https://doi.org/10.1038/s41378-022-00440-9

[21] S. Sulaiman, N. A. Rashid, A. S. A. Aziz, L. Q. Jun, and S. M. H. S. M. Jaafar, “Inkjet-printed graphene-based flexible humidity sensor for environmental applications,” in *2020 IEEE International Conference on Semiconductor Electronics (ICSE)*, 2020, pp. 148–151.

[22] A. Raj, A. Chandrakar, B. Tyagi *et al.*, “Advancements in material extrusion based three-dimensional printing of sensors: a review,” *International Journal on Interactive Design and Manufacturing (IJIDeM)*, vol. 18, pp. 627–648, 2024. [Online]. Available: https://doi-org.uml.idm.oclc.org/10.1007/s12008-023-01718-6

[23] H. Nassar, M. Ntagios, W. T. Navaraj, and R. Dahiya, “Multi-material 3d printed bendable smart sensing structures,” in *2018 IEEE SENSORS*, 2018, pp. 1–4.

[24] G. Kovacs, *Micromachined Transducers Sourcebook*, ser. McGraw-Hill series in electrical and computer engineering. WCB/McGraw-Hill, 1998. [Online]. Available: https://books.google.ca/books?id=MzNxQgAACAAJ

[25] Voltera, “Conductor 3 - technical data sheet rev 2,” https://files.gitbook.com/v0/b/gitbook-x-prod.appspot.com/o/spaces%2FKMS1I2mCuOJeZyXjzOqV%2Fuploads%2FZsmlQuks1lY6xjpOtU4T%

2FConductor3-Rev2.pdf?alt=media&token=63602eed-1367-46e2-86ea-e591fce45344, 2024, accessed: 2024-09-18.

[26] ——. (2024) Conductor 3 ink cartridge - 2 ml. https://store.voltera.io/products/conductor-3-ink-cartridge-2ml. Accessed: 2024-09-18.

[27] Electro-Wind, "5 mil (.005" thick) general purpose polyimide film hn - 180°c amber 36" wide x 40 ft roll," https://www.electro-wind.com/5-mil-005-thick-general-purpose-polyimide-film-hn-180c-amber-36-wide-x-40-ft-roll, 2024, accessed: 2024-09-18.

[28] Designer Data. (2024) Polyimide - thermoplastic material. https://designerdata.nl/materials/plastics/thermo-plastics/polyimide. Accessed: 2024-09-18.

[29] Voltera. (2024) Voltera nova. https://store.voltera.io/products/voltera-nova. Accessed: 2024-09-18.

[30] Y. El-Hajj, M. Ghalamboran, and G. Grau, "Inkjet and extrusion printed silver biomedical tattoo electrodes," in *2022 IEEE International Conference on Flexible and Printable Sensors and Systems (FLEPS)*, 2022, pp. 1–4.

[31] M. K. Idris, J. Qiu, G. W. Melenka, and G. Grau, "Printing electronics directly onto carbon fiber composites: unmanned aerial vehicle (uav) wings with integrated heater for de-icing," *Engineering Research Express*, vol. 2, no. 2, p. 025022, may 2020. [Online]. Available: https://dx.doi.org/10.1088/2631-8695/ab8e24

[32] P. Escobedo, M. Fernández-Ramos, N. López-Ruiz *et al.*, "Smart facemask for wireless co2 monitoring," *Nature Communications*, vol. 13, p. 72, 2022. [Online]. Available: https://doi.org/10.1038/s41467-021-27733-3

[33] D. Lagace and C. Shafai, "A stretchable extrusion printed piezoresistive strain sensor for respiration monitoring," in *2024 IEEE Canadian Conference on Electrical and Computer Engineering (CCECE)*, 2024, pp. 117–118.

[34] C. Inc. (2024) Comsol multiphysics® software. https://www.comsol.com/comsol-multiphysics. Accessed: September 19, 2024.

[35] W. Hortschitz, A. Kainz, R. Beigelbeck, G. Schmid, and F. Keplinger, "Review on sensors for electric fields near power transmission systems," *Measurement Science and Technology*, vol. 35, no. 5, p. 052001, feb 2024. [Online]. Available: https://dx.doi.org/10.1088/1361-6501/ad243a

[36] Hydro-Québec, "Exposure to electric and magnetic fields," 2024, accessed: 2024-11-28. [Online]. Available: https://www.hydroquebec.com/fields/exposure/

[37] Z. Agorastou, T. Noulis, and S. Siskos, "Analog sensor interface for field mill sensors in atmospheric applications," *Sensors*, vol. 22, no. 21, 2022. [Online]. Available: https://www.mdpi.com/1424-8220/22/21/8405

[38] M. G. Bateman, M. F. Stewart, S. J. Podgorny, H. J. Christian, D. M. Mach, R. J. Blakeslee, J. C. Bailey, and D. Daskar, "A low-noise, microprocessor-controlled, internally digitizing rotating-vane electric field mill for airborne platforms," *Journal of Atmospheric and Oceanic Technology*, vol. 24, no. 7, pp. 1245 – 1255, 2007. [Online]. Available: https://journals.ametsoc.org/view/journals/atot/24/7/jtech2039_1.xml

[39] B. Bahreyni, G. Wijeweera, C. Shafai, and A. Rajapakse, "Design and testing of a field-chopping electric field sensor using thermal actuators with mechanically amplified response," in *TRANSDUCERS 2007 - 2007 International Solid-State Sensors, Actuators and Microsystems Conference*, 2007, pp. 1397–1400.

[40] T. Chen and C. Shafai, "A flexible printed circuit board based microelectromechanical field mill with a vertical movement shutter driven by an electrostatic actuator," *Sensors*, vol. 24, no. 2, 2024. [Online]. Available: https://www.mdpi.com/1424-8220/24/2/439

[41] S. Liyanage, C. Shafai, T. Chen, and A. Rajapakse, "Torsional moving electric field sensor with modulated sensitivity and without reference ground," *Proceedings*, vol. 1, no. 4, 2017. [Online]. Available: https://www.mdpi.com/2504-3900/1/4/350

[42] T. Chen, "Mem electric field sensor using force deflection with capacitance interrogation," in *2013 IEEE Power Energy Society General Meeting*, 2013, pp. 1–4.

[43] F. Systems, "Quick guide to mems devices," 2024, accessed: 2024-11-28. [Online]. Available: https://www.falco-systems.com/quick_MEMS.pdf

[44] D.-K. Electronics, “Ppf series datasheet,” 2024, accessed: 2024-11-28. [Online]. Available: https://mm.digikey.com/Volume0/opasdata/d220001/medias/docus/5342/PPF_Series.pdf

[45] KiCad, “Kicad eda - open source pcb design software,” 2024, accessed: 2024-11-28. [Online]. Available: https://www.kicad.org/

[46] K. Corporation. (2024) P-7 stylus profiler. https://www.kla.com/products/instruments/stylus-profilers/p-7. Accessed: September 19, 2024.

[47] S. R. Systems. (2024) Ps300 series high voltage power supplies. https://www.thinksrs.com/products/ps300.html. Accessed: September 19, 2024.

[48] L. Microsystems. (2024) Leica DM6 M microscope. https://www.leica-microsystems.com/products/light-microscopes/p/leica-dm6-m/. Accessed: September 19, 2024.

[49] P. C.-P. Chao, C.-W. Chiu, and C.-Y. Tsai, “A novel method to predict the pull-in voltage in a closed form for micro-plates actuated by a distributed electrostatic force,” *Journal of Micromechanics and Microengineering*, vol. 16, no. 5, p. 986, apr 2006. [Online]. Available: https://dx.doi.org/10.1088/0960-1317/16/5/016

[50] E. ToolBox. (2024) Cantilever beams. https://www.engineeringtoolbox.com/cantilever-beams-d_1848.html. Accessed: 2024-09-19.

[51] ——, “Metals - poisson’s ratio,” https://www.engineeringtoolbox.com/metals-poissons-ratio-d_1268.html, 2024, accessed: 2024-09-19.

[52] D. Surf, “Software solutions for profilometry,” 2024, accessed: 2024-11-28. [Online]. Available: https://www.digitalsurf.com/software-solutions/profilometry/

[53] Hexagon, “Alphacam - cad/cam software,” 2024, accessed: 2024-11-28. [Online]. Available: https://hexagon.com/products/product-groups/computer-aided-manufacturing-cad-cam-software/alphacam

[54] A. Devices, “Ad7747: 24-bit capacitance-to-digital converter,” 2024, accessed: 2024-11-28. [Online]. Available: https://www.analog.com/en/products/ad7747.html

[55] D.-K. Electronics, “Stmicroelectronics nucleo-f401re development board,” 2024, accessed: 2024-11-28. [Online]. Available: https://www.digikey.ca/en/products/detail/stmicroelectronics/NUCLEO-F401RE/4695525

[56] D. Lagace, "Stm32-ad7747 library and example code," 2024, accessed: 2024-11-28. [Online]. Available: https://github.com/desmond-lagace/STM32-AD7747

[57] D. Lagace, T. Chen, and C. Shafai, "An extrusion printed capacitively interrogated dc electric field sensor," in *2024 IEEE International Conference on Flexible and Printable Sensors and Systems (FLEPS)*, 2024, pp. 1–4.

[58] T. Chen, B. Hill, S. Isik, C. Shafai, and L. Shafai, "Dc electric field sensor based on polyimide substrate," in *2021 IEEE Sensors*, 2021, pp. 1–4.

[59] G. Wijeweera, B. Bahreyni, C. Shafai, A. Rajapakse, and D. R. Swatek, "Micromachined electric-field sensor to measure ac and dc fields in power systems," *IEEE Transactions on Power Delivery*, vol. 24, no. 3, pp. 988–995, 2009.

[60] J. Yang and J. Zhang, *MEMS Actuators Driven by Lorentz Force*. Singapore: Springer Singapore, 2018, pp. 929–944. [Online]. Available: https://doi.org/10.1007/978-981-10-5945-2_28

[61] J. S. Ko, M. L. Lee, D.-S. Lee, C. A. Choi, and Y. Tae Kim, "Development and application of a laterally driven electromagnetic microactuator," *Applied Physics Letters*, vol. 81, no. 3, pp. 547–549, 07 2002. [Online]. Available: https://doi.org/10.1063/1.1494462

[62] F.-Y. Lee, T.-L. Tang, and W. Fang, "Development of a novel dual-axis large-displacement microstage using lorentz force actuators and curved-beam springs," *Procedia Engineering*, vol. 25, pp. 689–692, 2011, eurosensorsXXV. [Online]. Available: https://www.sciencedirect.com/science/article/pii/S1877705811058395

[63] S.-J. Lin, C.-C. Lee, W.-L. Sung, F.-Y. Lee, and W. Fang, "Displacement enhancement of 1-axis lorentz force actuator," in *2013 Transducers Eurosensors XXVII: The 17th International Conference on Solid-State Sensors, Actuators and Microsystems (TRANSDUCERS EUROSENSORS XXVII)*, 2013, pp. 1591–1594.

[64] B. Park, E. Afsharipour, D. Chrusch, C. Shafai, D. Andersen, and G. Burley, "A low voltage and large stroke lorentz force continuous deformable polymer mirror for wavefront control," *Sensors and Actuators A: Physical*, vol. 280, pp. 197–204, 2018. [Online]. Available: https://www.sciencedirect.com/science/article/pii/S0924424718300189

[65] X. Lv, W. Wei, X. Mao, J. Yang, and F. Yang, "A novel mems actuator with large lateral stroke driven by lorentz force," *Journal of Micromechanics and Microengineering*, vol. 25, no. 2, p. 025009, 2015. [Online]. Available: https://iopscience.iop.org/article/10.1088/0960-1317/25/2/025009

[66] B. Park, E. Afsharipour, D. Chrusch, C. Shafai, D. Andersen, and G. Burley, "Large displacement bi-directional out-of-plane lorentz actuator array for surface manipulation," *Journal of Micromechanics and Microengineering*, vol. 27, no. 8, p. 085005, jul 2017. [Online]. Available: https://dx.doi.org/10.1088/1361-6439/aa7970

[67] F. P. F. P. Beer, E. R. E. R. Johnston, J. T. DeWolf, and D. F. D. F. Mazurek, *Mechanics of materials*, seventh edition. ed. New York, NY: McGraw-Hill Education, 2015.

[68] "Veeco fpp 5000 four-point probe station," https://www.jmind.com/equipment/veeco-fpp-5000/, 2025, accessed: 2025-03-19.

[69] Y.-I. Lee, Y.-S. Goo, K.-J. Lee, Y.-G. Hwang, Y. Byun, H. J. Park, D.-Y. Park, N. V. Myung, and Y.-H. Choa, "Effect of uv/ozone treatment on interactions between ink-jet printed cu patterns and polyimide substrates," *Thin Solid Films*, vol. 519, no. 20, pp. 6853–6857, 2011, 10th Asia-Pacific Conference on Plasma Science and Technology. [Online]. Available: https://www.sciencedirect.com/science/article/pii/S0040609011008662

[70] C. J. Wohl, M. A. Belcher, S. Ghose, and J. W. Connell, "Modification of the surface properties of polyimide films using polyhedral oligomeric silsesquioxane deposition and oxygen plasma exposure," *Applied Surface Science*, vol. 255, no. 18, pp. 8135–8144, 2009. [Online]. Available: https://www.sciencedirect.com/science/article/pii/S0169433209006345

[71] I. Kim, H. Roh, W. Choi, and D. Kim, "Air-gap embedded triboelectric nanogenerator via surface modification of non-contact layer using sandpapers," *Nanoscale*, vol. 13, pp. 8837–8847, 2021. [Online]. Available: http://dx.doi.org/10.1039/D1NR01517F

[72] P. Morais, A. Akhavan-Safar, R. J. C. Carbas, E. A. S. Marques, B. Karunamurthy, and L. F. M. da Silva, "Mode i fatigue and fracture assessment of polyimide–epoxy and silicon–epoxy interfaces in chip-package components," *Polymers*, vol. 16, no. 4, 2024. [Online]. Available: https://www.mdpi.com/2073-4360/16/4/463

[73] ASTM International, "Standard test methods for rating adhesion by tape test," ASTM D3359-23, 2023, available online: https://cdn.standards.iteh.ai/samples/114668/46ea6693ae224de6bb02376bb9f45b49/ASTM-D3359-23.pdf.

[74] T. Chen and C. Shafai, "A flexible pcb based out of plane bimorph mems thermal actuator," in *2023 IEEE International Conference on Flexible and Printable Sensors and Systems (FLEPS)*, 2023, pp. 1–4.

[75] Keysight Technologies, "Keysight 34401a digital multimeter, 6-digit," https://www.keysight.com/ca/en/product/34401A/digital-multimeter-6-digit.html, 2023, accessed: 2024-12-10.

[76] Engineering Toolbox. (2003) Linear expansion coefficients. https://www.engineeringtoolbox.com/linear-expansion-coefficients-d_95.html. Accessed: 2024-09-19.

[77] Keysight E3640A 30W Power Supply, 8V, 3A or 20V, 1.5A. https://www.keysight.com/ca/en/product/E3640A/30w-power-supply-8v-3a-20v-1-5a.html. Accessed: 2025-01-01.

[78] OMRON Electronic Components - Americas, "What is an electrical relay? | omron electronic components - americas," https://components.omron.com/us-en/products/basic-knowledge/relays/basics, accessed: March 13, 2025.

[79] "Crydom solid state relays vs. electromechanical relays," https://www.arrow.com/en/research-and-events/articles/crydom-solid-state-relays-vs-electromechanical-relays#:~:text=An%20electromechanical%20relay%20uses%20a,contains%20the%20high%2Dpower%20signal, accessed: March 13, 2025.

[80] T. Cao, T. Hu, and Y. Zhao, "Research status and development trend of mems switches: A review," *Micromachines*, vol. 11, no. 7, 2020. [Online]. Available: https://www.mdpi.com/2072-666X/11/7/694

[81] C. Goldsmith, J. Ehmke, A. Malczewski, B. Pillans, S. Eshelman, Z. Yao, J. Brank, and M. Eberly, "Lifetime characterization of capacitive rf mems switches," in *2001 IEEE MTT-S International Microwave Sympsoium Digest (Cat. No.01CH37157)*, vol. 1, 2001, pp. 227–230 vol.1.

[82] D. Dellaert and J. Doutreloigne, "Compact thermally actuated latching mems switch with large contact force," *Electronics Letters*, vol. 51, pp. 80–81, 2015.

[83] R. M. Proie, T. Ivanov, J. S. Pulskamp, and R. G. Polcawich, "A compact, low loss piezoelectric rf mems relay with sub 100-ns switching times," in *2012 IEEE/MTT-S International Microwave Symposium Digest*, 2012, pp. 1–3.

[84] J. Qiu, J. Lang, A. Slocum, and A. Weber, "A bulk-micromachined bistable relay with u-shaped thermal actuators," *Journal of Microelectromechanical Systems*, vol. 14, no. 5, pp. 1099–1109, 2005.

[85] G. Schiavone, M. P. Y. Desmulliez, and A. J. Walton, "Integrated magnetic mems relays: Status of the technology," *Micromachines*, vol. 5, no. 3, pp. 622–653, 2014. [Online]. Available: https://www.mdpi.com/2072-666X/5/3/622

[86] "Chapter 10 - mems microrelay," in *Space Microsystems and Micro/nano Satellites*, ser. Micro and Nano Technologies, Z. You, Ed. Butterworth-Heinemann, 2018, pp. 361–417. [Online]. Available: https://www.sciencedirect.com/science/article/pii/B9780128126721000102

[87] "Mems solid state relays," Red Rock, White Paper, 2013, accessed: March 13, 2025. [Online]. Available: https://www.mouser.com/pdfdocs/RedRock-White-Paper-130417.pdf

[88] I. V. Uvarov and I. A. Belozerov, "Design guideline for a cantilever-type mems switch with high contact force," *Micro*, vol. 4, no. 1, pp. 1–13, 2024. [Online]. Available: https://www.mdpi.com/2673-8023/4/1/1

[89] N. S. Nise, *Control Systems Engineering*, 7th ed. Hoboken, NJ: Wiley, 2015.

[90] Circuit Basics, "Srd-05vdc-sl-c datasheet," https://www.circuitbasics.com/wp-content/uploads/2015/11/SRD-05VDC-SL-C-Datasheet.pdf, 2015, accessed: March 13, 2025.

[91] Littelfuse, "Littelfuse integrated circuits cpc1017n datasheet," https://www.littelfuse.com/assetdocs/littelfuse-integrated-circuits-cpc1017n-datasheet?assetguid=b4f177f1-629f-4104-97a5-8b8d709e83de, accessed: March 13, 2025.